INFORMATION TO USERS

This manuscript has been reproduced from the microfilm master. UMI films the text directly from the original or copy submitted. Thus, some thesis and dissertation copies are in typewriter face, while others may be from any type of computer printer.

The quality of this reproduction is dependent upon the quality of the copy submitted. Broken or indistinct print, colored or poor quality illustrations and photographs, print bleedthrough, substandard margins, and improper alignment can adversely affect reproduction.

In the unlikely event that the author did not send UMI a complete manuscript and there are missing pages, these will be noted. Also, if unauthorized copyright material had to be removed, a note will indicate the deletion.

Oversize materials (e.g., maps, drawings, charts) are reproduced by sectioning the original, beginning at the upper left-hand corner and continuing from left to right in equal sections with small overlaps.

Photographs included in the original manuscript have been reproduced xerographically in this copy. Higher quality 6" x 9" black and white photographic prints are available for any photographs or illustrations appearing in this copy for an additional charge. Contact UMI directly to order.

ProQuest Information and Learning
300 North Zeeb Road, Ann Arbor, MI 48106-1346 USA
800-521-0600

UMI®

Reproduced with permission of the copyright owner. Further reproduction prohibited without permission.

Reproduced with permission of the copyright owner. Further reproduction prohibited without permission.

Optimal Trajectory Control of Series Resonant Converter

SHENGLI FENG ©

A THESIS SUBMITTED IN PARTIAL FULFILMENT OF THE
REQUIREMENTS OF THE MScEng DEGREE
IN
CONTROL ENGINEERING
LAKEHEAD UNIVERSITY, THUNDER BAY
ONTARIO, CANADA

October 12, 2001

Reproduced with permission of the copyright owner. Further reproduction prohibited without permission.

National Library of Canada
Bibliothèque nationale du Canada

Acquisitions and Bibliographic Services
Acquisitions et services bibliographiques

395 Wellington Street
Ottawa ON K1A 0N4
Canada

395, rue Wellington
Ottawa ON K1A 0N4
Canada

Your file Votre référence

Our file Notre référence

The author has granted a non-exclusive licence allowing the National Library of Canada to reproduce, loan, distribute or sell copies of this thesis in microform, paper or electronic formats.

L'auteur a accordé une licence non exclusive permettant à la Bibliothèque nationale du Canada de reproduire, prêter, distribuer ou vendre des copies de cette thèse sous la forme de microfiche/film, de reproduction sur papier ou sur format électronique.

The author retains ownership of the copyright in this thesis. Neither the thesis nor substantial extracts from it may be printed or otherwise reproduced without the author's permission.

L'auteur conserve la propriété du droit d'auteur qui protège cette thèse. Ni la thèse ni des extraits substantiels de celle-ci ne doivent être imprimés ou autrement reproduits sans son autorisation.

0-612-64718-8

Canada

Reproduced with permission of the copyright owner. Further reproduction prohibited without permission.

Abstract

Resonant power converters have gained increased attention in industry due to various advantages over conventional pulse width modulation (PWM) converters. Resonant converters have improved transient response, reduced switching losses and stresses, reduced equipment size and weight and reduced electromagnetic interference (EMI). In this thesis, series resonant converters (SRC) in variable and constant frequency topologies are analyzed using state-space approach for effective control. The design and implementation of a practical optimal trajectory control (OTC) scheme is shown. Experimental results are presented to demonstrate the performance of the proposed control scheme.

Reproduced with permission of the copyright owner. Further reproduction prohibited without permission.

Acknowledgements

I would like to acknowledge my supervisor, Dr. K. Natarajan, for his great help and support. During the whole work, he supervised me on experiments and theory patiently. His erudite knowledge makes this thesis possible. I also would like to thank Dr. S. Y. Mansour as my co-supervisor.

Reproduced with permission of the copyright owner. Further reproduction prohibited without permission.

Contents

1 Introduction **1**
- 1.1 Power Electronics . . . 1
- 1.2 DC-DC Conversion . . . 2
- 1.3 Resonant Converters . . . 2
  - 1.3.1 Advantages of Resonant Converters . . . 2
  - 1.3.2 Resonant Converter Control Scheme . . . 4
- 1.4 Optimal Trajectory Control . . . 4
- 1.5 Power Semiconductor Switches . . . 5
- 1.6 Thesis Outline . . . 6

2 Optimal Trajectory Control of VF-SRC **7**
- 2.1 Introduction . . . 7
- 2.2 State Plane Analysis of Series Resonant Converters . . . 8
  - 2.2.1 State Plane Analysis . . . 8
- 2.3 Optimal Trajectory Control of VF-SRC . . . 10
  - 2.3.1 Control Laws . . . 10
  - 2.3.2 Design Considerations . . . 14
  - 2.3.3 Implementation Issues . . . 16
- 2.4 Modified Capacitor Voltage Technique . . . 17
  - 2.4.1 Robust Optimal Trajectory Control . . . 17
  - 2.4.2 Multirate Modified Capacitor Voltage Control Strategy . . . 19
  - 2.4.3 Outermost Loop Controller . . . 21
- 2.5 Results . . . 21
  - 2.5.1 Simulation Results . . . 22
  - 2.5.2 Implementation . . . 30
  - 2.5.3 Experimental Results . . . 31
- 2.6 Conclusion . . . 41

3 Optimal Trajectory Control of CF-SRC **42**
- 3.1 Introduction . . . 42
- 3.2 State-Plane Analysis of CF-SRC . . . 43
  - 3.2.1 Circuit Topological Modes . . . 44
  - 3.2.2 Control Parameterization of the CF-SRC . . . 45

Reproduced with permission of the copyright owner. Further reproduction prohibited without permission.

3.2.3 Steady state Characteristics 49
3.3 Optimal Trajectory Control of CF-SRC 50
3.3.1 Implementation Aspects 51
3.3.2 Multirate Control Strategy 53
3.4 Results 54
3.4.1 Simulation Results 54
3.4.2 Experimental Results 60
3.5 Conclusion 66

4 Conclusion and Future Work **68**

A **69**
A.1 Gate Drive Circuit 69
A.2 Snubber Circuit 70
A.3 Control Logic 71
A.3.1 Below Frequency Operation for VF-SRC 71
A.3.2 Above Frequency Operation for VF-SRC 71
A.3.3 Nonlinear Operation for CF-SRC 72
A.4 Maple Code 72

Reproduced with permission of the copyright owner. Further reproduction prohibited without permission.

List of Figures

2.1 Variable Frequency SRC circuit 7
2.2 Topological Modes of Variable Frequency SRC 9
2.3 Waveforms of i_L and v_C in Below Resonant Frequency Operation 11
2.4 Waveforms of i_L and v_C in Above Resonant Frequency Operation 12
2.5 Steady State Trajectory of Below Resonant Frequency Operation 12
2.6 Steady State Trajectory of Above Resonant Frequency Operation 13
2.7 Multirate Control Strategy 20
2.8 PI controller of outermost loop 21
2.9 Simplified Control Law (Below-Simulation) 23
2.10 Transient of i_{LN} and v_{CN} (Below-Simulation-Increasing load) 23
2.11 Transient of R (Below-Simulation-Increasing load) 24
2.12 Transient of i_{LN} and v_{CN} (Below-Simulation-Decreasing load) 24
2.13 Transient of R (Below-Simulation-Decreasing load) 25
2.14 Transient of Output Voltage (Below-Simulation) 26
2.15 Simplified Control Law (Above-Simulation) 26
2.16 Transient of i_{LN} and v_{CN}(Above-Simulation-Increasing load) 27
2.17 Transient of R(Above-Simulation-Increasing load) 27
2.18 Transient of i_{LN} and v_{CN}(Above-Simulation-Decreasing load) 28
2.19 Transient of R(Above-Simulation-Decreasing Load) 29
2.20 Transient of Output Voltage (Above-Simulation) 29
2.21 Waveforms of simplified control law(Below-Lab) 30
2.22 Switching Signals (Below-Lab) 31
2.23 Waveforms of simplified control law(Above-Lab) 32
2.24 Switching Signals (Above-Lab) 32
2.25 Steady State of i_{LN} and v_{CN} (Below-Lab) 33
2.26 Transient of i_{LN} and v_{CN} (Below-Lab-Increasing Load) 34
2.27 Transient of R(Below-Lab-Increasing Load) 34
2.28 Transient of Output Voltage and Error (Below-Lab-Increasing Load) 35
2.29 Transient of i_{LN} and v_{CN} (Below-Lab-Decreasing Load) 35
2.30 Transient of R(Below-Lab-Decreasing Load) 36
2.31 Transient of Output Voltage and Error (Below-Lab-Decreasing Load) . . . 36
2.32 Steady State of i_{LN} and v_{CN} (Above-Lab) 37
2.33 Transient of i_{LN} and v_{CN} (Above-Lab-Increasing Load) 38
2.34 Transient of R (Above-Lab-Increasing Load) 38

Reproduced with permission of the copyright owner. Further reproduction prohibited without permission.

2.35 Transient of Output Voltage and Error (Above-Lab-Increasing Load) . . . 39
2.36 Transient of i_{LN} and v_{CN} (Above-Lab-Decreasing Load) 39
2.37 Transient of R (Above-Lab-Decreasing Load) 40
2.38 Transient of Output Voltage and Error (Above-Lab-Decresing Load) 40

3.1 Constant Frequency SRC Circuit 43
3.2 Topological Modes of Constant Frequency SRC 44
3.3 State Plane Trajectory in Nonlinear Operation 46
3.4 State Plane Trajectory in Linear Operation 46
3.5 R variation with Load Current for $V_0/V_S = 0.25$ 49
3.6 Maximum I_0 Variation with V_0 In Nonlinear and Linear Operation 50
3.7 Control Law Simplification for Nonlinear Mode 52
3.8 Control Law Simplification for Linear Mode 53
3.9 Multirate Control Scheme of CF-SRC 55
3.10 Simplified Control Law (Nonlinear-Simulation) 56
3.11 Transient of i_{LN} and v_{CN} (Nonlinear-Simulation-Increasing Load) 56
3.12 Transient of R (Nonlinear-Simulation-Increasing Load) 57
3.13 Transient of i_{LN} and v_{CN} (Nonlinear-Simulation-Decreasing Load) 58
3.14 Transient of R (Nonlinear-Simulation-Decreasing Load) 58
3.15 Transient of Output Voltage V_{0N} (Simulation) 59
3.16 Steady State of i_{LN} and v_{CN} (Linear-Simulation) 59
3.17 Simplified Control Law (Nonlinear-Lab) 61
3.18 Steady State of i_{LN} and v_{CN} (Lab) 62
3.19 Transient of i_{LN} and v_{CN} (Lab-Increasing Load) 62
3.20 Transient of R (Lab-Increasing Load) 63
3.21 Transient of Output Voltage and Error (Lab-Increasing Load) 63
3.22 Transient of i_{LN} and v_{CN} (Lab-Decreasing Load) 64
3.23 Transient of R (Lab-Decreasing Load) 64
3.24 Transient of Output Voltage and Error (Lab-Decreasing Load) 65
3.25 Steady State of i_{LN} and v_{CN} in Linear Mode (Lab) 65
3.26 Performance of Controller with i_{LN} in Saturation (Increasing Load) 66
3.27 Performance of Controller with i_{LN} in Saturation (Decreasing Load) 67

A.1 Lockout Circuit for Variable Frequency SRC 74
A.2 Lockout Circuit for Constant Frequency SRC 75
A.3 Block Diagram of VF-SRC Operation Implementation (Below) 76
A.4 Block Diagram of VF-SRC Operation Implementation (Above) 77
A.5 Block Diagram of CF-SRC Implementation 78

Reproduced with permission of the copyright owner. Further reproduction prohibited without permission.

List of Tables

2.1 Equivalent Circuit DC Voltage 9
2.2 Simulation Parameters for VF-SRC 22
2.3 Implementation Circuit Parameters for VF-SRC 31

3.1 Equivalent Circuit DC Voltage of CF-SRC 44
3.2 Parameters in Simulations for CF-SRC 55
3.3 Parameters in Experiments for CF-SRC 60

Reproduced with permission of the copyright owner. Further reproduction prohibited without permission.

Chapter 1

Introduction

1.1 Power Electronics

Power Electronics is a branch of electrical and electronic engineering concerned with the analysis, design, manufacture and application of power converters. It covers a wide range of electronic circuits in which the objective is to control the transfer of electrical power from a source to a load.

Power electronics has various applications in industries, such as aerospace, telecommunications, etc [1, 2]. The power conversion in different applications can vary from a few watts to a few megawatts. The major source of inefficiency in power conversion is energy loss in the form of heat and the consequent requirement of large heat sinks and good ventilation facilities. Because energy usage and loss represent a contribution to the cost of all products and services, power converters must be made as efficient as possible to satisfy the total application requirements. Efficiency has always been a cardinal consideration in the design and application of power conversion schemes, especially for high power conversion.

In energy conversion, linear active electronic devices and regulators are notoriously inefficient. Therefore, recent research in power conversions is concentrated on switched mode power (SMP) conversion [3, 4]. In switched mode power supplies (SMPS), switches are used. These switches ideally carry current at zero voltage while closed and withstand voltage at zero current while open. Practical switches do not approach the ideal, but are close to the ideal approximation of no losses compared with linear devices. Thus, most practical power converters use switches as the active devices to make power conversion efficient. Therefore, compared to linear mode power supplies, SMPS have a higher efficiency. Moreover, SMPS also have a higher power density due to their high frequency of operation and consequent reduction in size of components. In this thesis, two DC-DC SMPS converters are studied from the point of view of their control to regulate output voltage.

Reproduced with permission of the copyright owner. Further reproduction prohibited without permission.

1.2 DC-DC Conversion

Power conversion requires changing the nature of electrical power delivered to a load as compared to that obtained from the source. In DC-DC conversion, an unregulated DC voltage is converted to a controlled DC voltage level. There are a variety of circuit designs and implementations for DC-DC SMPS. But there are only two basic converter topologies: step-down converter and step-up converter. Other topologies are combinations of the two basic topologies [1, 2, 3, 4].

As the name implies, a step-down converter produces a lower average output voltage than the input voltage level. The output voltage can be controlled by changing switch on-time using a pulse width modulation (PWM) circuit.

Unlike step-down converters, a step-up converter topology is capable of providing an output voltage that is greater than the input voltage. The operating scheme of step-up converters is the same as step-down converters, that is, the output voltage is controlled by varying the duty cycle of a switch using PWM.

Step-down and step-up converters are two basic topologies of DC-DC switching mode converters. Based on these two topologies, a number of topologies can be constructed. For example, buck-boost converter is a cascade combination of buck and boost converters [1, 2, 3, 4]. Fly-back and Cúk converters are derived from the buck-boost converter[1, 2, 3, 4].

It is necessary to mention that both of the basic topologies can only transfer energy in one direction. If bidirectional transfers of voltage and current are needed, a full bridge converter can be used, where both voltage and current can be reversed [2, 3]. If both higher and lower output voltage compared to the input are necessary, or negative polarity output compared to the input is desired, then the buck-boost or Cúk converters should be used.

1.3 Resonant Converters

Conventional DC-DC conversion as considered in the previous section has some drawbacks, such as high switch losses and stresses, high EMI, low efficiency, etc. By using L-C resonant circuits in the main converter circuit and appropriate zero-current-switching and/or zero-voltage-switching strategies as discussed in Section 1.3.1, these drawbacks can be overcome. Because LC resonance is always required, these kind of converters are broadly classified as resonant converters [1].

1.3.1 Advantages of Resonant Converters

The objectives of switch mode converter design are to obtain high efficiency and high power density. To increase power density, the switching frequency must be increased. The benefits of operating with a higher switching frequency include[1, 3, 4]: high power density and efficiency, reduced equipment size, reduced EMI and improved transient response, etc.

However, these benefits have to be traded off against some drawbacks[1, 3, 4]. In the conventional converters, the switches are operated and required to turn on and turn off

Reproduced with permission of the copyright owner. Further reproduction prohibited without permission.

the entire inductor or load current during each switching. This is termed hard-switching. Due to the large di/dt, dv/dt and finite turn on and off time of the switches, this results in increased switching losses, increased electromagnetic interference (EMI) and high stresses on switches. The drawbacks worsen as the switching frequency is increased to reduce converter size, weight and increase power density, consequently reducing its efficiency. To get the benefits of high operating frequency, these drawbacks associated with conventional switch mode converters must be overcome.

The use of resonant converters minimize the effects of these shortcomings. Generally resonant converters use some forms of LC resonant circuits to produce oscillating load current and voltage, thus provide the opportunity to change switch states at zero current through switches and/or zero voltage across them. This strategy is called zero-current-switching (ZCS) or zero-voltage-switching (ZVS) respectively [1]. In contrast to hard-switching, this is termed soft-switching.

In ZCS switching mode, LC tank circuit is used to produce oscillating current. By designing an appropriate logic circuit, a series of switching signals are produced to turn on/off switches at zero current. Such a converter has minimal switch losses, stresses and EMI. ZCS switching mode will be used in the two resonant converters of this thesis. In both resonant converters of this thesis the resonant tank circuit uses a series connection of an inductor and a capacitor. One converter is operated as a variable frequency series resonant converter while the other is a fixed frequency series resonant converter.

In ZVS switching mode, LC tank circuit is also used to produce oscillating voltage. A logic circuit can be designed to produce switching signals to turn on/off switches at zero voltage. This converter can also minimize switch losses, stresses and EMI as well.

Based on ZCS and ZVS switching strategies, resonant converters realize the advantages [1, 9, 10, 16]sought after for switched mode supplies. For example:

1). Increased power density and reduced equipment size and weight
2). High efficiency and fast transient response
3). Reduced EMI
4). Reduced switching losses and stresses than conventional switched mode converters with hard switching

Since switches change their states when the voltage across them or current through them is zero, resonant converters overcome the drawbacks of conventional DC-DC conversion. Because of this significant characteristic, resonant converters are widely studied and applied for high power and high frequency operating in industry [10].

Conventional Pulse-Width-Modulation (PWM) converters are also broadly employed in industry. However, as mentioned earlier, one of the major shortcomings is that the switching losses associated with the turn-on and turn-off of switches increase with switching frequency. Another major drawback of such converters is that high frequency harmonics due to the quasi-square switching current and/or voltage waveforms produce high level of electromagnetic interference (EMI). Therefore, conventional PWM converters are used in low and medium power conversion applications [13].

Reproduced with permission of the copyright owner. Further reproduction prohibited without permission.

1.3.2 Resonant Converter Control Scheme

In PWM converters, the output voltage is regulated by directly controlling the energy input to the slowly responding output filter by modulating the duty cycle of switches. Therefore, the PWM scheme is simple, straight forward and easy to implement in a feedback configuration. The dynamic properties of the converter are easily predictable and dependent upon the filter characteristics and duty cycle control law [8].

In resonant converters, on the other hand, two sets of energy storage elements are present: resonant tank circuit and output filter. The output voltage is controlled indirectly through the control of resonant tank energy. Due to the presence of resonant tank and its fast transient response, the control of resonant converters is considerably more complex than that of PWM converters [8].

Methods of resonant converter control are surveyed and analyzed in [8] in which different control methods are identified and their relative performance evaluated. Notably optimal trajectory control is used in [9]. state-space trajectory control is used in [12], and phase control is used in [15]. In these references, simplified solutions were presented in order to reduce the control complexity. In this thesis, the optimal trajectory control method [5, 6, 7, 8, 9, 13] is explored to analyze and implement control for a resonant converter in variable and constant frequency operation.

1.4 Optimal Trajectory Control

The optimal trajectory control of variable frequency series resonant converter proposed in [8] is based on state plane analysis [7] of the state variables of the resonant tank circuit: the inductor current and capacitor voltage. It uses appropriate state variable trajectories in a two-dimensional state plane as its desired trajectories. The control objective is to determine and switch the power switches at instants which would force the state variables to track their optimal (desired) trajectory in minimum time [9]. With this objective, the transients are kept to a minimum and the system reaches its steady state in minimum time with respect to these variables. Also the voltage and current swings are kept within bounds. However, as evident from [9], the optimal trajectory control structure is nonlinear and complex to implement. Its performance relies heavily on system parameters which can change during operation. In this respect, the OTC scheme as discussed in [8, 9] is not robust.

In [5], the dynamics of the variable frequency SRC operating at below resonant frequencies is further explored to improve the robustness of optimal trajectory control. In the process of simplification, the inherently nonlinear optimal trajectory control is shown equivalent to a modified form of capacitor voltage control with a pseudo-linear form. The simplified structure is shown to exhibit the decoupled dynamic characteristic of the SRC under optimal trajectory control. The theoretical results of [5] lead to a multirate control design which is presented and implemented in this thesis on an experimental SRC. Extensions of the results to above resonant frequency operation of the variable frequency SRC is also carried out in this thesis. Simulation and experimental results are presented and compared. The results demonstrate the superior dynamic performance of the proposed

Reproduced with permission of the copyright owner. Further reproduction prohibited without permission.

method with lesser implementation complexity. Furthermore, the controller so obtained is independent of the system parameters which are subject to change during operation and is therefore robust to changes in these parameters.

In [6] optimal trajectory control of a fixed frequency series resonant converter is proposed and simplified along the lines of [5]. Comparison of this method to other methods of control of the fixed frequency series resonant converter is made through simulations. Experiemental results, verifying the conclusions in [6] are lacking in the literature. This thesis verifies the theoretical conclusions of [6] experimentally on a fixed frequency series resonant converter.

1.5 Power Semiconductor Switches

In recent years, the field of power electronics has experienced a large growth. One of the reasons is the significant improvement of voltage and current ratings of power semiconductor devices and their faster switching-on and switching-off times. Switching frequency is one of the important considerations in choosing switches. Other characteristics such as thermal effects, ease of control and cost must also be considered [1].

In the experimental aspects of this thesis, MOSFETs (IRF540) are used as power switches. MOSFETs are voltage-controlled devices. This means, to keep MOSFETs in on-state, a continuous application of a gate-to-source voltage V_{GS} is required. To turn MOSFET on, V_{GS} must also be higher than a threshold value V_T.

As discussed above, MOSFETs are used as switches by controlling V_{GS}. If V_{GS} is lower than the threshold value V_T (2V for IRF540), MOSFETs are in off-state. Otherwise, if V_{GS} is significantly higher than V_T (10V for IRF540), MOSFETs are in on-state. This principle of operating MOSFETs poses the switching objective: a fast increasing or decreasing gate-to-source voltage is required to minimize switching time. Since the gate-source circuit is capacitive, the gate drive current determines how fast the gate-to-source capacitance is charged and discharged. The charging and discharging speed of gate-to-source capacitor indicates the rate of change in gate-to-source voltage. In other words, if a shorter switching on or off time is required, a fast changing large gate current must be supplied using the gate drive circuit. The detailed logic of gate drive circuits for the switching on and off of MOSFETS in this thesis are given in Appendix A.1.

ZCS and ZVS can reduce switch stresses. However, voltage spikes and oscillations across MOSFETs are always there during switching on and off due to stray inductances and the currents stored in them. In high current operation, the voltage spikes are very large and maybe higher than the maximum rating of drain-to-source voltage (100V for IRF540). These high spikes may damage the MOSFETs. To protect the MOSFETs, a snubber circuit can be used to bypass such currents during MOSFET turn off. Following preliminary testing as discussed in Appendix A.2, no snubbers were used in the resonant converter circuits of this thesis.

Reproduced with permission of the copyright owner. Further reproduction prohibited without permission.

1.6 Thesis Outline

As discussed in Section 1.3, resonant converters can overcome the drawbacks of conventional switched mode DC-DC converters. By using the modified optimal trajectory control of [5, 6] on series resonant converters, continuous measurements of inductor current is no longer required. Consequently the control complexity for series resonant converters is simplified and the system is robust to circuit parameter variations. The main contributions of this thesis are to experimentally evaluate and verify the theoretical and simulated results in [5, 6] thus greatly enhancing the applicability of these results.

Chapter 2 studies in the state-plane, a half-bridge series resonant converter in which the frequency of operation is variable with load. The application of modified robust optimal trajectory control along the lines of [5] is developed for this circuit in two modes of operation: below resonant frequency and above resonant frequency. In the prior literature only the below resonant frequency operation has been studied. Both simulation and experimental results are provided in this thesis to show the superior performance of modified optimal trajectory control for below and above resonant frequency of operation of the converter.

While the topology of the variable frequency series resonant converter studied in Chapter 2 is simple and has most of the advantages of resonant converters it emits a wideband of EMI due to its variable frequency operation. This wideband EMI is difficult to suppress. If the EMI is produced at a single frequency then it can be better suppressed more easily. Chapter 3 therefore studies in the state-plane, a more complex full bridge series resonant converter which is operated at a fixed frequency. Each of the two half-bridge arms of this converter are switched at the same frequency in the steady-state but with a phase shift between them. The phase shift controls the output voltage at various loads.

Optimal trajectory control for such fixed frequency series resonant converter was first proposed in [6] and simplified along the lines of [5] in [6]. In Chapter 3, the theoretical equations on maximum load that such converters can supply in steady-state, which were obtained in [6], are experimentally confirmed. Both simulation and experimental results on the performance of optimal trajectory control on such converters are provided in this Chapter to demonstrate its robustness and superior dynamic performance.

Chapter 4 concludes the thesis with suggestions for future work.

Reproduced with permission of the copyright owner. Further reproduction prohibited without permission.

Chapter 2

Optimal Trajectory Control of VF-SRC

2.1 Introduction

Optimal Trajectroy Control (OTC) scheme has been introduced in Section 1.4. In this Chapter. OTC will be applied for the control of variable frequency series resonant converter (VF-SRC). VF-SRC uses the half bridge circuit configuration shown below[16] in Figure 2.1. It is capable of being operated below or above the resonant frequency $\omega_0=1/\sqrt{LC}$. These modes of operation are therefore called below resonant frequency and above resonant frequency operation, respectively.

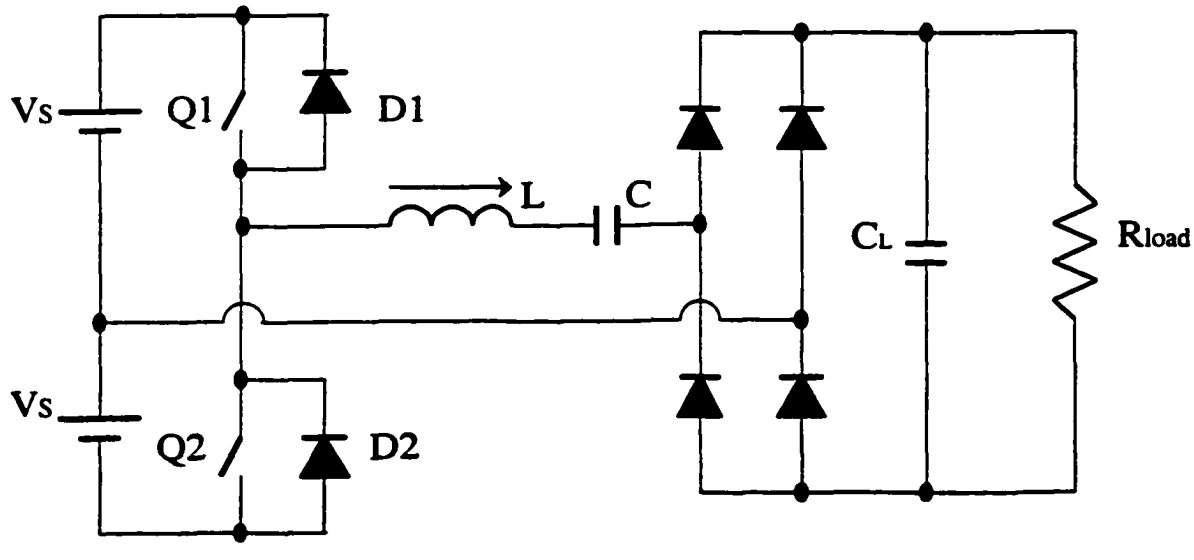

Figure 2.1: Variable Frequency SRC circuit

In this Chapter, state-space analysis is used in the design and implementation of optimal trajectory control scheme for both below and above resonant frequency operation.

Reproduced with permission of the copyright owner. Further reproduction prohibited without permission.

2.2 State Plane Analysis of Series Resonant Converters

Traditional DC-DC power conversion has been based upon the use of switch mode circuits. As mentioned in Section 1.3.1, PWM converters have some drawbacks. These drawbacks become more significant when switching frequency is increased in order to increase power density and decrease equipment size. In contrast with PWM converters, resonant converters can overcome these shortcomings by using zero-voltage switching (ZVS) and/or zero-current switching (ZCS). Study of the VF-SRC is based on state plane analysis which is introduced in the next subsection.

2.2.1 State Plane Analysis

The analysis of resonant converters is normally accomplished by identifying the circuit modes of the converter during a switching cycle and solving the associated differential equation with the appropriate boundary conditions associated with transitions between these modes. This is a time consuming process for obtaining a steady state solution. A simpler technique for obtaining steady-state solution is using the state plane diagram, where the state variables in each mode are graphed by recognizing the associated steady-state trajectories in each mode. Once the state plane diagram is obtained, the steady state solution in the time domain for all modes of operation can be found quickly and easily, as introduced in [7, 11]. State plane analysis is a simple and powerful method to study resonant converters. It is widely used in the analysis and control of DC-DC converters, as in [5, 6, 7, 10, 11]. To study resonant converters through state plane diagram, state equations are studied to determine the switching strategy based on the converter dynamics.

For the series resonant converter in Figure 2.1 with a single L and a single C, the state plane is a two dimensional plane. In a second order system, by using the inductor current and capacitor voltage of the resonant tank circuit as the two coordinates of the state plane, both large signal dynamics and steady state operation of the converter can be graphically represented on the state plane. To simplify the analysis, it is assumed that the output filter capacitor C_L is sufficiently large so that the output voltage V_0 measured across C_L is constant over a complete switching cycle and the resistance of the tank circuit is negligible. According to the direction of i_L, four topological modes exist, as shown in Figure 2.2.

As i_L=i_C in Figure 2.1 the following state equations, with i_L and v_C as state variables, can be written for the topological modes of the circuit:

$$\frac{dv_C}{dt} = \frac{1}{C} i_L \tag{2.1}$$

$$\frac{di_L}{dt} = -\frac{1}{L} v_C + \frac{1}{L} V_E \tag{2.2}$$

In Equation 2.2, V_E is the instantaneous DC voltage across the series inductor and capacitor in the topological modes shown in Figure 2.2. V_E is given in Table 2.1 for each topological mode shown in Figure 2.2. Equations 2.1 and 2.2 can be represented in a

Reproduced with permission of the copyright owner. Further reproduction prohibited without permission.

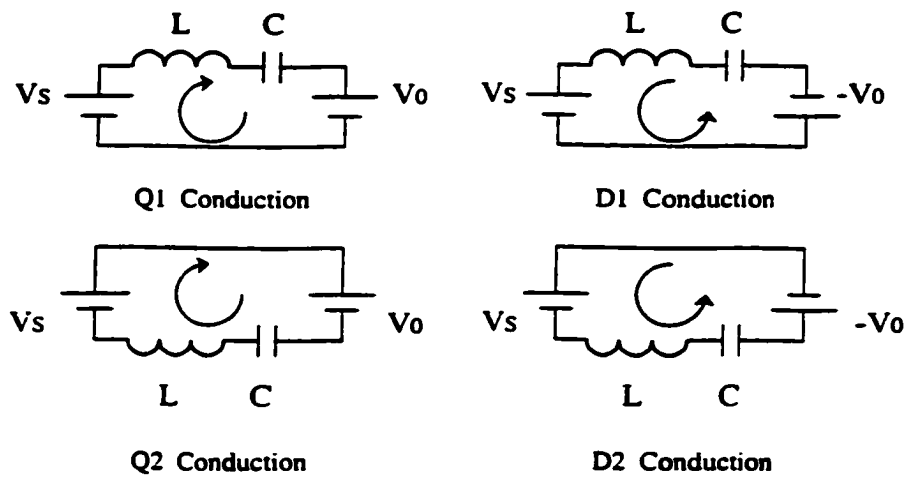

Figure 2.2: Topological Modes of Variable Frequency SRC

Conduction mode	V_E
Q1 conduction	$V_s - V_0$
D1 conduction	$V_s + V_0$
Q2 conduction	$-V_s + V_0$
D2 conduction	$-V_s - V_0$

Table 2.1: Equivalent Circuit DC Voltage

matrix form by the following state equation for the VF-SRC circuit shown in Figure 2.1:

$$\begin{bmatrix} \dot{v_C} \\ \dot{i_L} \end{bmatrix} = \begin{bmatrix} 0 & \frac{1}{C} \\ -\frac{1}{L} & 0 \end{bmatrix} \begin{bmatrix} v_C \\ i_L \end{bmatrix} + \begin{bmatrix} 0 \\ \frac{1}{L} \end{bmatrix} V_E \tag{2.3}$$

Solving Equation (2.3) with initial conditions, the variation of the two state variables in the time domain in any topological mode of this circuit can be obtained as:

$$\begin{aligned} v_C &= I_{L0} Z_0 sin(\omega_0(t - t_0)) + (V_{C0} - V_E) cos(\omega_0(t - t_0)) + V_E \\ Z_0 i_L &= I_{L0} Z_0 cos(\omega_0(t - t_0)) - (V_{C0} - V_E) sin(\omega_0(t - t_0)) \end{aligned}$$

where I_{L0} is the initial inductor current on entering the topological mode, V_{C0} is the initial capacitor voltage on entering the topological mode, Z_0 is the characteristic impedance, ω_0 is the resonant frequency and t_0 is the initial time at entry to the mode. To simplify the solutions, all of the voltages are normalized by dividing by V_S, all of the currents are normalized by multiplying by Z_0 and then dividing by V_S. Finally with $\theta_0 = \omega_0(t - t_0)$, the following normalized solutions can be obtained:

$$v_{CN} - V_{EN} = I_{L0N} sin(\theta_0) + (V_{C0N} - V_{EN}) cos(\theta_0) \tag{2.4}$$

$$i_{LN} = I_{L0N} cos(\theta_0) - (V_{C0N} - V_{EN}) sin(\theta_0) \tag{2.5}$$

where the "N" in subscripts indicates normalized quantities.

Reproduced with permission of the copyright owner. Further reproduction prohibited without permission.

From Equations (2.4) and (2.5), the following Equation is readily derived:

$$i_{LN}{}^2 + (v_{CN} - V_{EN})^2 = I_{L0N}{}^2 + (V_{C0N} - V_{EN})^2 \tag{2.6}$$

From Equation (2.6), we recognize that the trajectories for the topological modes of the VF-SRC represent a set of circles in the state plane of the normalized instantaneous capacitor voltage v_{CN} and inductor current i_{LN}. The centers of these circles are determined by the instantaneous voltage across the tank circuit (V_{EN}) in the corresponding topological mode. The coordinates of the centers in this plane are given by:

Q1 conduction $(V_{SN} - V_{0N}, 0)$ D1 conduction $(V_{SN} + V_{0N}, 0)$

Q2 conduction $(-V_{SN} + V_{0N}, 0)$ D2 conduction $(-V_{SN} - V_{0N}, 0)$

By combining the appropiate arcs of these circular trajectories into a state portrait, the trajectory of SRC operation can be characterized for a given input voltage, output voltage and load condition.

Note that in the above V_{SN}=1, but is retained as V_{SN} and not changed to 1 since in the control aspects of the SRC, the actual input voltage V_S can change but the normalizing voltage which acts as a numerical scaler does not change. Hence V_{SN} can change from 1.

2.3 Optimal Trajectory Control of VF-SRC

As mentioned in Section 2.1, the VF-SRC can be operated below or above resonant frequency. In this Section, OTC scheme and control laws will be developed for both below and above resonant frequency operation. In the next Section, the control laws will be simplified and set into the context of the literature.

2.3.1 Control Laws

At below resonant frequency operation ($\omega_s < \omega_0$), the typical normalized capacitor voltage and inductor current waveforms are shown in Figure 2.3, where i_{LN} is leading v_{CN} and four conduction modes are marked. Q1 turns off naturally when inductor current reverses (turns negative in Figure 2.3).The current then flows through D1. In this continuous mode, D1 conducts for a short time before Q2 is turned on. Similarly, when Q2 turns off, D2 conducts for a short while before Q1 is turned on. In this mode of operation, the switches turn off when the current through them naturally reduces to zero, but they turn on at a finite current and at a finite voltage drop across them, thus resulting in switching loss when the switches are turned on.

At above resonant frequency operation ($\omega_s > \omega_0$), the typical waveforms are shown in Figure 2.4 where i_{LN} is also leading v_{CN} and four conduction modes are marked. Compared with the previous below resonant frequency operation, where the switches turn off naturally but turn on at a finite current, the switches in the above resonant frequency operation are forced to turn off at a finite current, but they are turned on at zero current. As shown in Figure 2.4, after D2 conducts for some time, when current reverses naturally, Q2 is switched on and inductor current flows through it. Q2 is forced to turn off a little later in the trajectory, thus forcing the negative inductor current to flow

Reproduced with permission of the copyright owner. Further reproduction prohibited without permission.

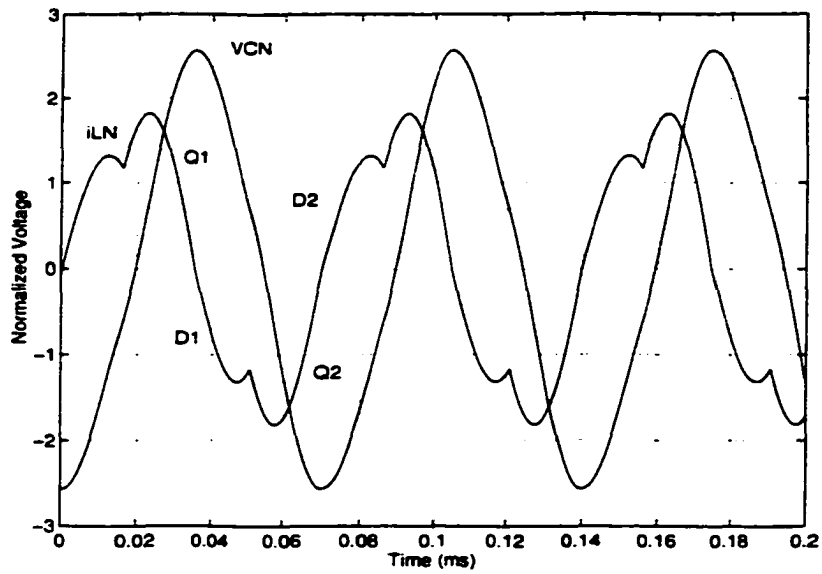

Figure 2.3: Waveforms of i_L and v_C in Below Resonant Frequency Operation

through D1. When the current again reverses direction, Q1 is turned on and is switched off a little later in the trajectory forcing current to flow through D2.

Optimal trajectory control of variable frequency series resonant converter is based on state plane analysis of the instantaneous inductor current and capacitor voltage [5, 7, 8, 9]. The state equation of variable frequency SRC and its solutions were given in Section 2.2.1. From the normalized solution (Equation 2.6), we understand that the trajectory of state variables in state plane diagram is a set of semi-circles with different centers depending on different topological modes. The control objective is to force the two state variables to track the desired steady-state trajectory in the state plane diagram such that it takes minimum time from one steady state to another steady state. Figures 2.5 and 2.6 are state plane, steady state trajectories showing the operation of SRC in continuous conduction mode below and above the resonant frequency of the tank circuit for a normalized output voltage V_{0N}=0.25 (Normalized by V_S) with R_{Load}=0.22 (Normalized by $Z_0=\sqrt{L/C}$). The four centres in Table 2.1 are also shown in these two Figures.

For below resonant frequency operation in Figure 2.5, the optimal trajectory control law determines using the desired trajectory of state variables when the switches(MOSFETs) Q1 and Q2 are to be turned on into conduction. Q1 and Q2 are switched off at the instants when the current through them reduces to zero naturally (ZCS). The radius r, measured from a point on the trajectory to a corresponding center is continuously monitored and compared with the desired radius R. The MOSFETs are turned on when r$\leq$R, as shown in Figure 2.5. In this Figure, r and R are marked only for the switching on of Q2. A similar symmetrical procedure is followed for the switching on of Q1.

From Figure 2.5, we obtain Equations (2.7) and (2.8) which give the law for switching Q1 and Q2 on at below resonant frequency [8, 9].

Reproduced with permission of the copyright owner. Further reproduction prohibited without permission.

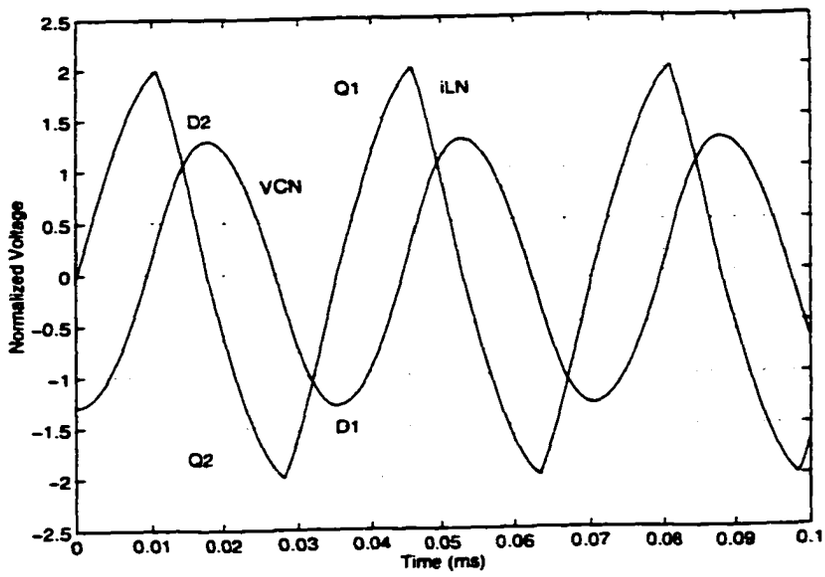

Figure 2.4: Waveforms of i_L and v_C in Above Resonant Frequency Operation

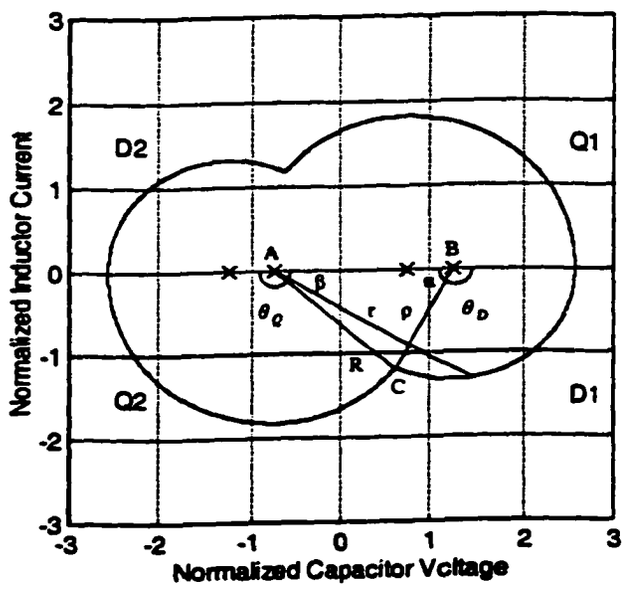

Figure 2.5: Steady State Trajectory of Below Resonant Frequency Operation

Reproduced with permission of the copyright owner. Further reproduction prohibited without permission.

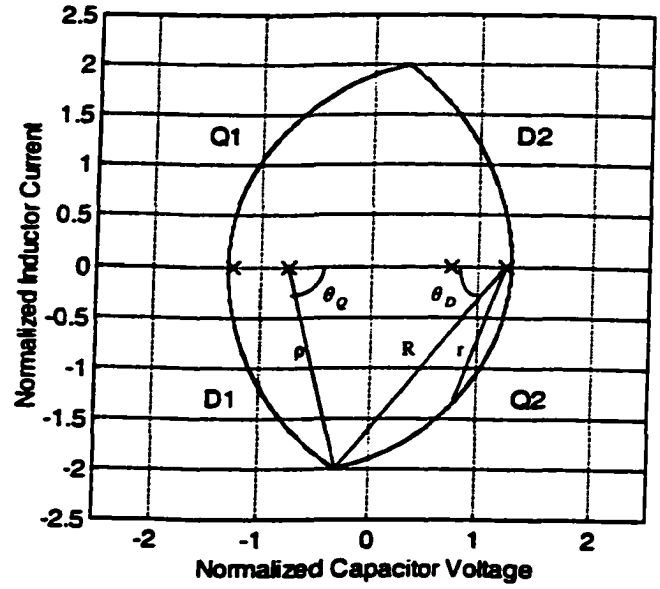

Figure 2.6: Steady State Trajectory of Above Resonant Frequency Operation

$$r^2 = (v_{CN} + V_{SN} - V_{0N})^2 + i_{LN}^2 \leq R^2 \qquad \textit{For switching Q2 on} \tag{2.7}$$

$$r^2 = (v_{CN} - V_{SN} + V_{0N})^2 + i_{LN}^2 \leq R^2 \qquad \textit{For switching Q1 on} \tag{2.8}$$

Combining Equations (2.7) and (2.8), Equation (2.9) is obtained:

$$(\pm v_{CN} + V_{SN} - V_{0N})^2 + {i_{LN}}^2 \leq R^2 \tag{2.9}$$

For above resonant frequency operation in Figure 2.6. the optimal trajectory control law determines using the desired trajectory when the switches Q1 and Q2 are to be turned off. The switches are turned on immediately after the current in the corresponding diode D1 and D2 respectively reduces to zero (ZCS). The radius r, measured from a point on the trajectory to a corresponding center is continuously monitored and compared with the desired radius value R. The switches are turned off when r≥R, as shown in Figure 2.6. In this Figure, r and R are marked only for the turning Q2 off. A similar symmetrical procedure is followed in the turning Q1 off.

From Figure 2.6, we obtain Equations (2.10) and (2.11) which give the control law for switching Q1 and Q2 off at above resonant frequency.

$$r^2 = (v_{CN} - V_{SN} - V_{0N})^2 + i_{LN}^2 \geq R^2 \qquad \textit{For switching Q2 off} \tag{2.10}$$

$$r^2 = (v_{CN} + V_{SN} + V_{0N})^2 + i_{LN}^2 \geq R^2 \qquad \textit{For switching Q1 off} \tag{2.11}$$

Combining Equations (2.10) and (2.11), Equation (2.12) is obtained:

$$(\pm v_{CN} + V_{SN} + V_{0N})^2 + i_{LN}^2 \geq R^2 \tag{2.12}$$

Reproduced with permission of the copyright owner. Further reproduction prohibited without permission.

Equations (2.9) and (2.12) give the control laws for below and above resonant frequency operation of the VF-SRC respectively. These control laws require continuous high bandwidth measurement of inductor current, scaling it by Z_0/V_S and squaring calculation. Following [5], they will be simplified in the next Section.

2.3.2 Design Considerations

Several issues from design perspective have to be considered as follows:

1. The optimal trajectory control provides fast response of the state variables once the desired radius R is determined. However, in applications where the output voltage V_0 is to be regulated, it is difficult to determine R directly and instantaneously. R is typically set by an outer control loop by sensing V_0, comparing it with a reference V_{ref} and processing the error through a controller. Hence the overall speed of response of the SRC under optimal trajectory control is limited by the performance of the outer control loop which in turn is influenced by the dynamics of the SRC's output section. This has not been considered in the literature [5, 6, 7, 8, 9, 12].

2. From Figure 2.5, the conduction angles of diodes and switches θ_D and θ_Q can be calculated as follow. In triangle ABC in Figure 2.5:

$$\begin{aligned} \alpha &= 180 - \theta_D \\ \beta &= 180 - \theta_Q \\ \rho &= V_{C0N} - V_{SN} - V_{0N} \\ \mathrm{R} &= V_{C0N} - V_{SN} + V_{0N} \end{aligned}$$

Therefore, the following results can be obtained:

$$\begin{aligned} cos\theta_D &= -\cos\alpha \\ cos\theta_Q &= -\cos\beta \\ \rho &= R - 2V_{0N} \\ \mathrm{AB} &= 2V_{SN} \end{aligned}$$

From the above Equations and cosine rule for triangles, α and β can be given as:

$$\cos\alpha = \frac{(R-2V_{0N})^2 + (2V_{SN})^2 - R^2}{2(R-2V_{0N})(2V_{SN})} = -\cos\theta_D \tag{2.13}$$

$$\cos\beta = \frac{(2V_{SN})^2 + R^2 - (R-2V_{0N})^2}{2R(2V_{SN})} = -\cos\theta_Q \tag{2.14}$$

Rearranging the above two Equations, the following Equations are obtained:

$$\cos\theta_D = \frac{V_{0N}R - {V_{SN}}^2 - {V_{0N}}^2}{V_{SN}(R-2V_{0N})} \quad \text{Below resonant frequency} \tag{2.15}$$

$$\cos\theta_Q = \frac{{V_{0N}}^2 - {V_{SN}}^2 - V_{0N}R}{V_{SN}R} \quad \text{Below resonant frequency} \tag{2.16}$$

Reproduced with permission of the copyright owner. Further reproduction prohibited without permission.

Using the same approach, from Figure 2.6, the conduction angles at above resonant frequency operation are obtained as below:

$$\cos\theta_D = \frac{V_{0N}R + V_{SN}{}^2 - V_{0N}{}^2}{V_{SN}R} \quad \text{Above resonant frequency} \tag{2.17}$$

$$\cos\theta_Q = \frac{V_{SN}{}^2 + V_{0N}{}^2 - V_{0N}R}{V_{SN}(R - 2V_{0N})} \quad \text{Above resonant frequency} \tag{2.18}$$

The average rectified normalized cycle current, $|\bar{i}_{LN}|$ of the SRC under optimal trajectory control can be calculated by integrating with respect to conduction angles of diodes and MOSFETs. At below resonant frequency operation, the integral of inductor current during Q1 conduction can be calculated as:

$$i_{LNQ} = \int_0^{\theta_Q} R\sin\theta d\theta = R(1-\cos\theta_Q) = \frac{RV_{SN} + V_{SN}{}^2 + RV_{0N} - V_{0N}{}^2}{V_{SN}} \tag{2.19}$$

The integral of inductor current during D2 conduction can be calculated as:

$$\begin{aligned} i_{LND} &= \int_0^{\theta_D} \rho\sin\theta d\theta = (R - 2V_{0N})(1-\cos\theta_D) \\ &= \frac{RV_{SN} - 2V_{0N}V_{SN} - RV_{0N} + V_{SN}{}^2 + V_{0N}{}^2}{V_{SN}} \end{aligned} \tag{2.20}$$

Therefore, the average inductor current in a half cycle is:

$$\begin{aligned} |\bar{i}_{LN}| &= \frac{i_{LND} + i_{LNQ}}{\theta_Q + \theta_D} \\ &= \frac{2(R + V_{SN} - V_{0N})}{\theta_Q + \theta_D} \quad \textit{Below resonant frequency} \end{aligned} \tag{2.21}$$

Likewise, at above resonant frequency operation, the average inductor current in a half cycle is:

$$\begin{aligned} |\bar{i}_{LN}| &= \frac{i_{LND} + i_{LNQ}}{\theta_Q + \theta_D} \\ &= \frac{2(R - V_{SN} - V_{0N})}{\theta_Q + \theta_D} \quad \textit{Above resonant frequency} \end{aligned} \tag{2.22}$$

In Figures 2.5 and 2.6, for fixed V_{0N} and V_{SN}, as R is increased, the switches are turned on soon after the diodes conduct (in Figure 2.5) or turned off quite late before

Reproduced with permission of the copyright owner. Further reproduction prohibited without permission.

diodes conduct (in Figure 2.6). In both cases as R increases, only switches conduct (θ_Q approaches π), the diodes conduct for a very short time (θ_D approaches zero). Thus $\theta_D + \theta_Q$ approaches π. Therefore, asymptotically for large R, the expressions of Equations (2.21) and (2.22) become linear in R with a positive slope.

The frequency of the SRC at both below and above resonant frequency operation in steady state is given by:

$$f = \frac{\omega_0}{2(\theta_D + \theta_Q)} \tag{2.23}$$

3. In Figure 2.5, if $\theta_D = \pi$, it means that Q2 is not turned on until the diode current i_D falls to zero. On the other hand, if Q2 is switched on when i_D=0, and conducts until the current through it is about to reverse, then $\theta_Q = \pi$. Substituting $\theta_D = \pi$ into Equations (2.15) or $\theta_Q = \pi$ into Equation (2.16), the minimum value of R for continuous conduction mode of operation in the steady state below resonant frequency is obtained as $R_{min} = V_{SN} + V_{0N}$. For this minimum value of R, from Equation (2.21), $|\bar{i}_{LN}|$=$2V_{SN}/\pi$. This corresponds to a maximum load resistance (in Ohms) of R_{Lmax}=$V_{0N}Z_0\pi/2V_{SN}$. For load resistances greater than this value, the SRC operates in discontinuous conduction mode and the optimal trajectory control should be augmented by an appropriate time-variant control to take over the operation of the SRC in the discontinuous mode. At this maximum load resistance value, the SRC in continuous conduction mode is operating in the steady state at its minimum frequency of half the natural resonant frequency.

   Likewise from Figure 2.6, for operation above resonant frequency the minimum value of R is $V_{SN} + V_{0N}$ as well. For this value of R, the entire steady state trajectory coincides with the origin and therefore $|\bar{i}_{LN}|$=0. This seems to allow for no load to be imposed on the SRC but requires infinite switching frequency. Therefore, a minimum load is needed for the SRC operating above resonance.

4. Expressions for the short circuit $|\bar{i}_{LN}|$ for the below and above resonant frequency operation of the SRC can be obtained as (R+V_{SN})/cos^{-1}(−V_{SN}/R) from Equations (2.15), (2.16) and (2.21) or (R−V_{SN})/cos^{-1}(V_{SN}/R) from Equations (2.17), (2.18) and (2.22) respectively by setting $V_{0N} = 0$ in these Equations.

2.3.3 Implementation Issues

Analog implementation of the control law of Equations (2.9) and (2.12) is presented in [9]. This implementation extensively highlights the complexity of optimal trajectory control of the SRC. The following factors contribute to complexity and poor robustness of the direct implementation of Equations (2.9) and (2.12).

1. The control law has a nonlinear form. It needs continuous measurement of v_C and i_L and continuous squaring operation of variables derived from the instantaneous values of v_C and i_L. The sensors measuring v_C and i_L should have a high slew rate (high bandwith) and the multipliers performing the squaring operation should have large

Reproduced with permission of the copyright owner. Further reproduction prohibited without permission.

bandwidth. This greatly increases the cost of control. Conversely the achievable SRC operational frequency is limited by the slew rate of the sensors and the bandwidth of the multipliers.

2. i_{LN} needs to be computed continuously by scaling the measured i_L by the characteristic impedance Z_0 of the resonant tank circuit. This requires precise knowledge of the ratio of the parameters L and C of the resonant tank circuit of the SRC. More significantly, during operation due to effects such as inductor saturation and thermal effects, this ratio is prone to vary, contributing to poor robustness of this method. A change in this ratio introduces significant errors which undermine the advantages of optimal trajectory control.

To overcome the issues raised above, the control laws of Equations (2.9) and (2.12) will be simplified in the next Section.

2.4 Modified Capacitor Voltage Technique

Control of SRC by using a linear capacitor voltage control law has been studied in [8]. In this Section, it is shown that the optimal trajectory control law can be simplified to a modified capacitor voltage control with a pseudo-linear form [5]. The proposed simplification in [5] greatly reduces the implementation complexity of optimal trajectory control for series resonant converter by avoiding continuous measurements and squaring calculations of i_{LN}.

2.4.1 Robust Optimal Trajectory Control

As discussed in Section 2.3.3, the OTC studied in [8, 9] is not robust because it requires continuous v_C, i_L measurements and exact knowledge of circuit parameters which are subject to vary during converter operation. Also, i_L measurement at high frequencies is costly. If this measurement requirement is eliminated then the scaling operation by the characteristic impedance of the tank circuit of the SRC also vanishes from the OTC laws and the resultant modified OTC laws will be robust. In this Section, the control laws in Section 2.3.1 will be simplified to get rid of i_{LN}, so that the modified OTC scheme does not require high bandwidth measurement of current and is robust to circuit parameter variations.

Control Law Simplification for Below Frequency Operation

The semicircular shape of the trajectory during diode conduction and zero initial value of the inductor current at the start of diode conduction can be exploited to simplify the control law given in Equation (2.9). From Figure 2.5, any point on the trajectory when D1 conducts can be described by:

$$(v_{CN} - V_{SN} - V_{0N})^2 + {i_{LN}}^2 = \rho^2 = (V_{C0N+} - V_{SN} - V_{0N})^2 \tag{2.24}$$

Reproduced with permission of the copyright owner. Further reproduction prohibited without permission.

Where V_{C0N+} is the positive peak value of capacitor voltage. Therefore,

$$\begin{aligned} {i_{LN}}^2 &= (V_{C0N+} - V_{SN} - V_{0N})^2 - (v_{CN} - V_{SN} - V_{0N})^2 \\ &= (V_{C0N+} - V_{0N})^2 - (v_{CN} - V_{0N})^2 + 2V_{SN}(v_{CN} - V_{C0N+}) \end{aligned} \tag{2.25}$$

By using Equation (2.25), i_{LN} can be eliminated from Equation (2.9) for switching on Q2 to obtain:

$$4V_{SN}(v_{CN} - V_{0N}) + (V_{C0N+} - V_{SN} - V_{0N})^2 \leq R^2 \tag{2.26}$$

Likewise, the condition for turning Q1 on can be obtained as:

$$-4V_{SN}(v_{CN} + V_{0N}) + (V_{C0N-} + V_{SN} + V_{0N})^2 \leq R^2 \tag{2.27}$$

Where V_{C0N-} is the negative peak value of capacitor voltage. Equations (2.26) and (2.27) can be combined into a single switching rule given in Equation (2.28):

$$4V_{SN}(\pm v_{CN} - V_{0N}) + (V_{SN} + V_{0N} - \mid V_{C0N} \mid)^2 \leq R^2 \tag{2.28}$$

The + sign in Equation (2.28) applies to Q2 being turned on while the − sign applies to Q1, with $\mid V_{C0N} \mid = \mid V_{C0N+} \mid$ or $\mid V_{C0N-} \mid$, the magnitude of the peak capacitor voltage in the appropriate half cycle.

Control Law Simplification for Above Frequency Operation

From Figure 2.6, any point on the trajectory when Q2 is conducting can be described by:

$$(v_{CN} + V_{SN} - V_{0N})^2 + {i_{LN}}^2 = \rho^2 = (V_{C0N+} + V_{SN} - V_{0N})^2 \tag{2.29}$$

Using the same approach as above, i_{LN} can be eliminated from Equation (2.12) by using Equation (2.29) to obtain Equation (2.30) for turning Q2 off.

$$-4V_{SN}(v_{CN} - V_{0N}) + (V_{C0N+} + V_{SN} - V_{0N})^2 \geq R^2 \tag{2.30}$$

Likewise, the condition for turning Q1 off can be obtained as:

$$4V_{SN}(v_{CN} + V_{0N}) + (V_{C0N-} - V_{SN} + V_{0N})^2 \geq R^2 \tag{2.31}$$

Equations (2.30) and (2.31) can be combined into a single switching rule given in Equation (2.32):

$$4V_{SN}(\pm v_{CN} + V_{0N}) + (\mid V_{C0N} \mid + V_{SN} - V_{0N})^2 \geq R^2 \tag{2.32}$$

Reproduced with permission of the copyright owner. Further reproduction prohibited without permission.

where − sign applies to Q2 being turned off while the + sign applies to Q1. with $| V_{C0N} | = | V_{C0N+} |$ or $| V_{C0N-} |$, the magnitude of the peak capacitor voltage in the appropriate half cycle.

In Equations (2.28) and (2.32), the normalized current i_{LN} has been eliminated. Equations (2.28) and (2.32) will be referred to as modified capacitor voltage form of the OTC laws. The reason for this name and the context of these Equations visavis the literature is discussed in the next subsection. To implement the new modified capacitor voltage control laws of Equations (2.28) and (2.32), there is no need to measure i_L. More significantly, there is no need to scale i_L by Z_0 and hence the control law does not require the precise knowledge of the circuit parameters L and C of the resonant tank circuit of the SRC. This makes the modified capacitor voltage form of the OTC laws robust to circuit parameter changes. However, the sign of i_{LN} is still needed to determine whether Q1 or Q2 is to be switched on or off. Obtaining sign of i_{LN} however is much more cheaper than measuring it at every instant accurately.

2.4.2 Multirate Modified Capacitor Voltage Control Strategy

In this subsection, it is shown that Equations (2.28) and (2.32) can be thought of as a multirate modified capacitor voltage feedback control strategy.

In Equations (2.28) and (2.32), we observe that during a half cycle of a trajectory, V_{C0N} is a constant equal to the peak value of capacitor voltage at the start of the half cycle. In such a half cycle, the dynamics of V_{SN} and V_{0N} can be neglected as the switching frequency of the converter is much higher than the dynamics of V_{SN} or the filtered V_{0N}. Therefore, within a half cycle, the left hand side of Equations (2.28) and (2.32) vary linearly with the instantaneous capacitor voltage v_{CN}. Consequently, the optimal trajectory control law of [5] is a modified form of (instantaneous, linear) capacitor voltage control law studied in [8] with a quadratic function of V_{C0N} being added at each half cycle to the linear capacitor voltage control law of [8]. Hence Equations (2.28) and (2.32) are referred to as modified capacitor voltage control form of the OTC laws [5]. In the sense that the modification to the linear control law is done once every half cycle, the optimal trajectory control law has a pseudo-linear multirate form developed below.

The control law in Equation (2.28) can be expanded as:

$$4V_{SN}(\pm v_{CN}) - 4V_{SN}V_{0N} + (V_{SN} + V_{0N})^2 + | V_{C0N} |^2 - 2(V_{SN} + V_{0N}) | V_{C0N} | \leq R^2$$

The expansion can be simplified to:

$$4V_{SN}(\pm v_{CN}) + (V_{SN} - V_{0N})^2 + | V_{C0N} |^2 - 2(V_{SN} + V_{0N}) | V_{C0N} | \leq R^2$$

Letting $K_1 = 4V_{SN}$, $K_{2_1} = (V_{SN} - V_{0N})^2$ and defining a quadratic function $f_1(x)$ as $f_1(x) = x^2 - 2(V_{SN} + V_{0N})x$, then with $f_1(| V_{C0N} |) = | V_{C0N} |^2 - 2(V_{SN} + V_{0N}) | V_{C0N} |$, Equation (2.28) can be written as:

$$\pm K_1 v_{CN} + K_{2_1} + f_1(| V_{C0N} |) \leq R^2$$

The first term in the above Equation ($K_1 v_{CN}$) is the instantaneous linear feedback term while $f_1(| V_{C0N} |)$ is updated every half cycle. K_{2_1} and K_1 are updated at a far slower pace and can be considered as constants for the two previous terms of the Equation.

Reproduced with permission of the copyright owner. Further reproduction prohibited without permission.

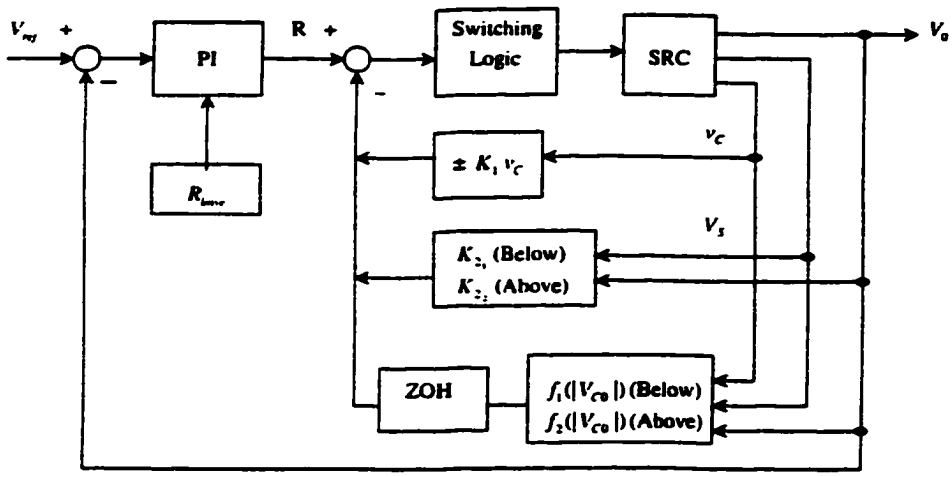

Figure 2.7: Multirate Control Strategy

The control law in Equation (2.32) can be expanded as:

$$4V_{SN}(\pm v_{CN}) + 4V_{SN}V_{0N} + (V_{SN} - V_{0N})^2 + \mid V_{C0N} \mid^2 + 2(V_{SN} - V_{0N}) \mid V_{C0N} \mid \geq R^2$$

This expansion can be simplified to:

$$4V_{SN}(\pm v_{CN}) + (V_{SN} + V_{0N})^2 + \mid V_{C0N} \mid^2 + 2(V_{SN} - V_{0N}) \mid V_{C0N} \mid \geq R^2$$

Letting $K_1 = 4V_{SN}$, $K_{2_2} = (V_{SN} + V_{0N})^2$ and defining a quadratic function $f_2(x)$ as $f_2(x) = x^2 + 2(V_{SN} - V_{0N})x$, then with $f_2(\mid V_{C0N} \mid) = \mid V_{C0N} \mid^2 + 2(V_{SN} - V_{0N}) \mid V_{C0N} \mid$, Equation (2.32) can be rewritten as:

$$\pm K_1 v_{CN} + K_{2_2} + f_2(\mid V_{C0N} \mid) \geq R^2$$

As before, the first term in the above Equation ($K_1 v_{CN}$) is the instantaneous linear feedback term while $f_2(\mid V_{C0N} \mid)$ is updated every half cycle. K_{2_2} and K_1 are updated at a far slower pace and can be considered as constants for the two previous terms of the Equation.

The discussion above shows that both Equations (2.28) and (2.32) have a similar multirate control structure depicted in the inner feedback loops of Figure 2.7.

In Figure 2.7, the inner loops for $\pm K_1 v_{CN}$ and K_{2_1} or K_{2_2} are in continuous operation. The third loop for $f_1(\mid V_{C0N} \mid)$ or $f_2(\mid V_{C0N} \mid)$ is updated at the beginning of each half cycle. The outermost loop in Figure 2.7 is a PI controller to generate R based on V_0 and V_{ref}. The rationale for the choice of a PI controller for this loop is discussed in the next subsection.

In the simulations reported later in Section 2.5.1, the outermost loop updates R at the beginning of every half cycle while in laboratory implementations reported in Section 2.5.2, this loop is implemented with an analog PI controller in continuous time.

Reproduced with permission of the copyright owner. Further reproduction prohibited without permission.

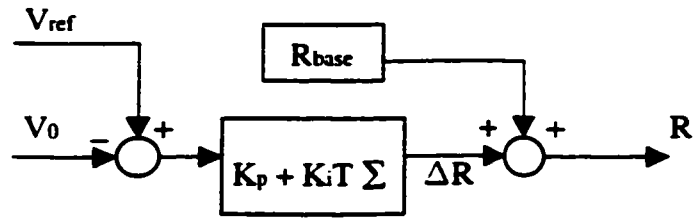

Figure 2.8: PI controller of outermost loop

2.4.3 Outermost Loop Controller

While optimal trajectory control guarantees the stability of the SRC with reference to the innermost and middle loops of Figure 2.7 assuming R is available, the controller in the outermost loop in Figure 2.7 which computes R has to be designed properly using the two final signals of interest in the SRC, V_0 and V_{ref}.

Assuming that the output capacitor C_L is large, an adequate model of the output filter stage of the SRC for discussing the design of the controller in the outermost loop is given by the following discretized recursive equation [5]:

$$V_0(n+1) = V_0(n)[1 - \frac{T}{R_L C_L}] + \frac{T \mid \bar{i}_{LN} \mid}{C_L} \tag{2.33}$$

In Equation (2.33), T is the nominal half period of operation of the SRC and n is the half cycle number. R_L is the load resistance.

From Equations (2.21), (2.22) and discussions following it in Section 2.3.2, we know that $|\bar{i}_{LN}|$ is related linearly to V_0 and R for large R. Using this knowledge and from Equation (2.33) it now becomes clear that the outermost loop controller should have a proportional controller with proportional gain so as to produce large changes in the value of R for small changes in V_0 within stability limits. To ensure tracking of the reference voltage V_{ref}, an integral controller is also needed. Therefore in this thesis, the controller in the outermost loop is a PI controller depicted in Figure 2.8. K_p and K_i in Figure 2.8 are proportional and integral gains and can be chosen to achieve the desired transient performance within stability margins of the SRC. R_{base} in Figure 2.8 is a constant parameter to offset R and allow the output of the controller to swing around R_{base}. For example, R_{base} can be chosen using Equations (2.21) and (2.22) to provide half the rated load current under no control action. With this R_{base}, ΔR assumes nearly the same range of variation in both positive and negative directions for the full range of load.

2.5 Results

The performance of the modified capacitor voltage control form of OTC as per Equations (2.28) and (2.32) with the outermost loop under PI control (Figure 2.7) is studied in this

Reproduced with permission of the copyright owner. Further reproduction prohibited without permission.

Section first by simulations and then on an experimental SRC with the same nominal parameters as that studied in the simulations.

2.5.1 Simulation Results

Before the control laws are implemented in the lab, they are simulated in a computer using C programming language with the model of the SRC developed in Equation (2.4), (2.5) and (2.33). Switches are considered ideal in these simulations. The resonant tank circuit is assumed to have no resistance. The parameter values used in simulations are listed in Table 2.2. In Table 2.2, all parameters are unnormalized. Normalized values of appropriate parameters are indicated in brackets.

V_S	20V (1)	V_0	5V (0.25)
L	$88.6\mu H$	C	$0.68\mu F$
C_L (Below)	$470\mu F$	C_L (Above)	$470\mu F$
Z_0	11.46Ω (1)	f_0 (Resonant)	20.5kHz
R_{Load} (Low Current)	2.5Ω (0.22)	R_{Load} (High Current)	1.25Ω (0.11)
f_S (Below) Steady State $R_{Load} = 2.5\Omega$	13.9kHz	f_S (Above) Steady State $R_{Load} = 2.5\Omega$	27.8kHz
f_S Range (Below)	13.9~17.881KHz	f_S Range (Above)	24.245~27.8KHz
P gain (Below)	100	I gain (Below)	650000
P gain (Above)	100	I gain (Above)	550000
R_{base} (Below)	31V (1.55)	R_{base} (Above)	24V (1.2)

Table 2.2: Simulation Parameters for VF-SRC

Simulation of Below Resonant Frequency Operation

Figure 2.9 shows the waveforms of the simplified control law of Equation (2.28) at steady state to determine the instants of turning the switches Q1 and Q2 on. In this Figure, $a = R^2 - (V_{SN} + V_{0N} - \mid V_{C0N} \mid)^2$ and $b = 4V_{SN}(\pm v_{CN} - V_{0N})$. According to the control law, if $a \geq b$, Q1(Q2) will be turned on. By using this switching signal, the steady state results in the time domain and in the state plane diagram shown in Figures 2.3 and 2.5 were produced.

Figure 2.10 shows the transient response of i_L and v_C in the state plane when load resistance is decreased in a step fashion (R_{Load} from 2.5Ω to 1.25Ω, I_0 from 2A to 4A). Figure 2.10 shows that it takes 2~3 cycles for i_{LN} and v_{CN} to settle. Figure 2.11 shows the corresponding transient in R. The ripple in R is a magnified version of ripple in the output (scaled) voltage V_0. The magnification occurs through the proportional gain of the PI controller.

Figure 2.12 shows the transient of i_{LN} and v_{CN} in the state plane when load resistance is increased (R_{Load} from 1.25Ω to 2.5Ω, I_0 from 4A to 2A). Figure 2.12 shows that it takes 2~3 cycles for i_{LN} and v_{CN} to settle. Figure 2.13 shows the corresponding transient in R.

The transient of the output voltage is shown in Figure 2.14. From 0 to 3ms, the simulated SRC is started using a function generator operating at a fixed frequency of

Reproduced with permission of the copyright owner. Further reproduction prohibited without permission.

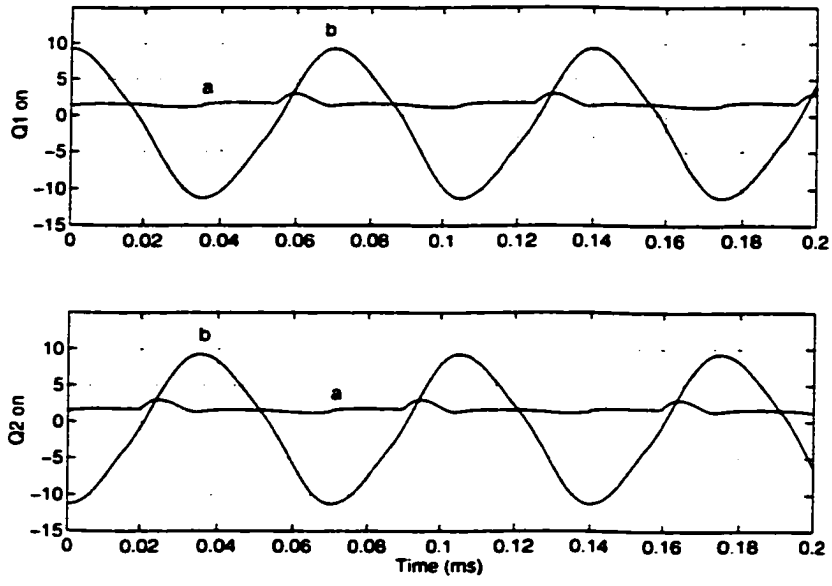

Figure 2.9: Simplified Control Law (Below-Simulation)

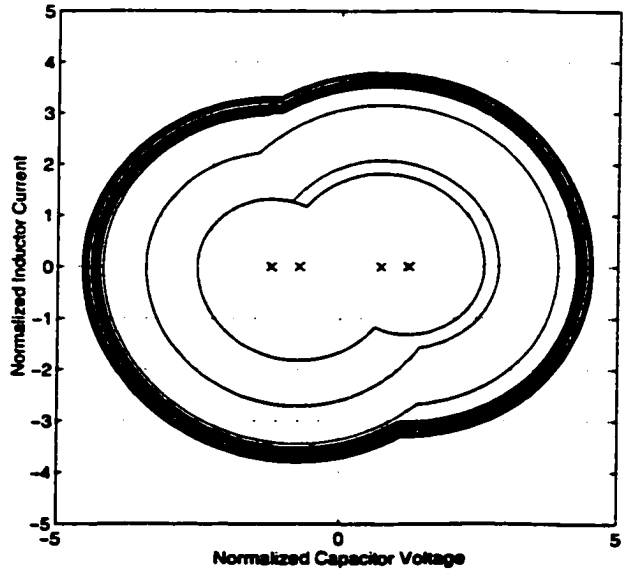

Figure 2.10: Transient of i_{LN} and v_{CN} (Below-Simulation-Increasing load)

Reproduced with permission of the copyright owner. Further reproduction prohibited without permission.

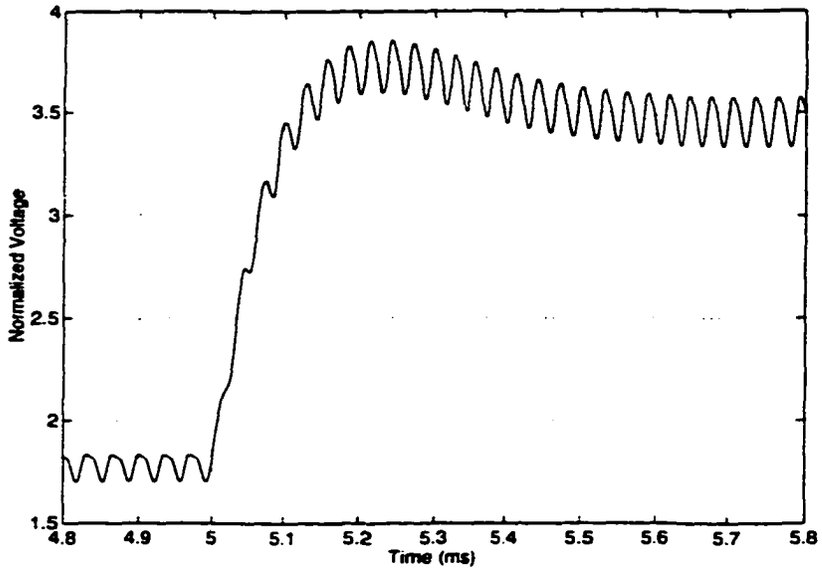

Figure 2.11: Transient of R (Below-Simulation-Increasing load)

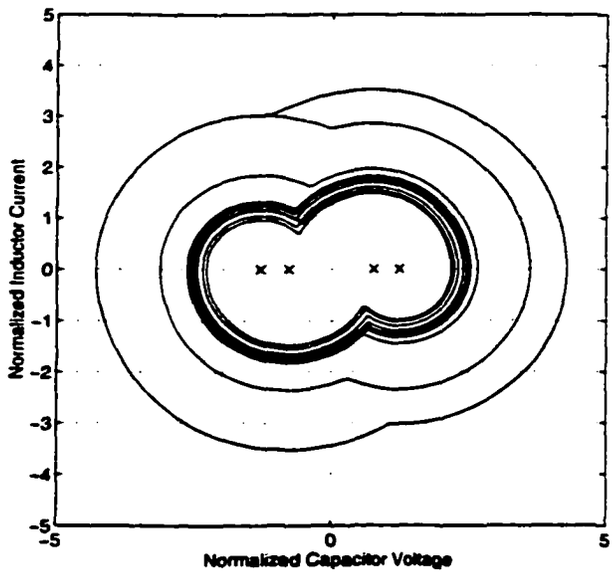

Figure 2.12: Transient of i_{LN} and v_{CN} (Below-Simulation-Decreasing load)

Reproduced with permission of the copyright owner. Further reproduction prohibited without permission.

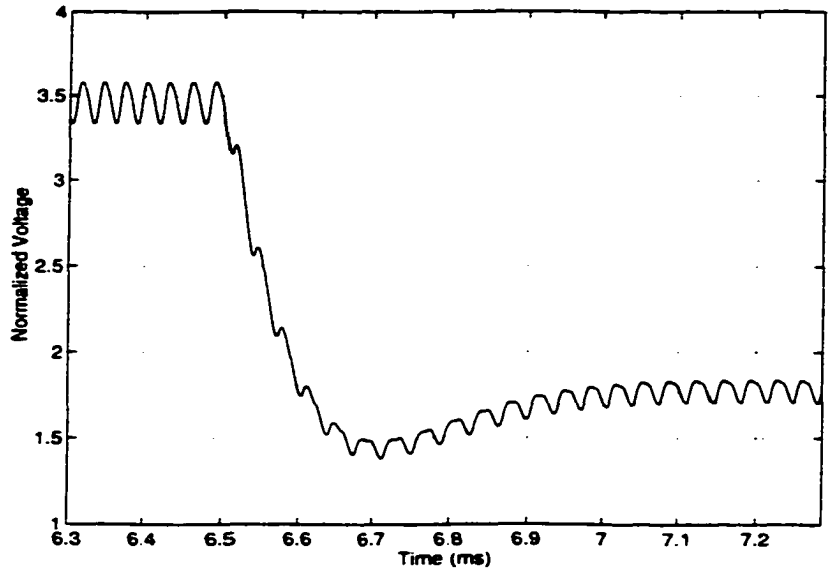

Figure 2.13: Transient of R (Below-Simulation-Decreasing load)

13.9kHz and with a load resistance on the SRC of 2.5Ω. Output voltage does not track the normalized setpoint V_{SN}=0.25. From 3ms onwards, modified capacitor voltage form of optimal trajectory control takes over from the function generator. The PI controller pushes V_0 to the setpoint with a little overshoot. From 5ms to 6.5ms, There is a step load change (I_0 from 2A to 4A). From 6.5ms to 8ms, there is another load change (I_0 from 4A to 2A). During the load changes, the system is stable and transient time to settle is about 0.5ms. This indicates that optimal trajectory control has very good performance in the face of a 50% load change.

Simulation of Above Resonant Frequency Operation

The parameters used in the simulations of above resonant frequency operation of the SRC are listed in Table 2.2.

Figure 2.15 shows the waveforms of the simplified control law of Equation (2.32) at steady state to determine the instants of turning Q1 and Q2 off. In this Figure, $a = R^2 - (|V_{C0N}| + V_{SN} - V_{0N})^2$ and $b = 4V_{SN}(\pm v_{CN} + V_{0N})$. According to the control law, if a≤b, Q1(Q2) will be turned off. By using this switching signal, the steady state results in the time domain and the state plane shown in Figures 2.4 and 2.6 were produced.

Figure 2.16 shows the transient of i_{LN} and v_{CN} in the state plane when load resistance is decreased in a step fashion (R_{Load} from 2.5Ω to 1.25Ω, I_0 from 2A to 4A). Figure 2.16 shows that it takes 4~5 cycles for i_{LN} and v_{CN} to settle. Figure 2.17 shows corresponding transient of total R.

Figure 2.18 shows the transient of i_{LN} and v_{CN} in the state plane when load resistance is increased in a step fashion (R_{Load} from 1.25Ω to 2.5Ω, I_0 from 4A to 2A). Figure 2.18 shows that it takes 4~5 cycles for i_{LN} and v_{CN} to settle. Figure 2.19 shows the

Reproduced with permission of the copyright owner. Further reproduction prohibited without permission.

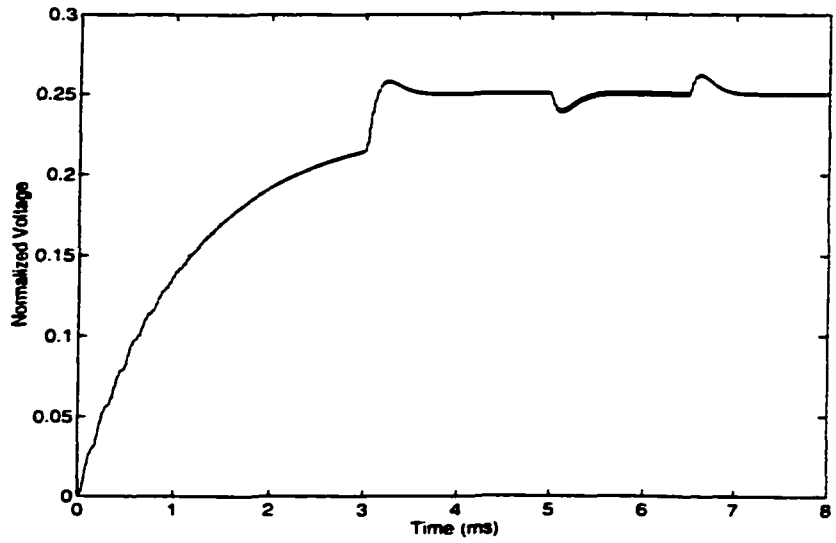

Figure 2.14: Transient of Output Voltage (Below-Simulation)

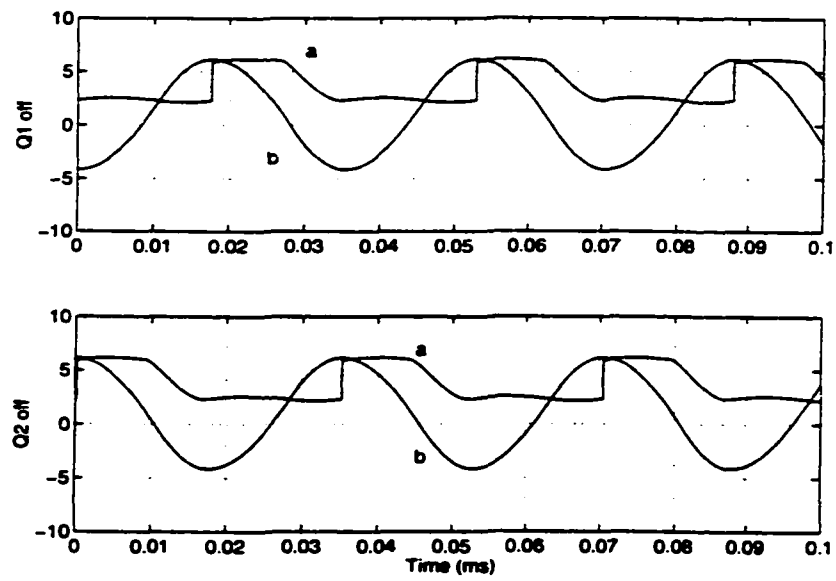

Figure 2.15: Simplified Control Law (Above-Simulation)

Reproduced with permission of the copyright owner. Further reproduction prohibited without permission.

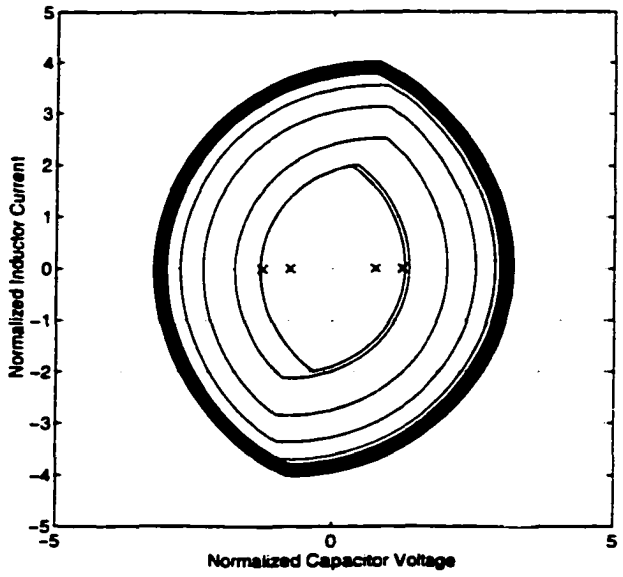

Figure 2.16: Transient of i_{LN} and v_{CN}(Above-Simulation-Increasing load)

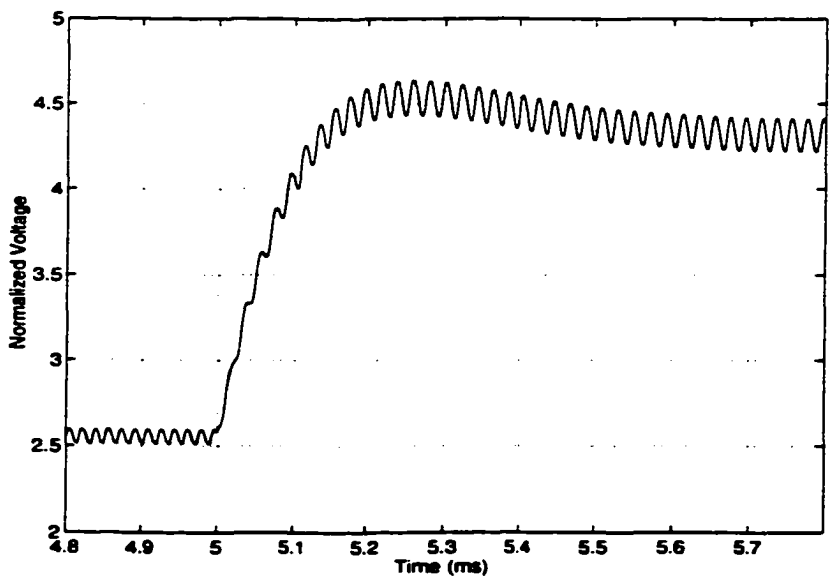

Figure 2.17: Transient of R(Above-Simulation-Increasing load)

Reproduced with permission of the copyright owner. Further reproduction prohibited without permission.

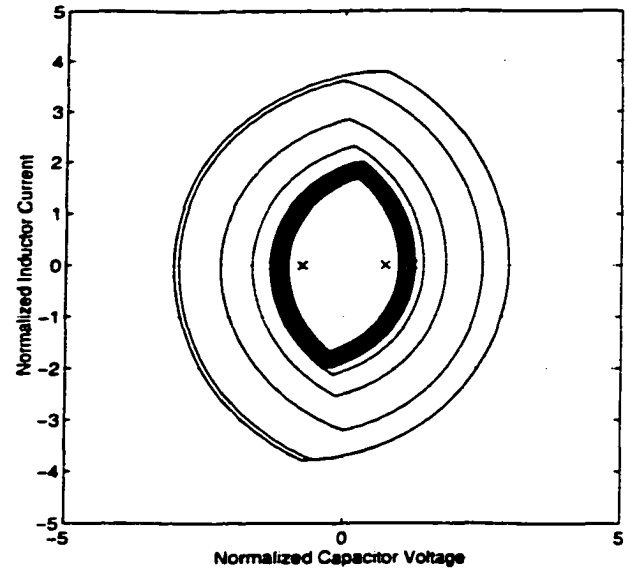

Figure 2.18: Transient of i_{LN} and v_{CN}(Above-Simulation-Decreasing load)

corresponding transient in total R.

The transient of the output voltage for above resonant frequency operation is shown in Figure 2.20. It is very similar to the below resonant frequency operation shown in Figure 2.14. From 0 to 3ms, the simulated SRC is started using a function generator operating at a fixed frequency of 27.8kHz and with a load resistance on the SRC of 2.5Ω. Output voltage does not track normalized setpoint V_{SN}=0.25. From 3ms onwards, modified capacitor voltage form of optimal trajectory control takes over the function generator. The PI controller pushes V_0 to the setpoint with some overshoot. From 5ms to 6.5ms, there is a step load change (I_0 from 2A to 4A). From 6.5ms to 8ms, there is another load change (I_0 from 4A to 2A). During the load changes, the system is stable and the time to settle is less than 0.5ms. This indicates that optimal trajectory control has very good performance in the face of a 50% load change.

Note that in the below resonant frequency operation, it takes 2~3 cycles for i_{LN} and v_{CN} to settle, but in the above resonant frequency operation, it takes 4~5 cycles. This is because the switching frequency is different. The time elapsed during the transients, 2~3 cycles in the below resonant frequency operation is approximately the same time as 4~5 cycles in the above resonant frequency operation.

From state plane portraits and the traces of total R, it is evident that i_{LN} and v_{CN} assume their optimal trajectory as determined by R very quickly. However, the number of cycles taken by the response of V_{0N} to reach steady state is dominated significantly by the time constant of the filter capacitor and load resistor. Moreover, the output voltage is a capacitor filtered waveform. It always has ripples because of capacitor charging and discharging. These ripples are magnified by the high P gains listed in Table 2.2. This results in the ripples of corresponding R as shown for example in Figures 2.17 and 2.19. Consequently, in Figures 2.10 and 2.12, 2.16 and 2.18, the trajectories have bands after

Reproduced with permission of the copyright owner. Further reproduction prohibited without permission.

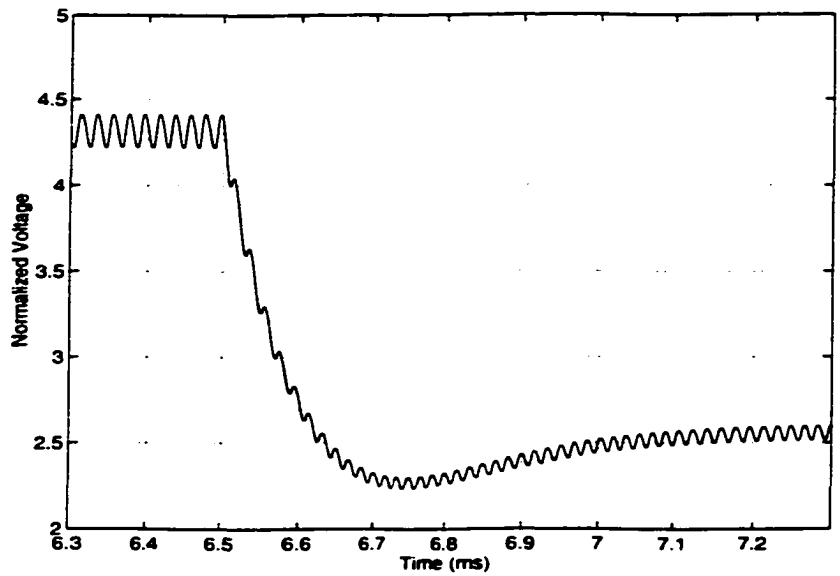

Figure 2.19: Transient of R(Above-Simulation-Decreasing Load)

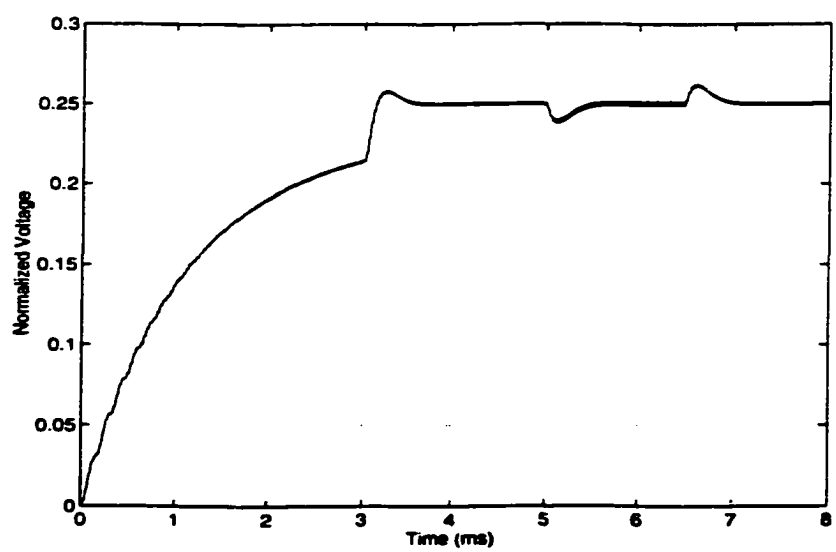

Figure 2.20: Transient of Output Voltage (Above-Simulation)

Reproduced with permission of the copyright owner. Further reproduction prohibited without permission.

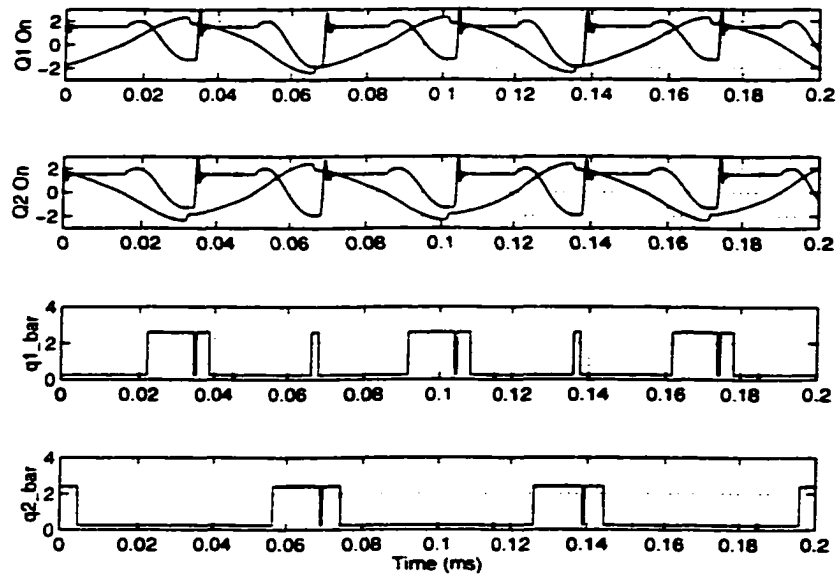

Figure 2.21: Waveforms of simplified control law(Below-Lab)

settling down. This effect is nominal in the steady state.

2.5.2 Implementation

The variable frequency SRC operation model has been implemented in an experimental prototype based on the logic diagram discussed in Appendix A.3.

Implementation of below resonant frequency operation

The control law for below resonant frequency operation is given in Equation (2.28). Let V_{L0}=$V_S + V_0 - |V_{C0}|$, the control law can be written for implementation as:

$$4V_S(\pm v_C - V_0) \leq R^2 - V_{L0}{}^2 = (R - V_{L0})(R + V_{L0}) \tag{2.34}$$

The block diagram of the implementation of Equation (2.34) is shown in Figure A.3. The waveforms obtained experimentally for the left hand side and right hand side of Equation (2.34) and the results of the comparison operation of Equation (2.34) are shown in Figure 2.21. The signals of the sign of the inductor current and final switching signals to turn on the Mosfets for this experimental run are shown in Figure 2.22.

Implementation of above resonant frequency operation

The control law for above resonant frequency operation is given in Equation (2.32). Let V_{L0}=$|V_{C0}| + V_S - V_0$, the control law can be written for implementation as:

$$4V_S(\pm v_C + V_0) \geq R^2 - V_{L0}{}^2 = (R - V_{L0})(R + V_{L0}) \tag{2.35}$$

Reproduced with permission of the copyright owner. Further reproduction prohibited without permission.

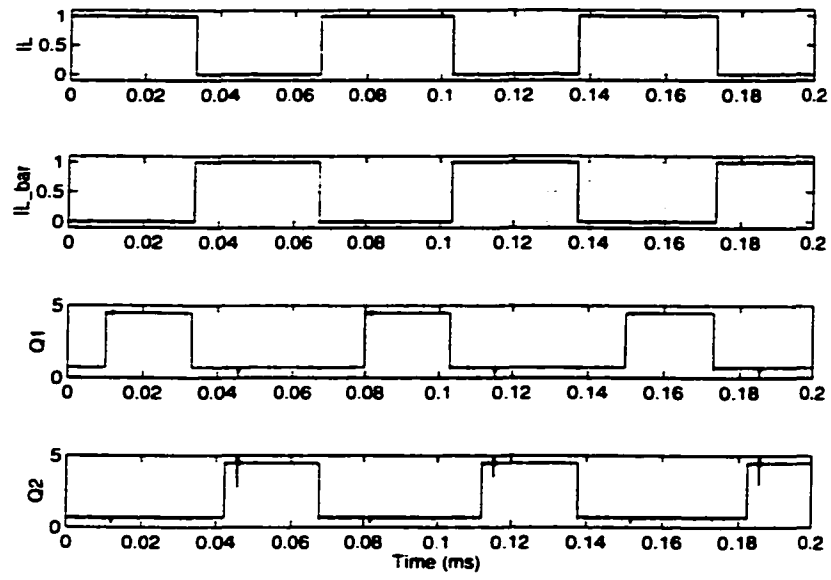

Figure 2.22: Switching Signals (Below-Lab)

The block diagram of this implementation is shown in Figure A.4. The waveforms obtained experimentally for the left hand side and right hand side of Equation (2.35) and the results of the comparison operation of Equation (2.35) are shown in Figure 2.23. The signals of the sign of the inductor current and final switching signals to turn off the Mosfets for this experimental run are shown in Figure 2.24.

2.5.3 Experimental Results

The proposed implementation of the loops of the modified capacitor voltage form of the optimal trajectory control law was tested on an experimental SRC with nominal parameters listed in Table 2.3. The parameters of the experimental SRC are the same as in Table 2.2 used for simulation except for the P and I gains and base value of R. These differences will be discussed in Section 2.6.

V_S	20V (1)	V_0	5V (0.25)
L	$88.6\mu H$	C	$0.68\mu F$
C_L (Below)	$470\mu F$	C_L (Above)	$470\mu F$
Z_0	11.46Ω (1)	f_0 (Resonant)	20.5kHz
R_{Load} (Low Current)	2.5Ω (0.22)	R_{Load} (High Current)	1.25Ω (0.11)
f_S (Below) Steady State $R_{Load} = 2.5\Omega$	14kHz	f_S (Above) Steady State $R_{Load} = 2.5\Omega$	28kHz
f_S Range (Below)	14.0~17.481KHz	f_S Range (Above)	24.447~28.0KHz
P gain (Below)	70	I gain (Below)	532000
P gain (Above)	60	I gain (Above)	368000
R_{base} (Below)	60V (3)	R_{base} (Above)	22V (1.1)

Table 2.3: Implementation Circuit Parameters for VF-SRC

Reproduced with permission of the copyright owner. Further reproduction prohibited without permission.

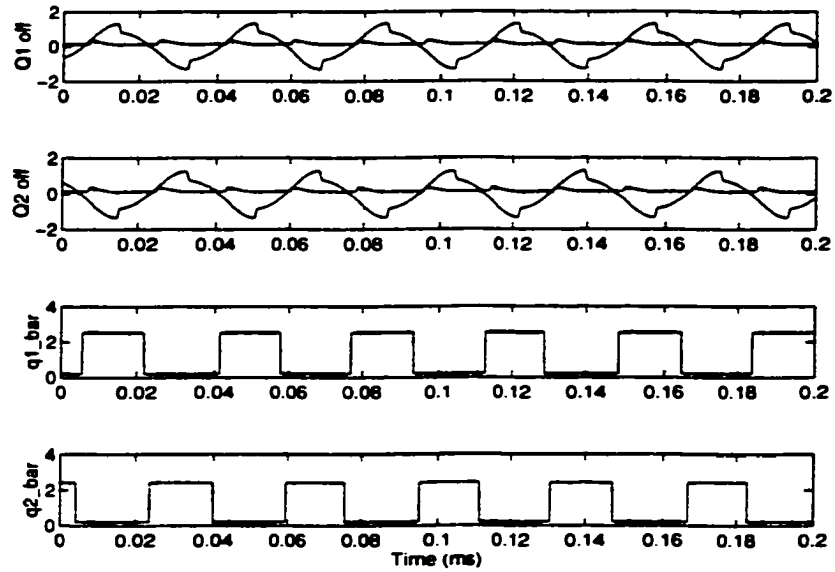

Figure 2.23: Waveforms of simplified control law(Above-Lab)

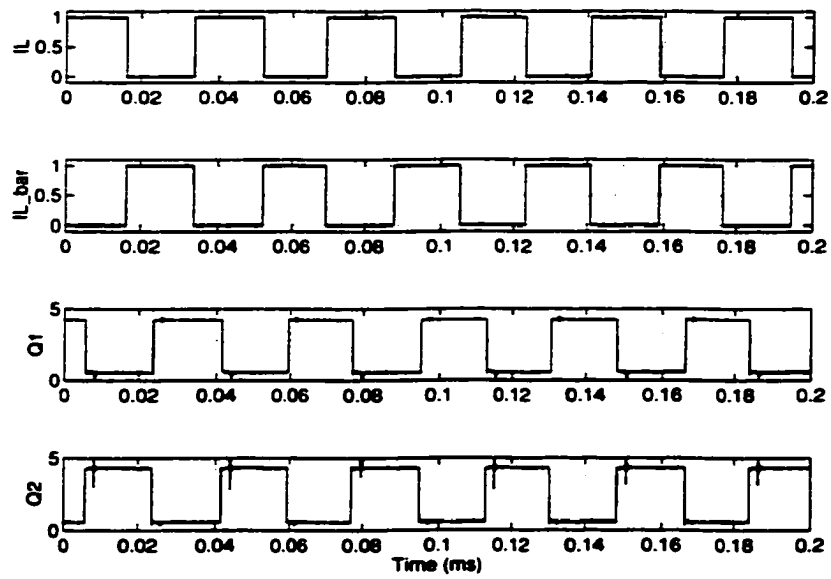

Figure 2.24: Switching Signals (Above-Lab)

Reproduced with permission of the copyright owner. Further reproduction prohibited without permission.

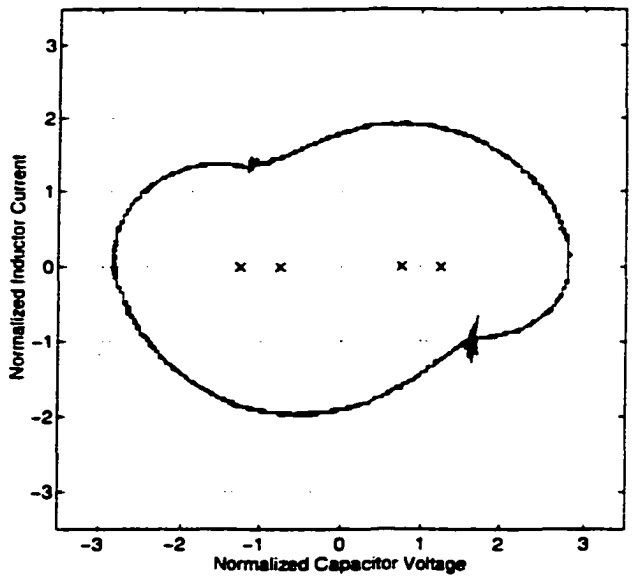

Figure 2.25: Steady State of i_{LN} and v_{CN} (Below-Lab)

Results of Below Resonant Frequency Operation

Figure 2.25 shows the steady state waveforms of i_L and v_C measured on the experimental VF-SRC in the state plane when the circuit is operating at its nominal parameters.

The performance of modified capacitor voltage control law based optimal trajectory control Equation (2.28) and implemented by Equation (2.34) is tested by a 50% step change in load. viz for an output current change from 2A to 4A or from 4A to 2A.

The transient response of i_{LN} and v_{CN} are shown in Figure 2.26 in the state plane for a step increase in the load. It takes about 3 cycles from the steady state at low load to reach the steady state at high load. This matches the results obtained from simulation. Figure 2.27 shows the corresponding transient response of total R.

Figure 2.28 shows the waveforms of output voltage and error between the reference (set point) voltage for the output and the actual output voltage during the transient. From this plot, it is seen that the variation of output voltage during the load change is less than 4% and the settling time is about 0.8ms.

Figures 2.29 through 2.31 show the results for a step decrease in the load. From these figures, it is seen that it takes about 2~3 cycles for i_{LN} and v_{CN} to settle after the step. This matches the results obtained from simulations earlier. The settling time of the output voltage after the step decrease in load is about 0.4ms which is shorter than the settling time when the load is increased. However, the variation of output voltage during the transient is about 10% which is higher than that obtained when the load is increased. The transient responses of Figure 2.29 through 2.31 for a step decrease in load are not the exact inverse waveforms of those in Figure 2.26 through 2.28 for a step increase in load because the dynamics of the experimental SRC with its control loops are nonlinear for such large (50%) load change.

Reproduced with permission of the copyright owner. Further reproduction prohibited without permission.

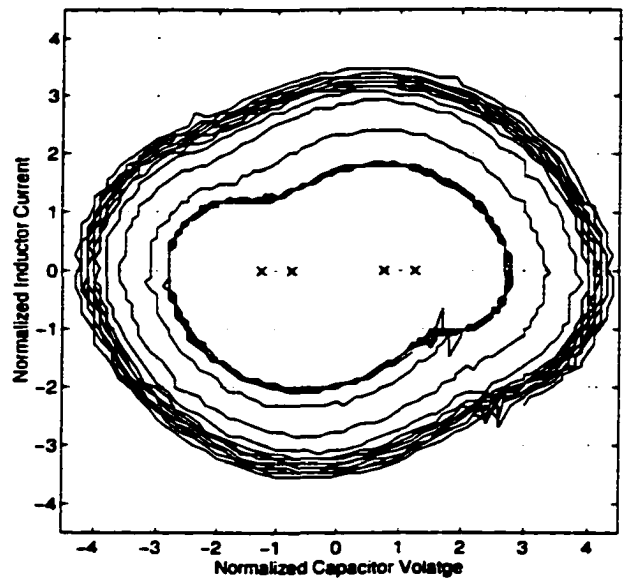

Figure 2.26: Transient of i_{LN} and v_{CN} (Below-Lab-Increasing Load)

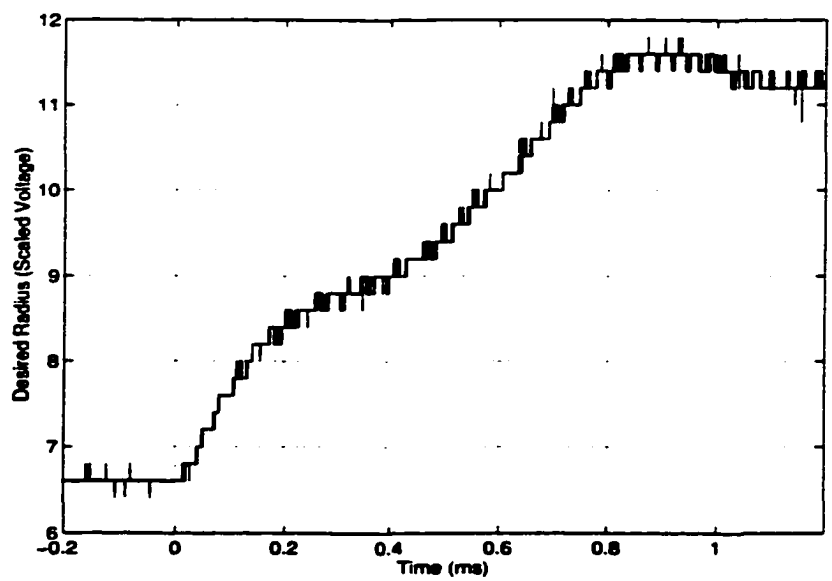

Figure 2.27: Transient of R(Below-Lab-Increasing Load)

Reproduced with permission of the copyright owner. Further reproduction prohibited without permission.

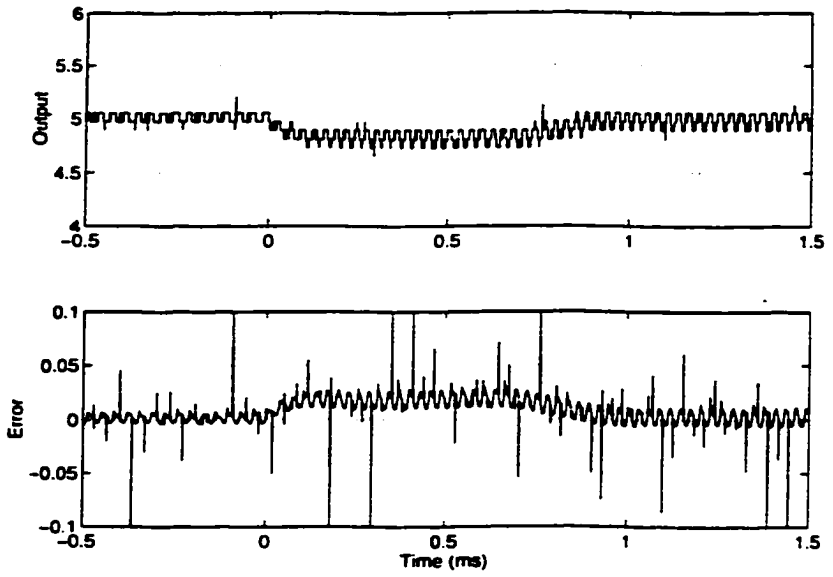

Figure 2.28: Transient of Output Voltage and Error (Below-Lab-Increasing Load)

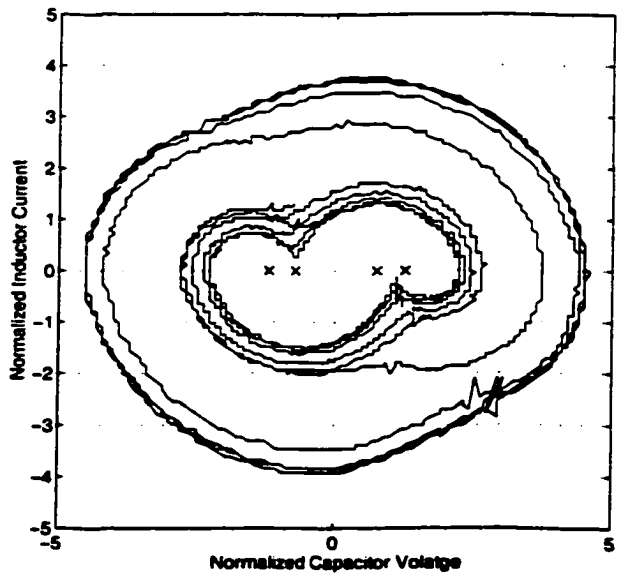

Figure 2.29: Transient of i_{LN} and v_{CN} (Below-Lab-Decreasing Load)

Reproduced with permission of the copyright owner. Further reproduction prohibited without permission.

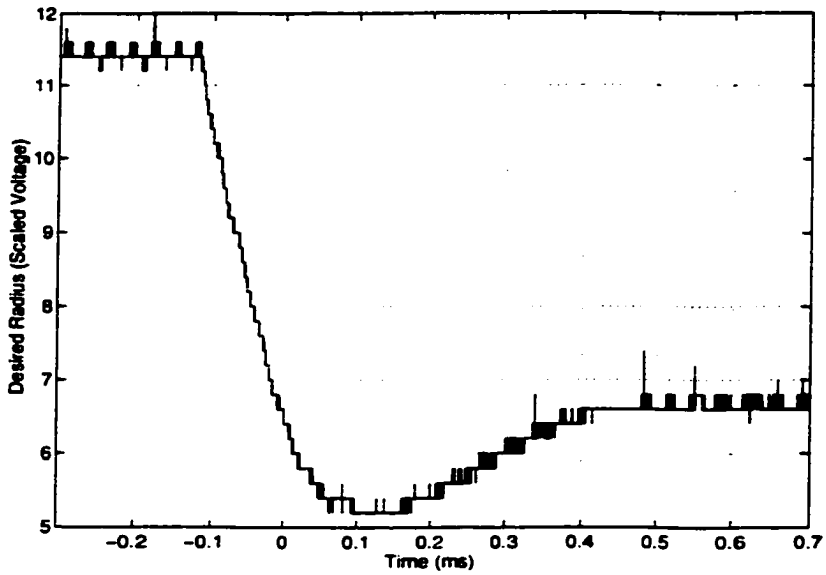

Figure 2.30: Transient of R(Below-Lab-Decreasing Load)

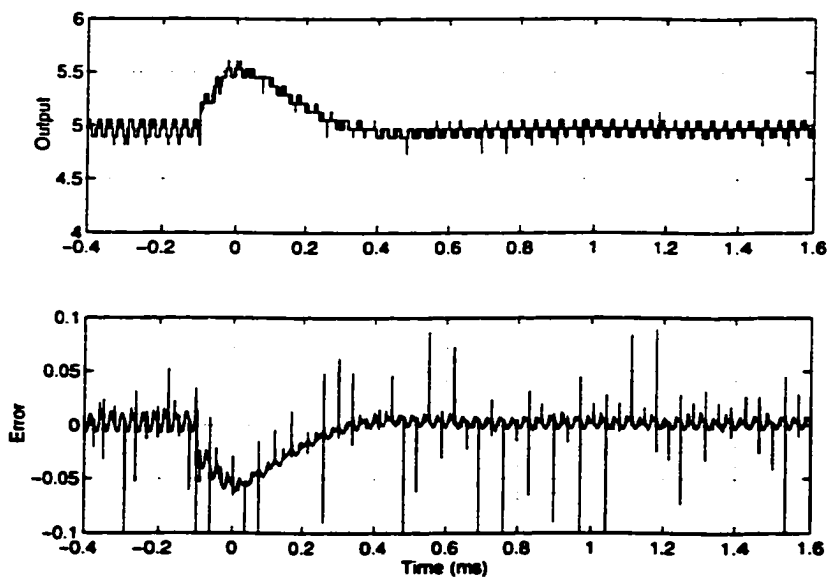

Figure 2.31: Transient of Output Voltage and Error (Below-Lab-Decreasing Load)

Reproduced with permission of the copyright owner. Further reproduction prohibited without permission.

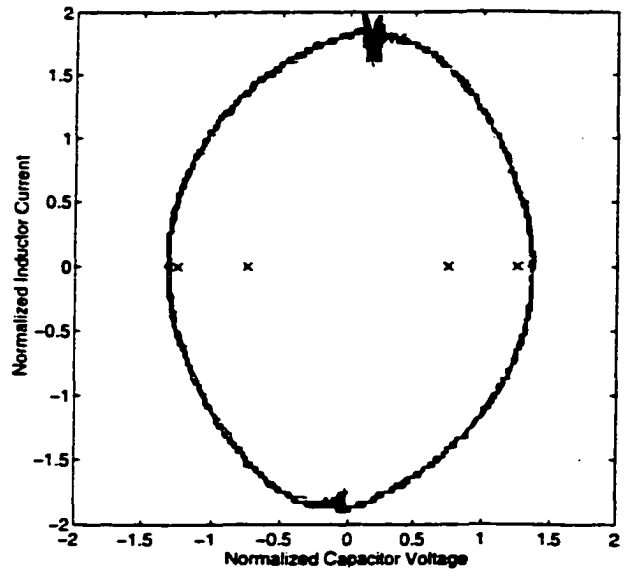

Figure 2.32: Steady State of i_{LN} and v_{CN} (Above-Lab)

Results of Above Resonant Frequency Operation

Figure 2.32 shows the steady state waveforms of i_{LN} and v_{CN} measured on the experimental VF-SRC in state plane when the circuit is operating at its nominal parameters.

The performance of modified capacitor voltage control law based optimal trajectory control Equation (2.32) and implemented through Equation (2.35) is tested by a 50% step change in load (2A to 4A and vice versa in output current of the VF-SRC).

The transient response of i_{LN} and v_{CN} is shown in the state plane in Figure 2.33 for a step increase in load. It takes about 6 cycles from the steady state at low load to reach the steady state at high load. This matches the results obtained earlier from simulations. Figure 2.34 shows the corresponding transient response of total R.

Figure 2.35 shows the waveforms of output voltage and error between set point and the actual output voltage during this transient. From this plot, the variation of the output voltage during this load change is less than 4% and the settling time is about 0.8ms.

Figures 2.36 through 2.38 show the results for a step decrease in the load. From these plots, it is seen that it takes about 6 cycles for i_{LN} and v_{CN} to settle after the step. The settling time of the output voltage after the step decrease in load is about 0.6ms. However, the variation of the output voltage during the transient is about 8% which is higher than the variation of output voltage when the load is increased. Just like the below resonant frequency case, the transient responses when the load is decreased are not the exact inverse waveforms of those obtained when the load is increased as the dynamics of the experimental SRC are nonlinear for such large (50%) load changes.

Reproduced with permission of the copyright owner. Further reproduction prohibited without permission.

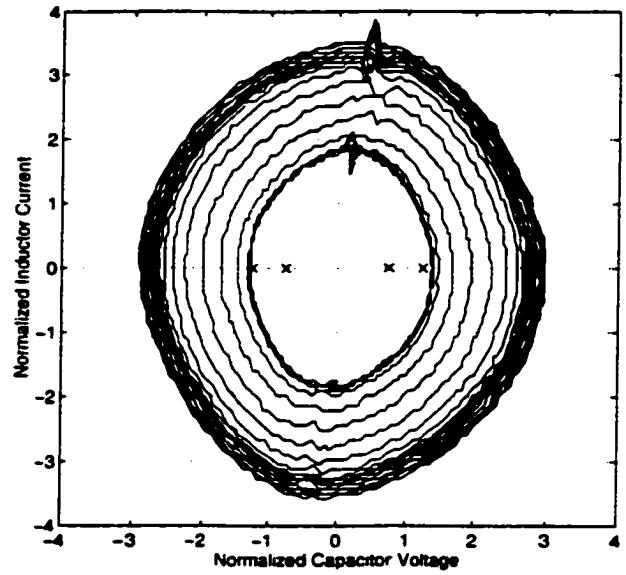

Figure 2.33: Transient of i_{LN} and v_{CN} (Above-Lab-Increasing Load)

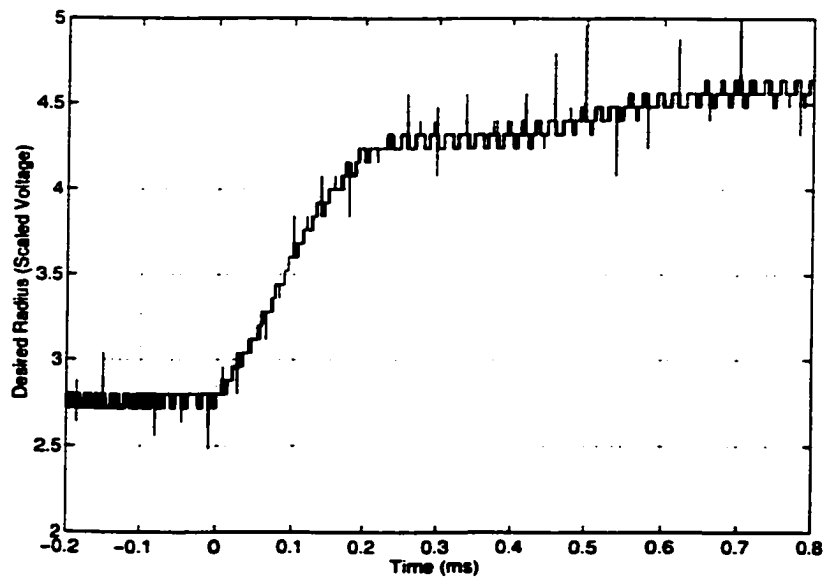

Figure 2.34: Transient of R (Above-Lab-Increasing Load)

Reproduced with permission of the copyright owner. Further reproduction prohibited without permission.

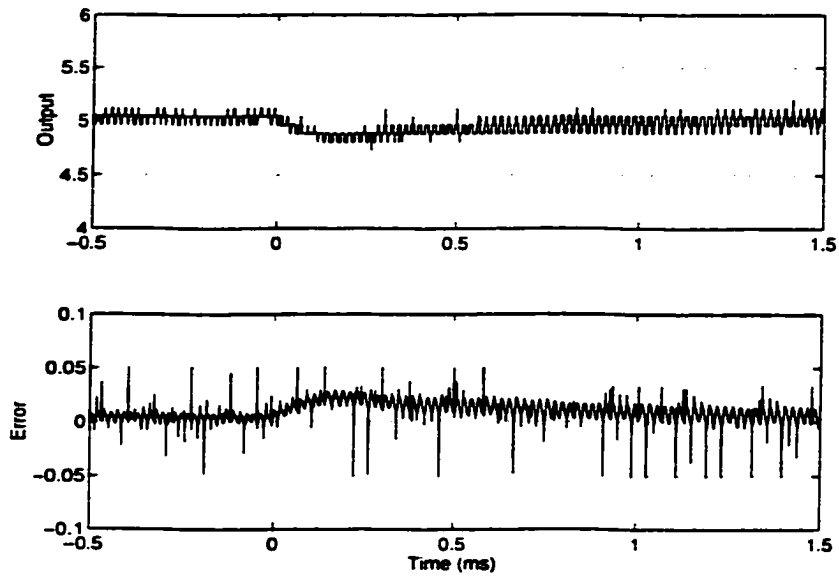

Figure 2.35: Transient of Output Voltage and Error (Above-Lab-Increasing Load)

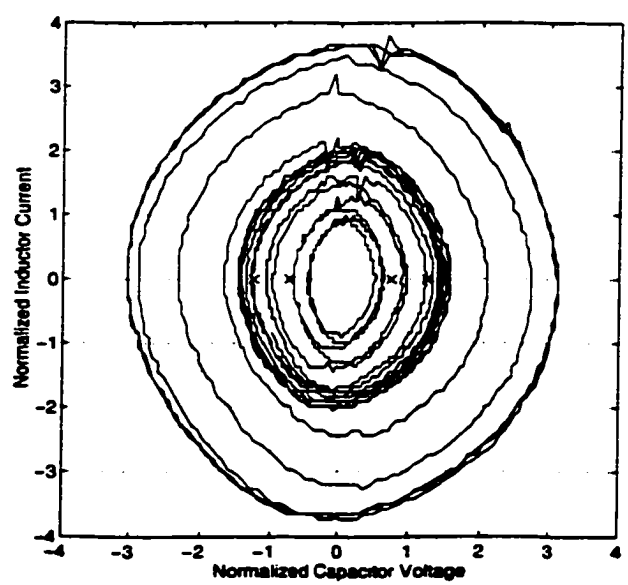

Figure 2.36: Transient of i_{LN} and v_{CN} (Above-Lab-Decreasing Load)

Reproduced with permission of the copyright owner. Further reproduction prohibited without permission.

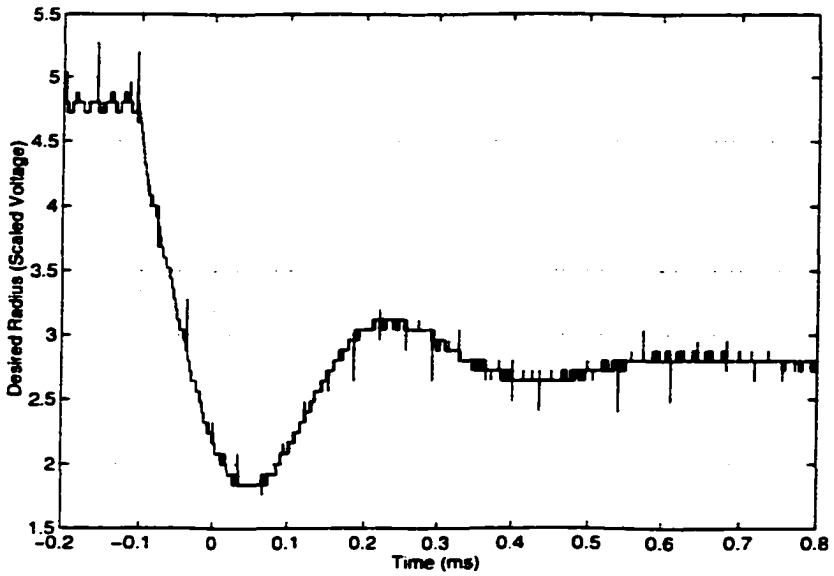

Figure 2.37: Transient of R (Above-Lab-Decreasing Load)

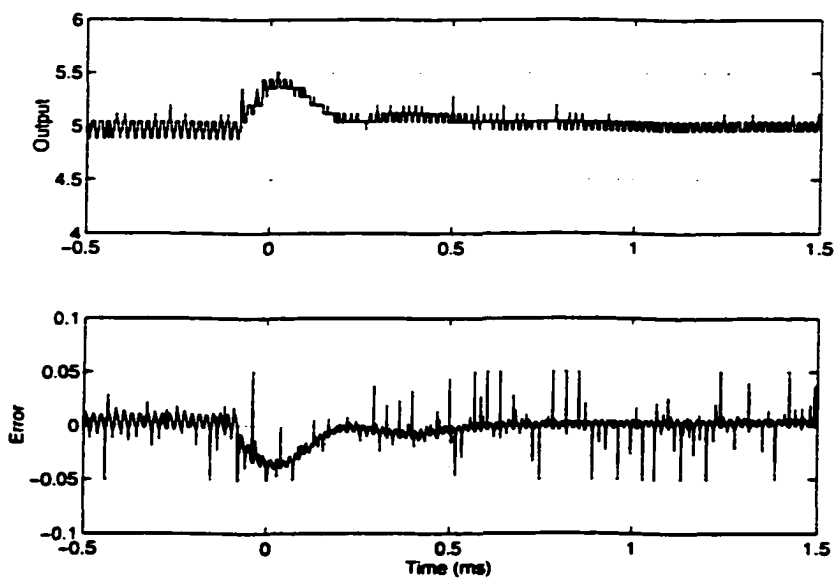

Figure 2.38: Transient of Output Voltage and Error (Above-Lab-Decresing Load)

Reproduced with permission of the copyright owner. Further reproduction prohibited without permission.

2.6 Conclusion

In the simulations and experiments. V_S, V_0, L. C, C_L and R_{Load} have the same nominal values. However. R_{base}, P gain and I gain listed in Table 2.2 and 2.3 are different. This is because the practical circuit has some differences from the simulated circuits. Firstly. assumptions have been adopted in the simulations, such as ideal switches, negligible tank circuit resistance. no parameter variations, etc. Thus the simulations were conducted for an ideal situation. The losses in the practical circuit also cause the variation of the parameters and slight deviations of trajectories from the arcs of circles in the theoretical derivations. Secondly, in the simulations no additional filtering except that produced by C_L was provided on the error fed to the high PI gain controller for producing R (Note the ripples in the simulations in Figures 2.11. 2.13, 2.17 and 2.19). In the experimental control circuit, filtering was introduced in the control effort (R) from the PI controller to reduce the ripples. Additional filtering was necessary to prevent spurious switching. The filter cut off frequency was selected at 4kHz. Consequently, the filter introduces phase shift. Some phase shift is also introduced by the analog processing in the multipliers. etc. So while the simulations provide ideas of the possible PI gains to be used for control. the implementation gains were tuned to provide a compromise among settling time. transient response and noise for the 50% load change. R_{base} was adjusted to provide adequate range for the load change involved in the experimental setup.

In this thesis. the control strategy is decoupled into multirate structure. The outer loop regulates output voltage. Most studies of optimal trajectory control [9. 12] neither consider the external PI loop design. nor avoid high bandwidth current measurements. If the outer loop to select R is designed correctly, optimal trajectory control guarantees that tank circuit quickly reaches steady state. Simulation studies provide a valuable tool in design of this loop. Based on the multirate control structure, the expermental results are very close to the simulation results. It indicates that losses in the circuit do not significantly affect the predictive ability of calculations and simulations done with the ideal models.

The advantage offered by using the direct optimal trajectory control technique [8. 9] in term of dynamic performance is somewhat obscured by its apparent implementation complexity and the limitations imposed by its poor robustness to circuit parameter changes. In this Chapter, the optimal trajectory control law is simplified as in [5] so that the implementation complexity is reduced and high bandwidth inductor current measurement and scaling using the characteristic impedance are avoided. This has conferred the optimal trajectory control with robustness to circuit parameter changes. These become more evident in the results of Chapter 3.

Reproduced with permission of the copyright owner. Further reproduction prohibited without permission.

Chapter 3

Optimal Trajectory Control of CF-SRC

3.1 Introduction

Series resonant converter (SRC) allows high frequency operation with zero-current switching and hence facilitates size and weight reduction with improved efficiency, reduced EMI and reduced stresses on switches. However, in the variable frequency SRC studied in Chapter 2, a wide range of switching frequency is required and as a result, a large EMI spectrum is produced. EMI emitted with variable frequency is more difficult to control than fixed frequency EMI. Constant frequency resonant converters can overcome this disadvantage of variable frequency resonant converters [6, 10, 13, 15]. However, their control requirements and operating characteristics have an added complexity due to the fixed frequency of switching which limits their performance [10, 13].

State plane analysis techniques have been successfully employed in characterizing steady state and dynamic behaviour of resonant converters [7, 8, 10]. Based on state plane analysis, optimal trajectory control was first proposed for variable frequency SRC which forces the resonant state variables to track their trajectory in minimum time from one steady state to another [7, 8]. A modified version of OTC [5] has been verified in Chapter 2 of this thesis. While the OTC approach facilitates superior transient performance, it is complex to implement and susceptible to parameter variation [9]. However, as shown in Chapter 2, the inherently nonlinear control law can be simplified into a pseudo-linear form which greatly reduces its implementation complexity and improves its robustness to parameter variation [5].

In this Chapter, an analysis of a constant frequency series resonant converter (CF-SRC) in the state plane is presented and following [6], optimal trajectory control is extended to constant frequency SRC. In analyzing the CF-SRC, one has to take into account the additional constraint due to fixed frequency switching. Based on this analysis, a suitable parameter for trajectory control is identified which provides a framework for the design of an optimal switching control scheme to achieve the lowest possible response time with guaranteed stability using this scheme. The proposed optimal trajectory control law

Reproduced with permission of the copyright owner. Further reproduction prohibited without permission.

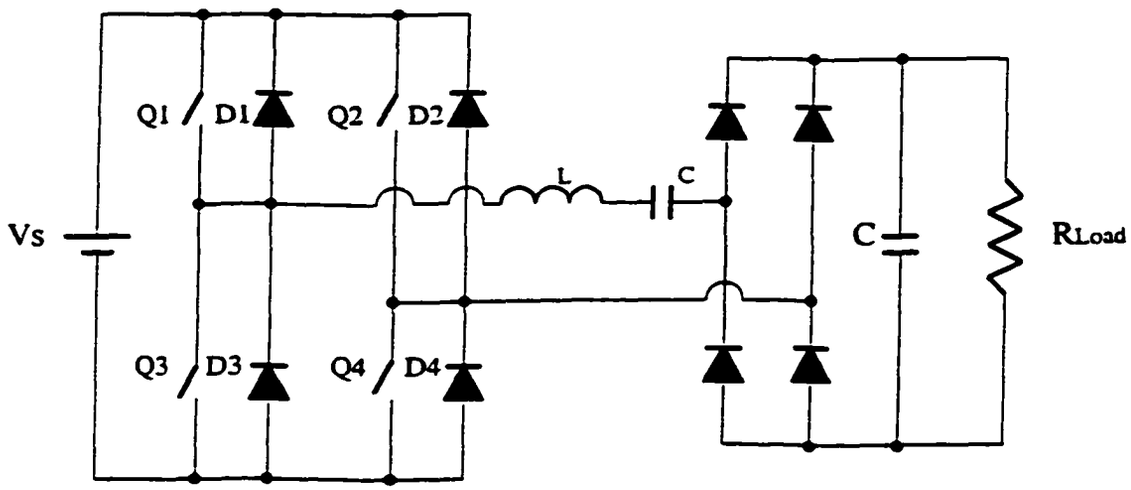

Figure 3.1: Constant Frequency SRC Circuit

[6] has a nonlinear form as in the case of variable frequency SRC. Following the earlier work [6], this control law for the CF-SRC is simplified into a pseudo-linear form which is robust to parameter variations. This simplified control law is shown to have decoupled dynamics and can be implemented in a multirate frame work. In [6], no experimental results were reported. This Chapter is devoted to verifying the theoretical results in [6] by experimental work. Results of CF-SRC operation under the robust optimal trajectory control with reduced implementation complexity [6] are presented.

3.2 State-Plane Analysis of CF-SRC

As introduced in Section 2.2.1, series resonant converters are normally analyzed by identifying the circuit modes of converters during a switching cycle and solving the associated differential equations of the state variables with the appropriate boundary conditions associated with transitions between those modes. In this Section, the topological modes of CF-SRC are identified and the CF-SRC is analyzed in the state plane.

The circuit configuration of the CF-SRC is given in Figure 3.1. The switching strategy for the fixed frequency operation of this circuit is that switches Q1 and Q3 are turned on and off by a constant frequency (f_S) gating signal with a 50% duty cycle. Switches Q2 and Q4 are turned on and off by a gating signal, which in the steady state, has the same frequency and duty cycle as that controlling Q1 and Q3, but is phase shifted with Q2 and Q4 being switched on before Q3 and Q1, respectively. The switching frequency f_S is assumed to be greater than the resonant frequency of the tank circuit since the higher the switching frequency, the greater the power density of the circuit due to smaller components.

Reproduced with permission of the copyright owner. Further reproduction prohibited without permission.

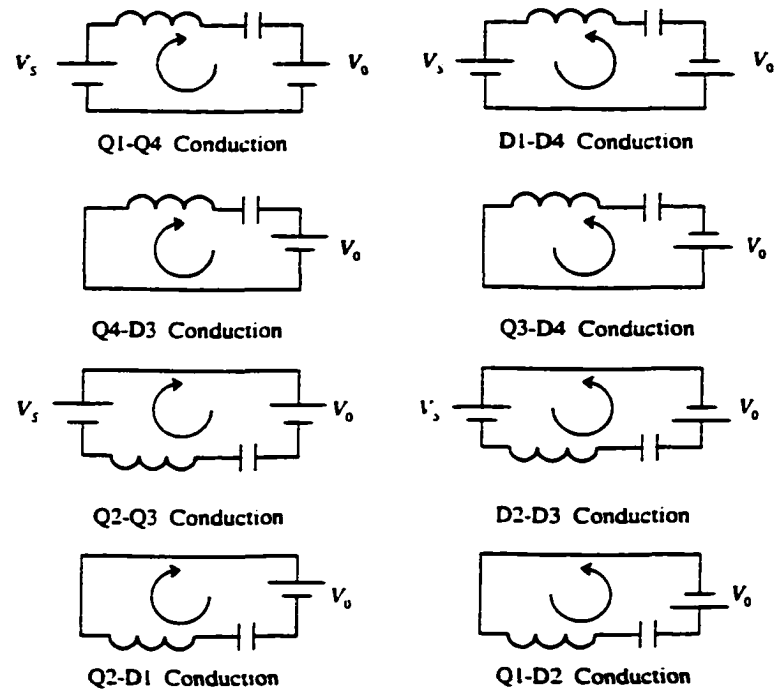

Figure 3.2: Topological Modes of Constant Frequency SRC

Mode	V_E	Mode	V_E
Q1-Q4	$V_S - V_0$	Q1-D2	$-V_0$
D2-D3	$-V_S - V_0$	Q4-D3	$-V_0$
Q2-Q3	$-V_S + V_0$	Q3-D4	V_0
D1-D4	$V_S + V_0$	Q2-D1	V_0

Table 3.1: Equivalent Circuit DC Voltage of CF-SRC

3.2.1 Circuit Topological Modes

Unlike the VF-SRC circuit, there are four switches (MOSFETs) in the CF-SRC circuit. Therefore, eight topological modes are available. They are shown in Figure 3.2.

The governing differential equation for these topological modes using current in the inductor (i_L) and voltage across the capacitor (v_C) of the tank circuit as state variables is given by:

$$\begin{bmatrix} \dot{v_C} \\ \dot{i_L} \end{bmatrix} = \begin{bmatrix} 0 & -\frac{1}{L} \\ \frac{1}{C} & 0 \end{bmatrix} \begin{bmatrix} i_L \\ v_C \end{bmatrix} + \begin{bmatrix} \frac{1}{L} \\ 0 \end{bmatrix} V_E \tag{3.1}$$

In Equation (3.1), V_E is the voltage across the tank circuit in each mode. The values of V_E in each mode is given in Table 3.1.

The solution of Equation (3.1) in the time domain in each mode is given by:

$$Z_0 i_L = (V_E - V_{C0}) sin(\omega_0 t) + I_{L0} cos(\omega_0 t) \tag{3.2}$$

$$v_C = Z_0 I_{L0} sin(\omega_0 t) - (V_E - V_{C0}) cos(\omega_0 t) + V_E \tag{3.3}$$

Reproduced with permission of the copyright owner. Further reproduction prohibited without permission.

In Equations (3.2) and (3.3) V_{C0} and I_{L0} are the boundary conditions of the state variables at the time of entry into each mode. ω_0, Z_0 in Equations (3.2) and (3.3) are the resonant frequency and the characteristic impedance of the tank circuit respectively.

Using the same normalization technique as in Chapter 2, all voltages are normalized by dividing by V_S, all currents are normalized by multiplying by Z_0 and then dividing by V_S. Finally using $\theta_0=\omega_0 t$, the following normalized form of the solution in Equation (3.1) is obtained:

$$i_{LN} = (V_{EN} - V_{C0N})sin(\theta_0) + I_{L0N}cos(\theta_0) \tag{3.4}$$

$$v_{CN} - V_{EN} = I_{L0N}sin(\theta_0) - (V_{EN} - V_{C0N})cos(\theta_0) \tag{3.5}$$

where V_{C0N} and I_{L0N} are the scaled initial capacitor voltage and scaled current through the inductor at entry into each mode. Following the analysis of variable frequency SRC in Chapter 2, from Equation (3.4) and (3.5), the following Equation is derived:

$$(v_{CN} - V_{EN})^2 + {i_{LN}}^2 = (V_{C0N} - V_{EN})^2 + {I_{L0N}}^2 \tag{3.6}$$

From Equation (3.6), we recognize that, in the state plane with axes v_{CN} and i_{LN}, each mode of the circuit has the trajectory of an arc of a circle with appropriate radii determined by the initial capacitor voltage V_{C0N} and initial inductor current I_{L0N} and centers at one of $(V_{0N}, 0)$, $(V_{SN} + V_{0N}, 0)$, $(V_{SN} - V_{0N}, 0)$ or the mirror images of these centers about the i_{LN} axis.

3.2.2 Control Parameterization of the CF-SRC

Based on the assumptions made above and the circuit topological modes, the two steady state switching portraits of the CF-SRC operating above resonance are shown in Figure 3.3 and 3.4. In Figure 3.3, the transition from Q1-D2 mode to D2-D3 mode and from Q3-D4 mode to D1-D4 mode is activated by the constant frequency switching of Q1 and Q3. In Figure 3.4, the transition from Q4-D3 mode to Q1-Q4 mode and from Q2-D1 mode to Q3-Q2 mode is achieved by the constant frequency switching of Q1 and Q3. In both Figures, the transition from Q1-Q4 mode to Q1-D2 mode and from Q2-Q3 mode to Q3-D4 mode is initiated by the instant of switching of Q2 and Q4 which provides the mechanism for control of the state plane portraits.

The mode transitions initiated by the switching of Q2(Q4) can be characterized by the radius R (Figures 3.3 and 3.4) of the portion of the trajectory in Q1-D2 mode (Q3-D4 mode) from the centre $(-V_{0N}, 0)$(or $(V_{0N}, 0)$).

From Figures 3.3 and 3.4, the load current which is the rectified average inductor current over a switching cycle can be expressed as:

$$\bar{i}_{LN} = \frac{2\omega_S \mid V_{C0N} \mid}{\omega_0 \pi} \tag{3.7}$$

where V_{C0N} is the capacitor voltage at the zero crossing of the inductor current and $\omega_S=2\pi f_S$ is the angular switching frequency of the CF-SRC. From Figure 3.4, the radius R is related to the capacitor voltage by:

Reproduced with permission of the copyright owner. Further reproduction prohibited without permission.

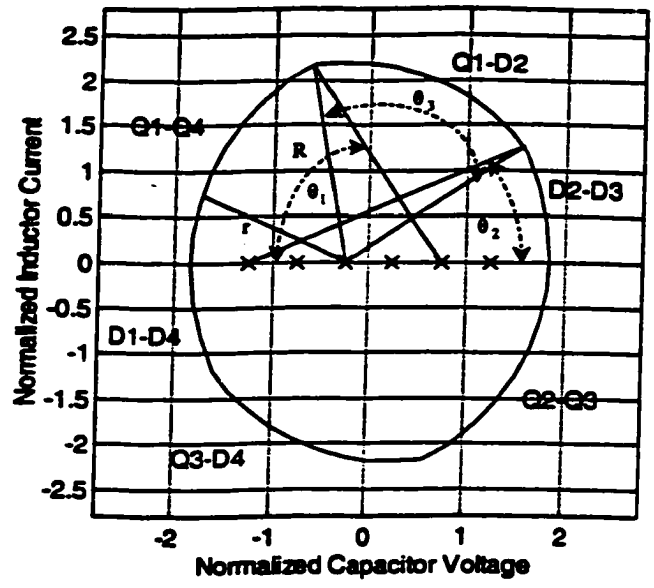

Figure 3.3: State Plane Trajectory in Nonlinear Operation

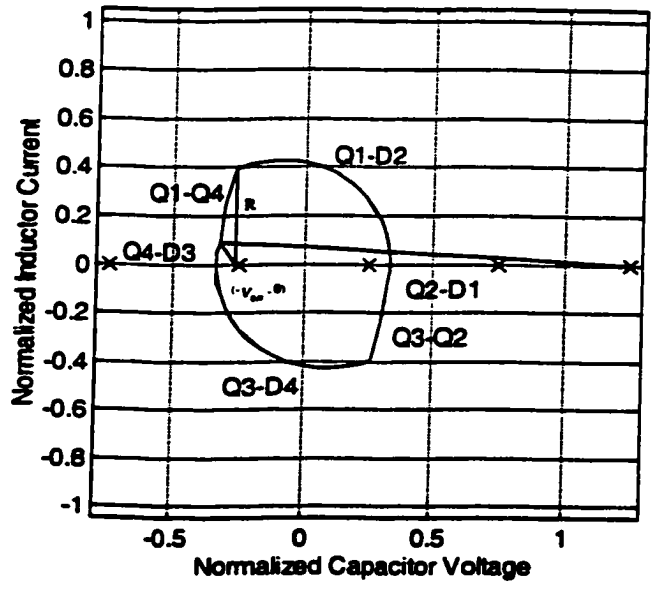

Figure 3.4: State Plane Trajectory in Linear Operation

Reproduced with permission of the copyright owner. Further reproduction prohibited without permission.

$$R = | V_{C0N} | + V_{0N} \tag{3.8}$$

Combining Equations (3.7) and (3.8), we conclude that in the operating trajectory of Figure 3.4. the load current varies linearly with R for a particular V_{0N}. For this reason, trajectories of the type shown in Figure 3.4 are referred to as that due to linear operation [6].

For the cycle shown in Figure 3.3, a nonlinear relationship in the steady-state between R and $| V_{C0N} |$ can be derived. The derivation is now given following [6]. Considering the positive i_{LN} half cycle, the coordinates of the transition point between Q1-Q4 mode and Q1-D2 mode can be written in terms of the radius $r_1 = | V_{C0N} | + V_{SN} - V_{0N}$ and the angle θ_1 subtended by Q1-Q4 mode at its centre $(V_{SN} - V_{0N}, 0)$. These coordinates are expressed as a complex number with real and imaginary parts being the scaled capacitor voltage and scaled inductor current as per Equation (3.9):

$$r_1 e^{j(\pi - \theta_1)} + V_{SN} - V_{0N} \tag{3.9}$$

In Equation (3.9), $j = \sqrt{-1}$ and e denotes the base of the natural logarithm.

Likewise, the coordinates of the transition points between Q1-D2 mode and D2-D3 mode can be written in terms of the radius $r_2 = | V_{C0N} | + V_{SN} + V_{0N}$ and angle θ_2 subtended by D2-D3 mode at its centre $(-V_{SN} - V_{0N}, 0)$ as the real and imaginary parts of the complex number given below in Equation (3.10):

$$r_2 e^{j\theta_2} - V_{SN} - V_{0N} \tag{3.10}$$

The coordinates of these two points in Equations (3.9), (3.10) form the extremities of the arc of a circle with the same radius R from centre $(-V_{0N}, 0)$. This arc subtends the angle θ_3 at the centre $(-V_{0N}, 0)$. Hence the coordinates of these two points are related by the following complex number relationship given in Equation(3.11):

$$\left(r_2 e^{j\theta_2} - V_{SN}\right) e^{j\theta_3} = r_1 e^{j(\pi - \theta_1)} + V_{SN} \tag{3.11}$$

The angle θ_3 is related to θ_1 and θ_2 by the relation of Equation (3.12) which arises from the time taken to complete a half cycle in this converter.

$$\theta_1 + \theta_2 + \theta_3 = \frac{\pi \omega_0}{\omega_S} \tag{3.12}$$

Using Equation (3.12) in Equation (3.11) and rearranging terms and using $V_{SN} = 1$, Equation (3.13) is obtained:

$$r_2 e^{j\left(\frac{\pi\omega_0}{\omega_S} - \theta_1\right)} - r_1 e^{j(\pi - \theta_1)} - 1 = e^{j\theta_3} \tag{3.13}$$

Taking the magnitude of both sides of Equation (3.13), Equation (3.14) is obtained as:

$$\left| r_2 e^{j\left(\frac{\pi\omega_0}{\omega_S} - \theta_1\right)} - r_1 e^{j(\pi - \theta_1)} - 1 \right| = 1 \tag{3.14}$$

Reproduced with permission of the copyright owner. Further reproduction prohibited without permission.

From Figure 3.3, using the cosine rule on the triangle formed by the centres ($V_{SN} - V_{0N}$, 0), ($-V_{0N}$, 0) and the transition point between Q1-Q4 mode to Q1-D2 mode, Equation (3.15) can be written with V_{SN}=1 as:

$$\cos\theta_1 = \frac{{r_1}^2 + 1 - R^2}{2r_1} \tag{3.15}$$

Now using Equation (3.15), in Equation (3.14) and defining $a = cos(\pi\omega_0/\omega_S)$ and simplifying algebraically, Equation (3.16) is obtained:

$$\begin{aligned}&\left[{r_1}^2 + {r_2}^2 + 2r_1r_2a\right]R^4 + \left[2\left(r_1r_2a - 1\right)\left({r_1}^2 + {r_2}^2 + 2r_1r_2a\right)\right]R^2 + \\ &\left[\left({r_1}^2 + {r_2}^2\right)\left(1 + {r_1}^2{r_2}^2\right) - 2r_1r_2a\left({r_1}^2 + {r_2}^2 - 1 - {r_1}^2{r_2}^2\right) - 4{r_1}^2{r_2}^2\right] = 0\end{aligned} \tag{3.16}$$

Finally, using $r_2 = (\mid V_{C0N} \mid +1 + V_{0N})$ and $r_1 = (\mid V_{C0N} \mid +1 - V_{0N})$ in Equation (3.16) the nonlinear relationship between R and $\mid V_{C0N} \mid$ is given by the implicit Equation (3.17):

$$a_4R^4 + a_2R^2 + a_0 = 0 \tag{3.17}$$

where a_4, a_2 and a_0 are multivariate polynomials expressed in terms of $\mid V_{C0N} \mid$, V_{0N} and a.

a_0, a_2 and a_4 are obtained from Equation (3.16), with the substitution of r_2 and r_1 and is given by Equations (3.18), (3.19) and (3.20) with $\alpha = \mid V_{C0N} \mid$ [6]. The simplifications of Equations (3.14) to (3.16) and the final simplifications referred to above are carried out using Maple [18], a symbolic computing package. Maple code for these simplifications is provided in Appendix A.4.

$$\begin{aligned}
a_0 &= (2-2a)V_{0N}^6 + (10a-6)V_{0N}^4 + (8-8a)V_{0N}^2 + \\
&\quad \alpha((12a-4)V_{0N}^4 + (8-26a)V_{0N}^2) + \\
&\quad \alpha^2((6a-2)V_{0N}^4 - (36a+4)V_{0N}^2 + 8a + 8) + \\
&\quad \alpha^3(-(8+24a)V_{0N}^2 + 24a + 24) + \\
&\quad \alpha^4(-(6a+2)V_{0N}^2 + 26a + 26) + \\
&\quad \alpha^5(12a+12) + \alpha^6(2+2a) && (3.18)\\
a_2 &= (4a^2-4a)V_{0N}^4 + (4a-8a^2-4)V_{0N}^2 + (4a^2-4) + \\
&\quad \alpha(8a-8+16a^2-16V_{0N}^2a^2) + \alpha^2(20a-8V_{0N}^2a^2+24a^2-4) + \\
&\quad \alpha^3(16a+16a^2) + \alpha^4(4a+4a^2) && (3.19)\\
a_4 &= (2-2a)V_{0N}^2 + 2 + 2a + \alpha(4+4a) + \alpha^2(2+2a) && (3.20)
\end{aligned}$$

Due to the nonlinearity of Equation (3.17), trajectories of the type shown in Figure 3.3 will be referred to as that due to nonlinear operation.

Parameter R characterizes the "instantaneous " tank energy of the CF-SRC in each cycle. Therefore, it can be used for controlling the energy transfer between the supply, load and the tank circuit of the CF-SRC in a manner akin to [5, 6, 7, 8, 9]. Such a direct control of the tank energy would force the inductor current and capacitor voltage to settle into their steady state trajectory in minimum time with low transients.

Reproduced with permission of the copyright owner. Further reproduction prohibited without permission.

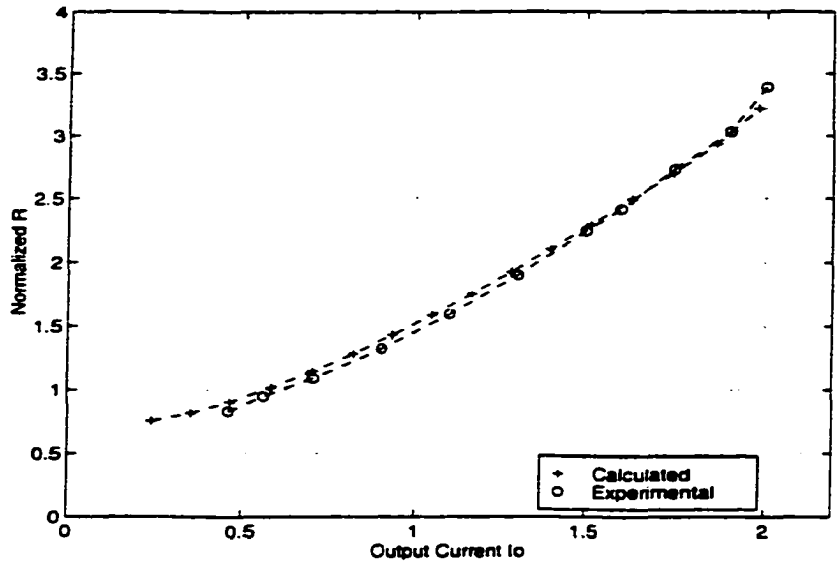

Figure 3.5: R variation with Load Current for $V_0/V_S = 0.25$

3.2.3 Steady state Characteristics

In steady state, the relationship between the parameter R and the load current I_0 for a specific output voltage V_0 for a particular ω_S in both calculations and experiments is shown in Figure 3.5. The calculated results are obtained by giving a constant value to V_{0N} (with $V_{SN} = 1$) and a set of values to V_{C0N}, solving Equations (3.7), (3.8) and (3.17) to get associated values of R and I_0. In Figure 3.5, calculated results and experimental results match each other very well. Note that the R varies monotonically with the load current for a particular V_0 and therefore it can be used as an effective control variable for the circuit. Furthermore, for small load currents this relationship is linear and for large currents it is nonlinear, corresponding to linear and nonlinear trajectories of operation respectively. The transition between the linear and nonlinear ranges occur when $\theta_3 = 0$, which corresponds to the switching of Q1 and Q3 precisely at the zero crossings of the inductor current. This transition point provides the upper bound for R in Equation (3.8) and lower bound in Equation (3.17). The maximum load current that the linear cycle of operation can supply is obtained by solving these Equations simultaneously for $\mid V_{C0N} \mid$ and using Equation (3.7).

In Figure 3.6, a plot of the variation of the maximum load current with V_0 is depicted. The maximum load current that the nonlinear operating trajectory can supply is obtained from the steady state trajectory in Figure 3.3 with θ_2=0. The maximum load currents were obtained in the laboratory for the nonlinear mode by setting the phase shift between the two sets of switching signals to a maximum (allowable on isolated MOSFET driver boards) and then adjusting load resistance to record voltage and current. To obtain the maximum load currents in the laboratory for linear mode, both load resistance and phase shift were adjusted to find the transition values (θ_3=0) of output voltage and current.

Reproduced with permission of the copyright owner. Further reproduction prohibited without permission.

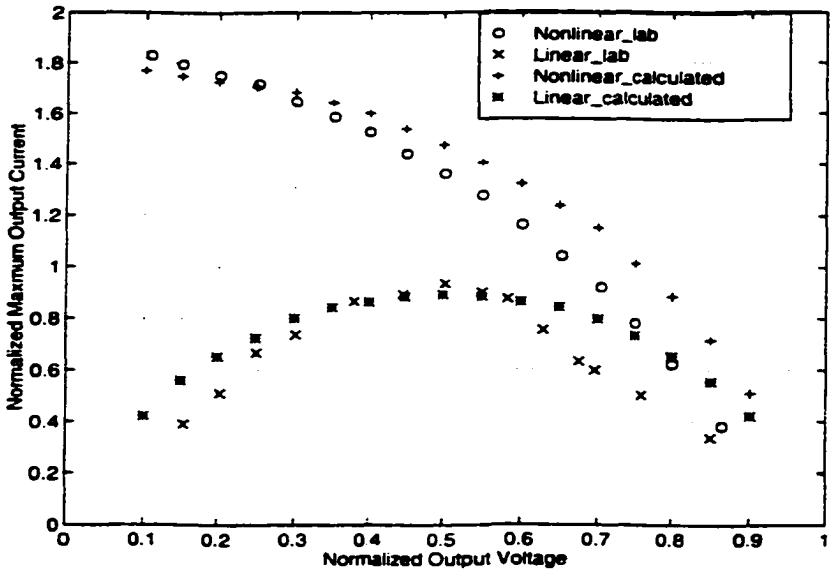

Figure 3.6: Maximum I_0 Variation with V_0 In Nonlinear and Linear Operation

It is a difficult measurement to adjust for. In the calculations, it is assumed that tank circuit has no resistance, switches are ideal and there are no losses. Within measurement errors and idealized lossless calculations, Figure 3.6 depicts good agreement with theoretical Equations (3.8), (3.12), (3.17), (3.18), (3.19) and (3.20). Note that the maximum current decreases with increasing V_0 and that with the output short circuited (V_0=0), the maximum current from the CF-SRC is finite thus providing short circuit protection. The calculations in Figures 3.5 and 3.6 are based on the ideal equations above and neglect losses in the circuit and assume ideal switching devices and drivers. The experimental results take into account losses in the circuit. The good match of the experimental to calculated results indicates that modelling without losses which is conducive to developing analytical equations, provides good predictive albeit optimistic results (in terms of load current in Figure 3.6) compared with experimental results. However losses while having some effects on these predictions (Figures 3.5 and 3.6) do not significantly affect these predictions.

3.3 Optimal Trajectory Control of CF-SRC

With reference to Figures 3.3 and 3.4, the optimal trajectory control objective is to determine the switching instants of Q2 and Q4 which would force the inductor current and capacitor voltage to trace their optimal trajectory at the operating cycle. With this objective, the transients can be kept to a minimum and the system can reach its steaty state in minimum time. To meet this, when the CF-SRC is operating in Q1-Q4 mode (or Q2-Q3 mode), the distance r of the trajectory measured from the center of Q1-D2 mode (or Q3-D4 mode) is continuously monitored. And when r $\geq$ R, Q2 (Q4) is switched off. In the Q1-Q4 mode, distance r is given by:

Reproduced with permission of the copyright owner. Further reproduction prohibited without permission.

$$r^2 = (v_{CN} + V_{0N})^2 + i_{LN}^2 \tag{3.21}$$

In Q2-Q3 mode, distance r is given by:

$$r^2 = (v_{CN} - V_{0N})^2 + i_{LN}^2 \tag{3.22}$$

Thus the control law for switching off Q2 and Q4 can be given by:

$$(v_{CN} \pm V_{0N})^2 + i_{LN}^2 \geq R^2 \tag{3.23}$$

where + sign is for switching Q4 off and - sign is for switching Q2 off.

This control law requires continuous measurement of normalized inductor current and squaring calculation. It is to be simplified as in variable frequency operation to avoid this continuous measurement and normalization.

3.3.1 Implementation Aspects

The Optimal Trajectory Control (OTC) law given by Equation (3.23) has a nonlinear form. As discussed in variable frequency operation of SRC, i_{LN} is the scaled value of the inductor current with scaling by the characteristic impedance of the tank circuit Z_0. This scaling requires precise knowledge of the ratio of parameters L and C in the tank circuit. More significantly, this ratio is prone to vary during operation due to effects such as inductor saturation and thermal effects. A change in this ratio will introduce significant errors which undermine the advantages of optimal trajectory control. To develop a robust form for OTC, the scaled current will be eliminated in the following.

As the state plane trajectory of each mode is a circular arc with known centre and radius determined by initial conditions, it is possible to simplify the optimal trajectory control law of Equation (3.23) as in Chapter 2 and [5, 6].

Control Law Simplification for Nonlinear Operation

The simplified control law for switching Q4 off is derived here. From Figure 3.7 with the capacitor voltage at zero crossing from negative to positive inductor current denoted by V_{C0N-}, Equation (3.24) can be written.

$$\rho^2 = (\mid V_{C0N-} \mid + V_{SN} - V_{0N})^2 = (V_{SN} - V_{0N} - v_{CN})^2 + i_{LN}^2 \tag{3.24}$$

Therefore, i_{LN} can be described as:

$$\begin{aligned} i_{LN}^2 &= (\mid V_{C0N-} \mid + V_{SN} - V_{0N})^2 - (V_{SN} - V_{0N} - v_{CN})^2 \\ &= \mid V_{C0N-} \mid^2 - v_{CN}^2 + 2(\mid V_{C0N-} \mid + v_{CN})(V_{SN} - V_{0N}) \end{aligned} \tag{3.25}$$

Substituting Equation (3.25) into control law (3.23) for switching Q4 off, Equation (3.26) is derived:

Reproduced with permission of the copyright owner. Further reproduction prohibited without permission.

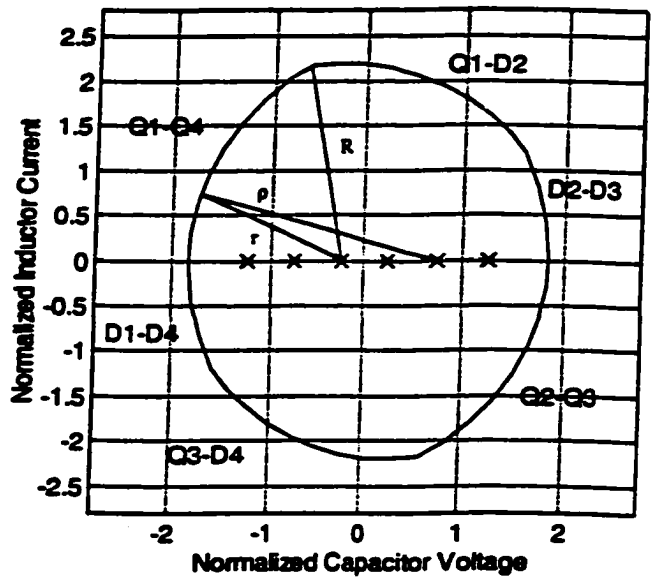

Figure 3.7: Control Law Simplification for Nonlinear Mode

$$\begin{aligned} r^2 &= (v_{CN} + V_{0N})^2 + |V_{C0N-}|^2 - v_{CN}^2 + 2(|V_{C0N-}| + v_{CN})(V_{SN} - V_{0N}) \\ &= (|V_{C0N-}| + V_{0N})^2 + 2V_{SN}(v_{CN} + |V_{C0N-}|) \geq R^2 \end{aligned} \tag{3.26}$$

Likewise, the simplified control law for switching Q2 off can be derived as:

$$r^2 = (|V_{C0N+}| - V_{0N})^2 + 2V_{SN}(|V_{C0N+}| - v_{CN}) \geq R^2 \tag{3.27}$$

where V_{C0N+} is the capacitor voltage at the zero crossing of the inductor current from positive to negative.

Control Law Simplification for Linear Operation

For the linear operation, the simplified control law can be derived as follows from Figure 3.8:

$$\begin{aligned} \lambda^2 &= (V_{C0N-} + V_{0N})^2 \\ d^2 &= \lambda^2 - (V_{CSN-} + V_{0N})^2 \\ \rho^2 &= d^2 + (V_{SN} - V_{0N} - V_{CSN-})^2 = (V_{SN} - V_{0N} - V_{CN})^2 + i_{LN}^2 \end{aligned}$$

where V_{CSN-} is the capacitor voltage when Q1 is switched on and V_{C0N-} is the capacitor voltage at zero crossing of the inductor current from negative to positive direction. By using the above Equations, i_{LN} can be described as:

$$\begin{aligned} i_{LN}^2 &= d^2 + (V_{SN} - V_{0N} - V_{CSN-})^2 - (V_{SN-} - V_{0N} - V_{CN})^2 \\ &= V_{C0N-}^2 + 2V_{0N}V_{C0N-} - 2V_{CSN-}V_{SN} - V_{CN}^2 + 2V_{CN}(V_{SN-} - V_{0N}) \end{aligned} \tag{3.28}$$

Reproduced with permission of the copyright owner. Further reproduction prohibited without permission.

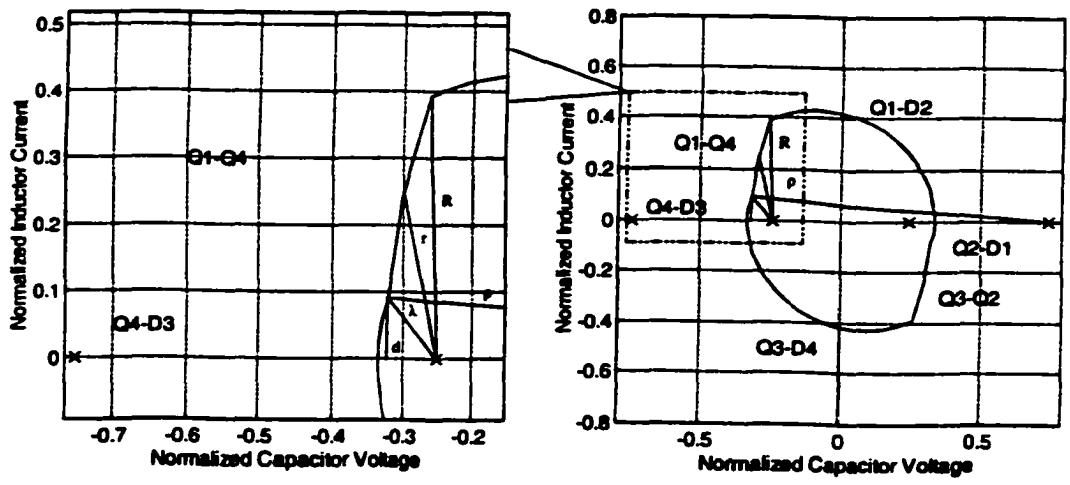

Figure 3.8: Control Law Simplification for Linear Mode

Substituting Equation (3.28) into the control law in Equation (3.23), the simplified control law given in Equation (3.29) for switching Q4 off is obtained:

$$r^2 = (V_{C0N-} + V_{0N})^2 + 2V_{SN}(v_{CN} - V_{CSN-}) \geq R^2 \tag{3.29}$$

Likewise, the simplified control law for switching Q2 off is given by:

$$r^2 = (V_{C0N+} - V_{0N})^2 + 2V_{SN}(V_{CSN+} - v_{CN}) \geq R^2 \tag{3.30}$$

where V_{CSN+} is the capacitor voltage at the switching on instant of switch Q3 and V_{C0N+} is the capacitor voltage at zero crossing of the inductor current from positive to negative direction.

3.3.2 Multirate Control Strategy

In this subsection, it is shown that Equations (3.26) and (3.27) for CF-SRC can be thought of as a multirate modified capacitor voltage feedback control strategy as discussed in Section 2.4.2 for VF-SRC.

For nonlinear operation mode in Equations (3.26) and (3.27), we observe that during a half cycle of a trajectory, V_{C0N-} or V_{C0N+} is a constant equal to the peak value of capacitor voltage at the start of the half cycle. In such a half cycle, the dynamics of V_{SN} and V_{0N} can be neglected as the switching frequency of the converter is much higher than the dynamics of V_{SN} or the filtered V_{0N}. Therefore, within a half cycle, the left hand side of Equations (3.26) and (3.27) vary linearly with the instantaneous capacitor voltage v_{CN}. Consequently, the optimal trajectory control law of [6] is a modified form of (instantaneous, linear) capacitor voltage control law studied in [8] with a quadratic function of V_{C0N} being added at each half cycle to the linear capacitor voltage control law

Reproduced with permission of the copyright owner. Further reproduction prohibited without permission.

of [8]. Hence Equations (3.26) and (3.27) are referred to as modified capacitor voltage control form of the OTC laws [6]. In the sense that the modification to the linear control law is done once every half cycle, the optimal trajectory control law has a pseudo-linear multirate form developed below as in Section 2.4.2. The control law in Equation (3.26) can be expanded and simplified as:

$$| V_{C0N-} |^2 + 2(V_{SN} - V_{0N}) | V_{C0N-} | + 2V_{SN}v_{CN} + V_{0N}^2 \geq R^2 \tag{3.31}$$

Letting $K_1 = 2V_{SN}$, $K_2 = V_{0N}^2$ and defining a quadratic function $f(x) = x^2 + 2(V_{SN} - V_{0N})x$, then with $f(| V_{C0N-} |) = | V_{C0N-} |^2 + 2(V_{SN} - V_{0N}) | V_{C0N-} |$, Equation (3.26) can be written as:

$$f(| V_{C0N-} |) + K_1 v_{CN} + K_2 \geq R^2$$

In above Equation, $K_1 v_{CN}$ is the instantaneous linear feedback term while $f_1(| V_{C0N-} |)$ is updated every half cycle. K_2 can be considered as a constant in each half cycle.

The control law in Equation (3.27) can be expanded and simplified as:

$$| V_{C0N+} |^2 + 2(V_{SN} - V_{0N}) | V_{C0N+} | - 2V_{SN}v_{CN} + V_{0N}^2 \geq R^2 \tag{3.32}$$

Letting $K_1 = 2V_{SN}$, $K_2 = V_{0N}^2$ and defining a quadratic function $f(x) = x^2 + 2(V_{SN} - V_{0N})x$, then with $f(| V_{C0N+} |) = | V_{C0N+} |^2 + 2(V_{SN} - V_{0N}) | V_{C0N+} |$, Equation (3.27) can be written as:

$$f(| V_{C0N+} |) - K_1 v_{CN} + K_2 \geq R^2$$

As before, $K_1 v_{CN}$ is the instantaneous linear feedback term while $f(| V_{C0N+} |)$ is updated every half cycle. K_2 can be considered as a constant in each half cycle.

The discussion above shows that both Equations (3.26) and (3.27) have a similar multirate control structure depicted in the inner feedback loops of Figure 3.9. In Figure 3.9, $\pm K_1 v_{CN}$ is in continuous operation. The second loop for K_2 and $f(| V_{C0N} |)$ is updated at the begining of each half cycle. The outermost loop in Figure 3.9 is a PI controller to generate R based on V_0 and V_{ref}, as discussed in Section 2.4.2.

The similar discussion can be developed for linear operation mode but is not considered here as in this thesis the linear operation mode is not studied further due to its low power output.

3.4 Results

The performance of the robust optimal trajectory control scheme discussed in Section 3.3 is studied first by simulations and then implemented on a CF-SRC circuit in the laboratory.

3.4.1 Simulation Results

Like the simulation in variable frequency operation, CF-SRC is simulated in a computer using C code. Switches are considered ideal in these simulations. Tank circuit is assumed to have no resistance. The parameters used in the simulations are listed in Table 3.2. Normalized values of appropriate parameters are shown in brackets in Table 3.2.

Reproduced with permission of the copyright owner. Further reproduction prohibited without permission.

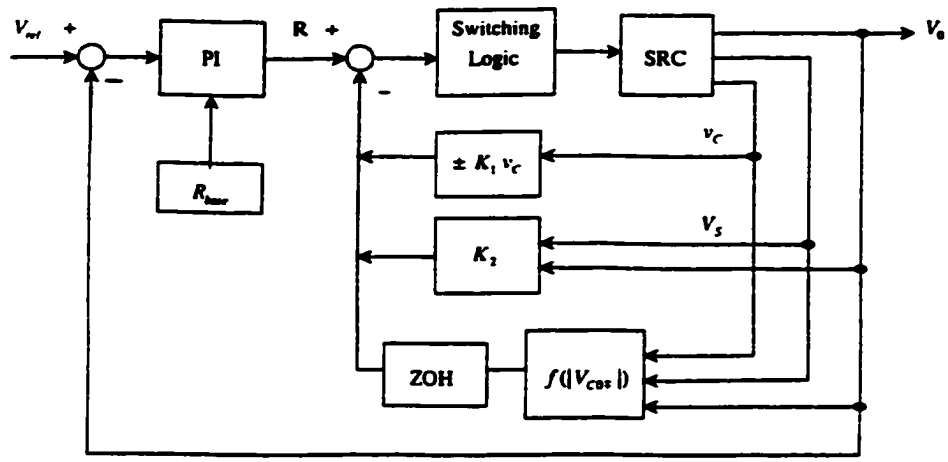

Figure 3.9: Multirate Control Scheme of CF-SRC

V_{SN}	20V (1)	V_{ON}	5V (0.25)
L	$88.6\mu H$	C	$0.68\mu F$
C_L	470 μF	R_{Load}	4.0 Ω (0.35) (Low Current) 2.0 Ω (0.18) (High Current)
Z_0	11.46Ω (1)	R_{base}	26.8V (1.34)
f_0 (Resonant)	20.5kHz	f_S	25kHz
P gain	150	I gain	650000

Table 3.2: Parameters in Simulations for CF-SRC

Simulation of Nonlinear Operation

Figure 3.10 shows the waveforms of simplified control law at steady state for switching Q4 and Q2 off in nonlinear mode of operation, where:

$$\begin{aligned} a_1 &= 2V_{SN}(v_{CN}+ \mid V_{C0N-} \mid) \\ b_1 &= R^2 - (\mid V_{C0N-} \mid + V_{0N})^2 \\ a_2 &= 2V_{SN}(\mid V_{C0N+} \mid - v_{CN}) \\ b_2 &= R^2 - (\mid V_{C0N+} \mid - V_{0N})^2 \end{aligned} \tag{3.33}$$

according to the control law, if $a_1 \geq b_1$, Q4 is to be turned off. If $a_2 \geq b_2$, Q2 is to be turned off. By using the switching signal produced by this control law, the steady state result in state plane diagram has been shown in Figure 3.3.

Figure 3.11 shows the transient response of i_{LN} and v_{CN} in state plane when load is increased by a step of 50% (R_{Load} from 4Ω to 2Ω, I_0 from 1.25A to 2.5A). It takes 2 ~ 3 cycles for i_{LN} and v_{CN} to settle. Figure 3.12 shows the corresponding transient for total R.

Figure 3.13 shows the transient response of i_{LN} and v_{CN} in state plane when load resistance is decreased by a step of 50% (R_{Load} from 2Ω to 4Ω, I_0 from 2.5A to 1.25A).

Reproduced with permission of the copyright owner. Further reproduction prohibited without permission.

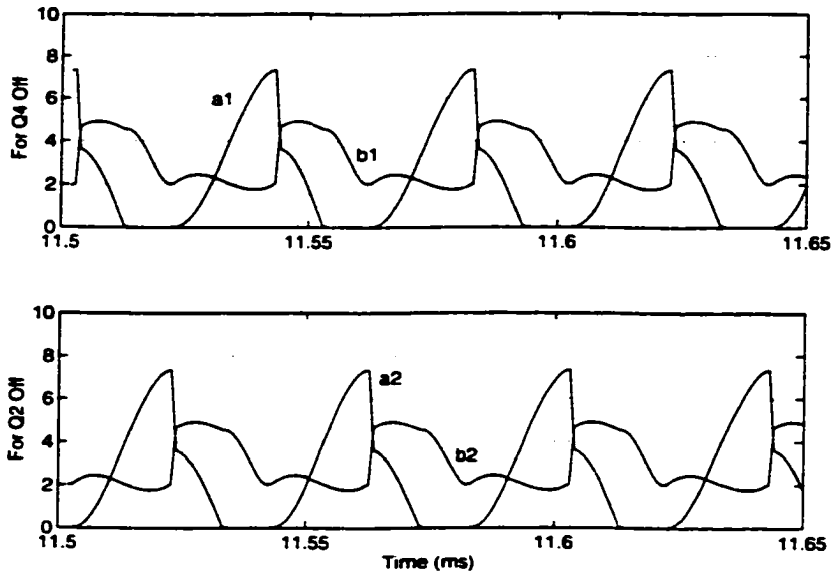

Figure 3.10: Simplified Control Law (Nonlinear-Simulation)

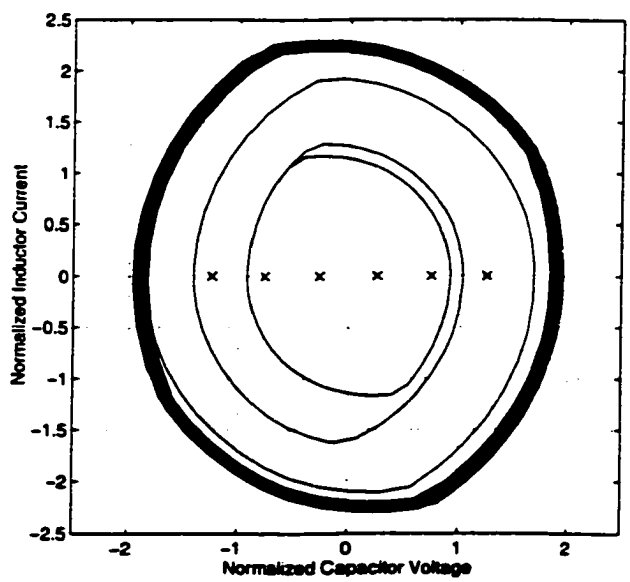

Figure 3.11: Transient of i_{LN} and v_{CN} (Nonlinear-Simulation-Increasing Load)

Reproduced with permission of the copyright owner. Further reproduction prohibited without permission.

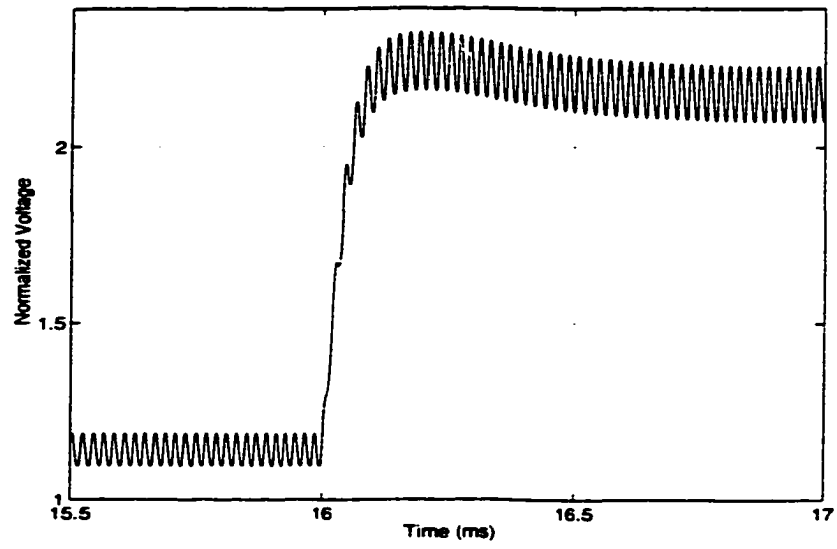

Figure 3.12: Transient of R (Nonlinear-Simulation-Increasing Load)

It also takes 2 ~ 3 cycles for i_{LN} and v_{CN} to settle. Figure 3.14 shows the corresponding transient of total R.

The transient of output voltage is shown in Figure 3.15. During 0 ~ 8ms, CF-SRC is started by function generator at a constant frequency f_S = 25kHz with a phase shift of about 90 degrees between the two arms of the CF-SRC. During this phase of operation even after system settles, output voltage does not reach the setpoint 0.25. During 8 ~ 12ms, modified OTC takes over function generator and the PI controller pushes the output voltage to track the setpoint without any overshoot. During 12 ~ 16 ms, there is a decreasing load change (I_0 from 2.5A to 1.25A). The settling time is less than 0.5ms. During 16 ~ 20ms, there is an increasing load change (I_0 from 1.25A to 2.5A). The settling time is about 0.5ms. Compared to the simulation results of VF-SRC, there are less overshoots and shorter settling times in CF-SRC simulations for similar parameter values. As mentioned in Section 2.5.1, the transient of R in Figures 3.12 and 3.14 have ripples. Therefore, the trajectories in Figure 3.11 and 3.13 have bands after settling down.

Simulation of Linear Operation

Because the load current (and output power) is small in linear operation mode, in this thesis the linear mode of CF-SRC is not studied further in the experiments. The simulation of linear mode depicted is to verify the theory. Figure 3.16 shows the steady state of linear mode in state plane with steady state R_{Load} = 15Ω. No experimental results are presented on this mode beyond those that are shown in Figures 3.5, 3.6, 3.16 and 3.26.

Reproduced with permission of the copyright owner. Further reproduction prohibited without permission.

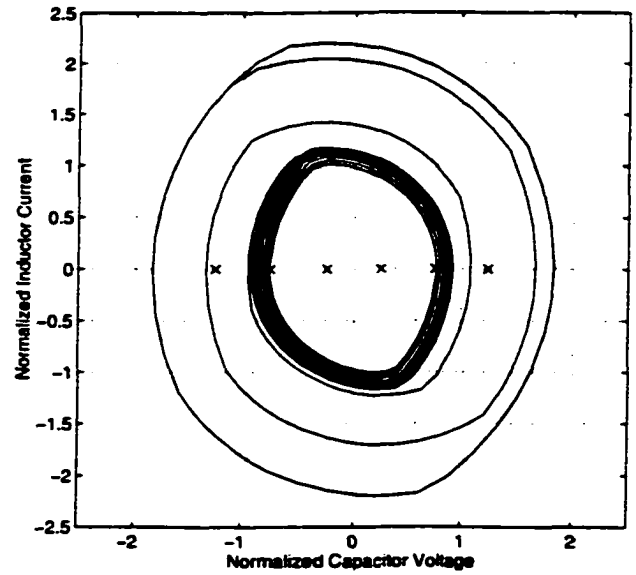

Figure 3.13: Transient of i_{LN} and v_{CN} (Nonlinear-Simulation-Decreasing Load)

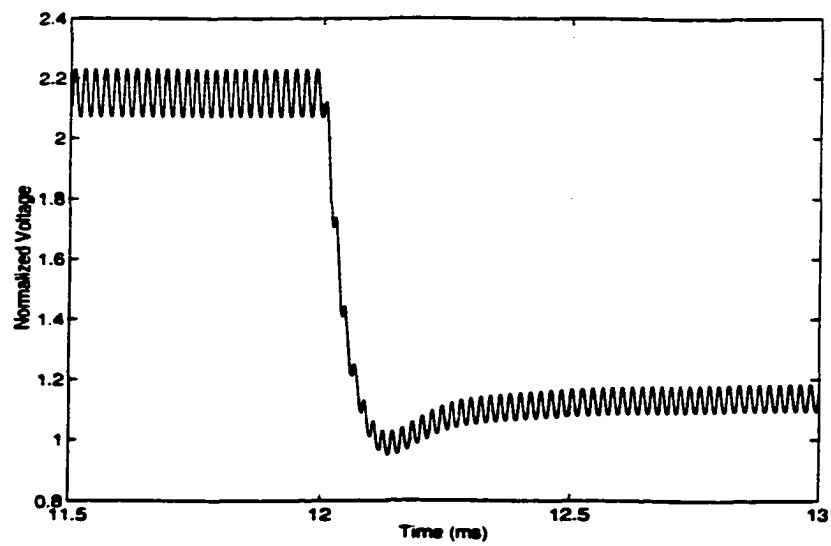

Figure 3.14: Transient of R (Nonlinear-Simulation-Decreasing Load)

Reproduced with permission of the copyright owner. Further reproduction prohibited without permission.

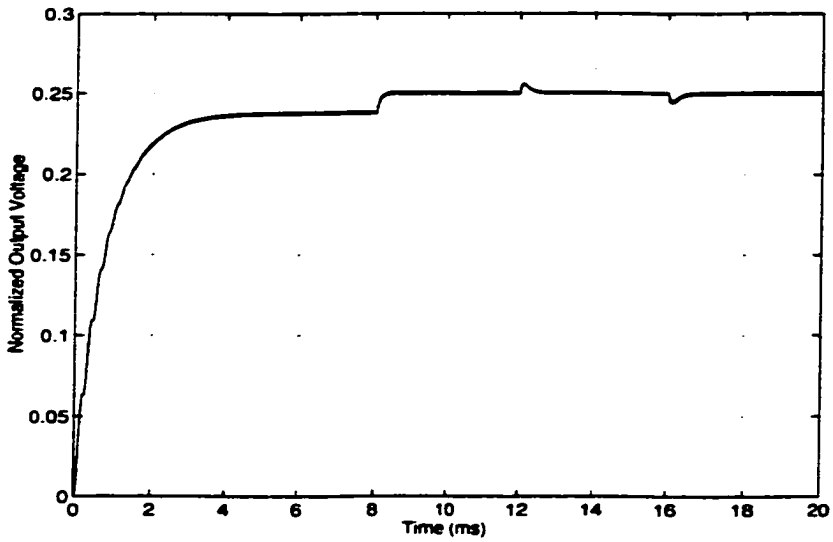

Figure 3.15: Transient of Output Voltage V_{ON} (Simulation)

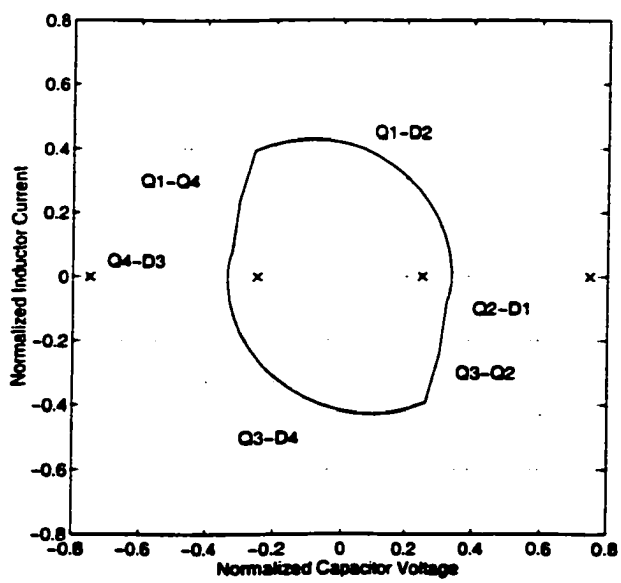

Figure 3.16: Steady State of i_{LN} and v_{CN} (Linear-Simulation)

Reproduced with permission of the copyright owner. Further reproduction prohibited without permission.

3.4.2 Experimental Results

The same CF-SRC considered in simulation is tested using an experimental CF-SRC circuit with nominal parameters listed in Table 3.3.

V_{SN}	20V (1)	V_{0N}	5V (0.25)
L	$88.6\mu H$	C	$0.68\mu F$
C_L	470 μF	R_{Load}	4.0 Ω (0.35) (Low Current) 2.0 Ω (0.18) (High Current)
Z_0	11.46Ω (1)	R_{base}	22V (1.1)
f_0 (Resonant)	20.55kHz	f_S	25kHz
P gain	75	I gain	532000

Table 3.3: Parameters in Experiments for CF-SRC

The same nominal values of circuit parameters are used for simulation and experiment. But R_{base}, P gain and I gain are different in Tables 3.2 and 3.3. As discussed in Section 2.6, in simulations, assumptions such as ideal switches, negligible tank circuit resistance, no parameter variations, etc. have been made. Thus the simulations have an ideal, lossless circuit. In addition, simulations have no additional low pass filtering on V_0, except that produced by output filter capacitor C_L. The level of ripple present is magnified when the PI controller operates on the error between V_0 and V_{ref} in producing R (Note the ripples in Figures 3.12 and 3.14). In the experimental circuit, additional filtering was introduced in control effort to reduce the ripples. The filter cut off frequency was 4kHz, the same as in variable frequency operation. Consequently, the filter introduces phase shift. Some phase shift is also introduced by the analog processing in the multipliers, etc. Finally losses in the circuit cause slight deviations of trajectories from the arcs of circles in the theoretical derivations. So while the simulations provide ideas of the possible PI gains to be used for control, the implementation gains were tuned to provide a compromise amongst settling time, transient response and noise for the 50% load change. R_{base} was adjusted to provide adequate range for the load change involved in the experimental setup.

Experimental Results of Nonlinear Operation

This implementation is based on the logic diagram in Figure A.5. The basic ideas are to produce the left and right hand side of the control law in Equations (3.26) and (3.27) after rearranging the two terms (R^2 and $(V_{C0N\pm} - V_{0N})^2$) containing squares to be together on one side of the inequality. The rearrangement (Equation (3.33)) makes it possible to write these two terms which involve a difference in squares as the product of a sum and difference of voltages and therefore reduces the multipliers needed for practical implementation.

Figure 3.17 shows the simplified control law in the experimental circuit. This figure obtained experimentally is comparable with the simulations shown in Figure 3.10 based on Equation (3.32).

Figure 3.18 shows the steady state waveforms of i_{LN} and v_{CN} in state plane with steady state $R_{Load} = 2\Omega$. Figure 3.19 shows the transient response of i_{LN} and v_{CN} in state plane when load is increased (R_{Load} from 4Ω to 2Ω, I_0 from 1.25A to 2.5A). It takes 3 ~ 4 cycles

Reproduced with permission of the copyright owner. Further reproduction prohibited without permission.

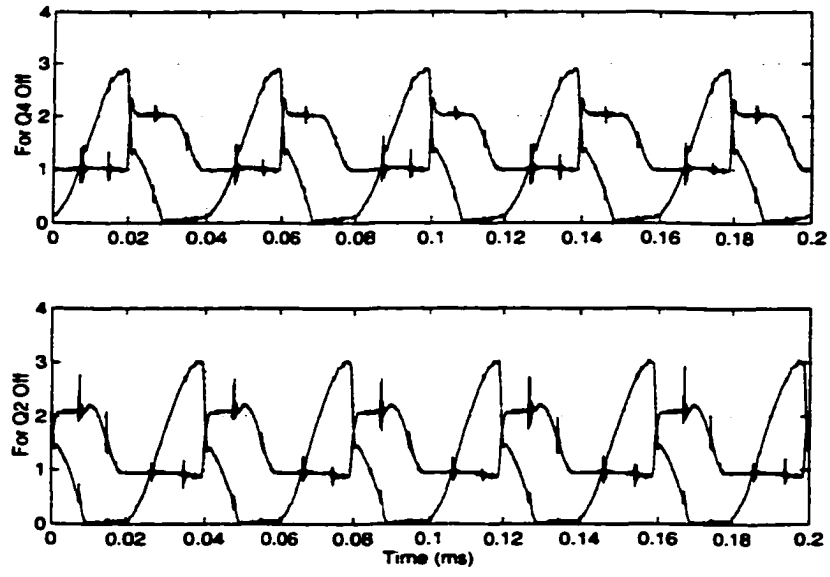

Figure 3.17: Simplified Control Law (Nonlinear-Lab)

for i_{LN} and v_{CN} to settle. This settling time is longer than the simulation result. Figure 3.20 shows the corresponding transient of total R. Figure 3.21 shows the corresponding transients of output voltage V_0 and process error. The variation of V_0 is about 2% which is much better than V_0 variation in the VF-SRC results of Chapter 2. The settling time for V_0 is about 0.4ms, shorter than the settling time of VF-SRC and comparable with simulations shown in Section 3.4.1.

Figure 3.22 through 3.24 show the results when load is decreased(R_{Load} from 2Ω to 4Ω. I_0 from 2.5A to 1.25A). In this transient, it takes about 2 ~ 3 cycles for i_{LN} and v_{CN} to settle with some undershoot. The V_0 variation is around 4%. The settling time for V_0 is 0.3ms. These results are also comparable with simulations in Section 3.4.1.

Experimental Results of Linear Operation

The experimental results of steady state linear mode operation are depicted in Figure 3.25 and are comparable with the corresponding simulation results shown in Figure 3.16. Figure 3.25 shows the steady state of i_{LN} and v_{CN} in state plane. In Figure 3.25. R_{Load} is 15 Ω, other parameters used in the linear mode are the same as those used in nonlinear mode listed in Table 3.3. Transient studies in this mode were not conducted in this thesis as the load current (output power) in this mode are small.

Robustness of Modified Capacitor Voltage Control Scheme

One of the advantages of the control scheme used in this thesis is that inductor current is eliminated from the control law. This makes the controller robust to circuit parameter (Z_0) changes. As shown in Figures 3.26 and 3.27, where inductor current i_L is measured with the sensor in saturation, the system performance with OTC control as modified in

Reproduced with permission of the copyright owner. Further reproduction prohibited without permission.

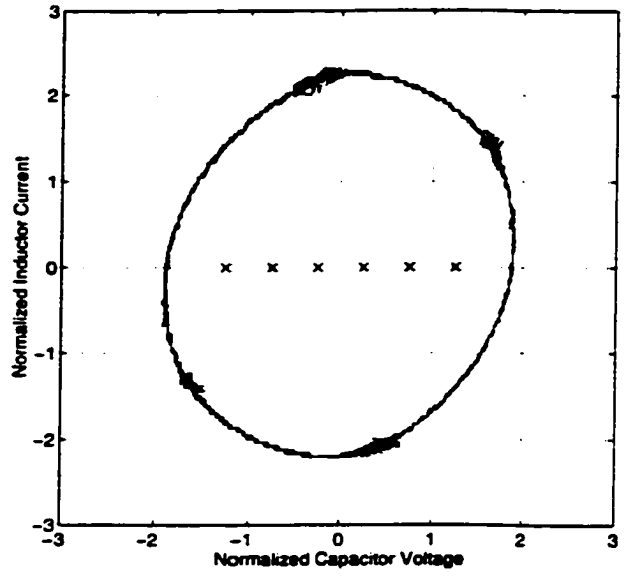

Figure 3.18: Steady State of i_{LN} and v_{CN} (Lab)

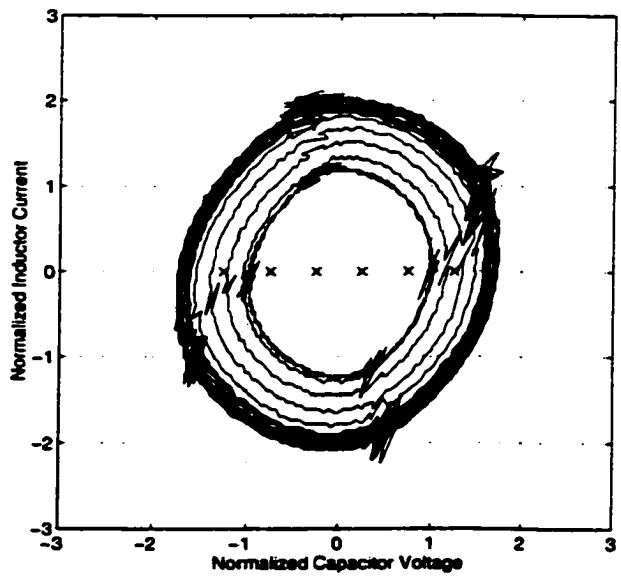

Figure 3.19: Transient of i_{LN} and v_{CN} (Lab-Increasing Load)

Reproduced with permission of the copyright owner. Further reproduction prohibited without permission.

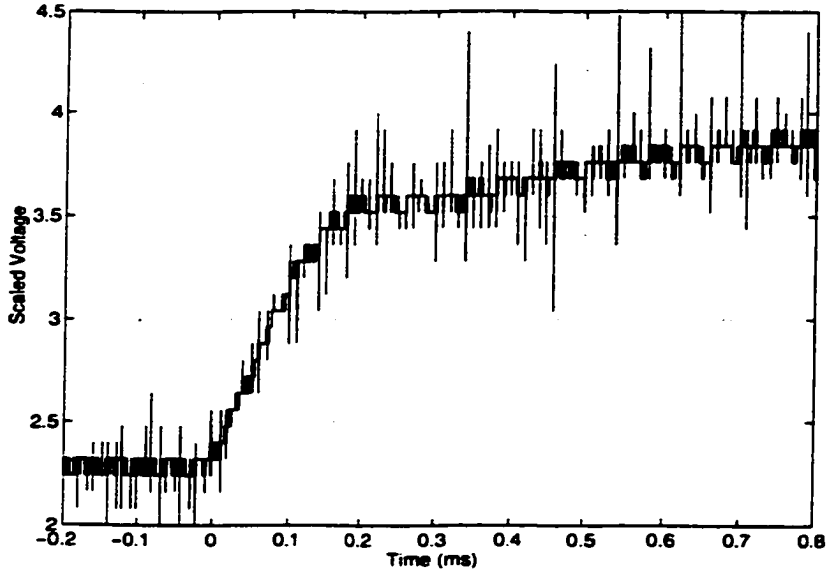

Figure 3.20: Transient of R (Lab-Increasing Load)

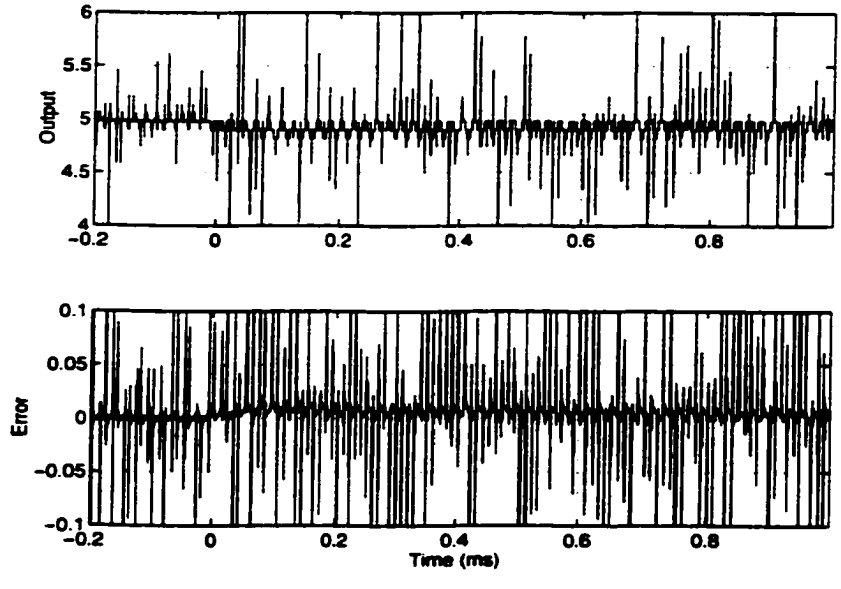

Figure 3.21: Transient of Output Voltage and Error (Lab-Increasing Load)

Reproduced with permission of the copyright owner. Further reproduction prohibited without permission.

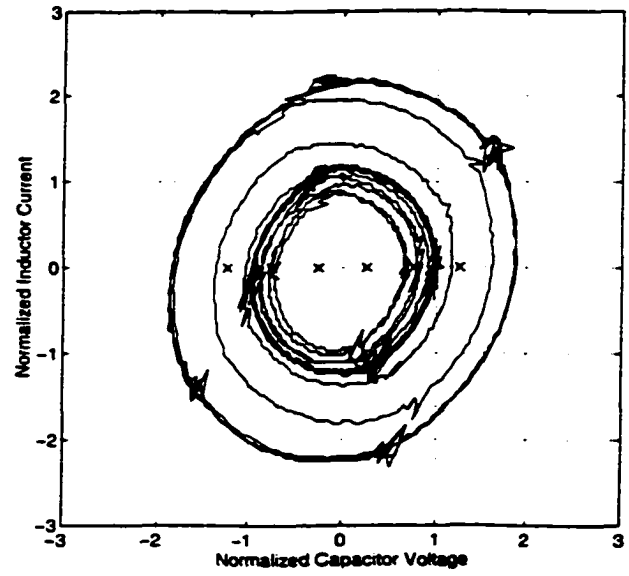

Figure 3.22: Transient of i_{LN} and v_{CN} (Lab-Decreasing Load)

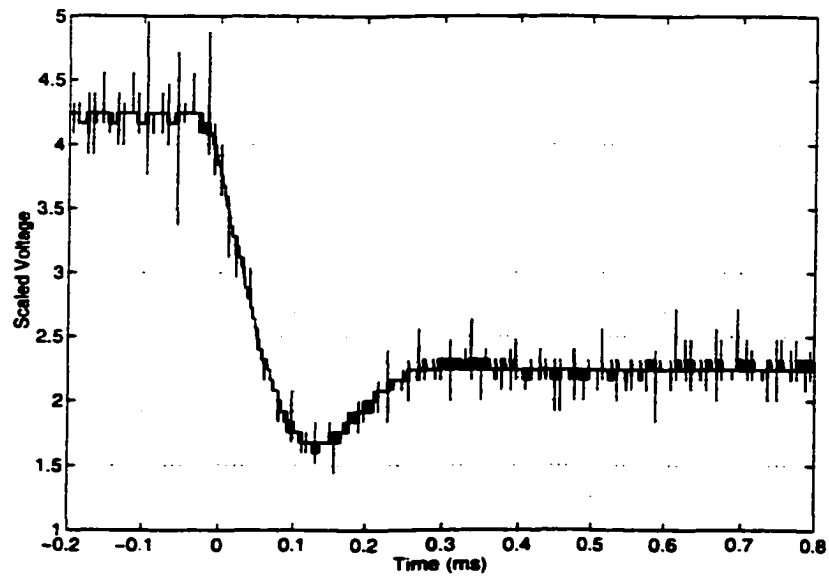

Figure 3.23: Transient of R (Lab-Decreasing Load)

Reproduced with permission of the copyright owner. Further reproduction prohibited without permission.

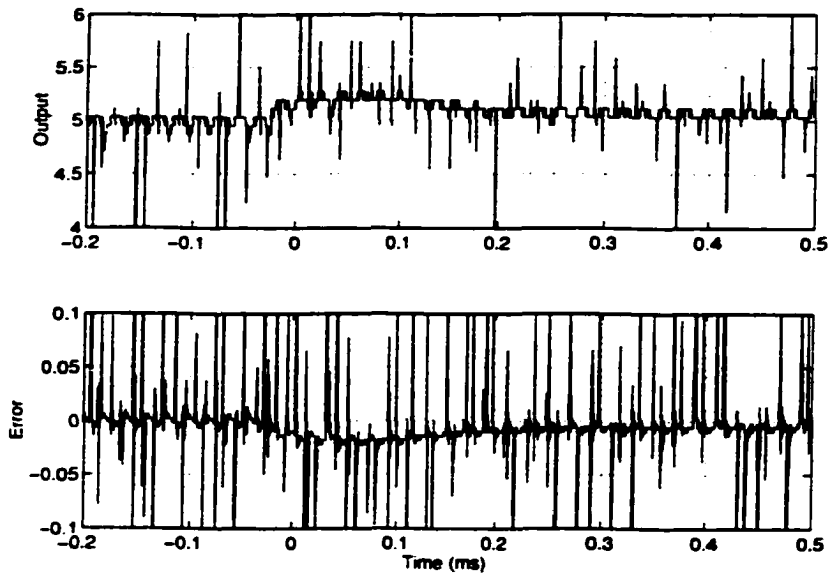

Figure 3.24: Transient of Output Voltage and Error (Lab-Decreasing Load)

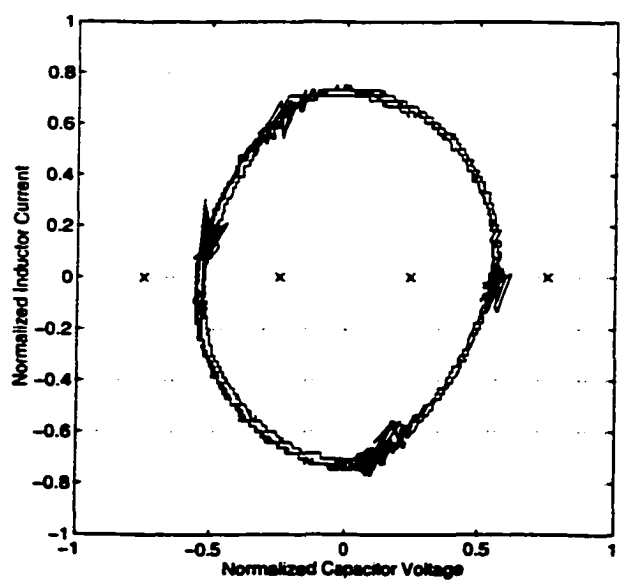

Figure 3.25: Steady State of i_{LN} and v_{CN} in Linear Mode (Lab)

Reproduced with permission of the copyright owner. Further reproduction prohibited without permission.

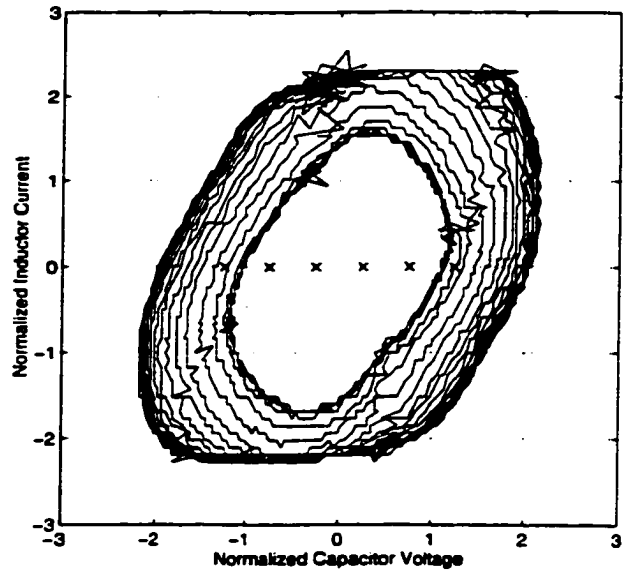

Figure 3.26: Performance of Controller with i_{LN} in Saturation (Increasing Load)

this thesis following [5, 6] is still stable and has good performance as before. Compared to other control schemes in [9, 12], the control scheme proposed in this thesis has a clear advantage against circuit parameter variations.

3.5 Conclusion

This Chapter has analyzed the CF-SRC in state plane and following [6] developed a control parameterization which can be used in optimal trajectory control of the CF-SRC. The optimal trajectory parameter R characterizes the instantaneous energy in the tank circuit and can be used to generate signals which force the tank energy to reach its steady state trajectory in minimum time. Under optimal trajectory control, the CF-SRC exhibits two stable steady state trajectories, one in which the relationship between the load current and the parameter R is linear and the other in which it is nonlinear [6]. Limits on the maximum load current obtainable from CF-SRC in its linear and nonlinear trajectories first obtained in [6] have been verified experimentally in this Chapter. The robust performance of the optimal trajectory control has been demonstrated through transient performance analysis in this work. The close match between the ideal (lossless) simulations of transient performance and the experimental results indicates that losses do not significantly affect the predictive ability of calculations and simulations done with the ideal models. While the simulations provide an ideal PI controller with high gains capable of better performance, the practical circuit requires additional noise filtering and the gains have to be tuned as a compromise between settling time, transient response and noise on the experimental circuit. The advantage of the optimal trajectory control is usually obscured by its nonlinearity and its implementation complexity. Following [6],

Reproduced with permission of the copyright owner. Further reproduction prohibited without permission.

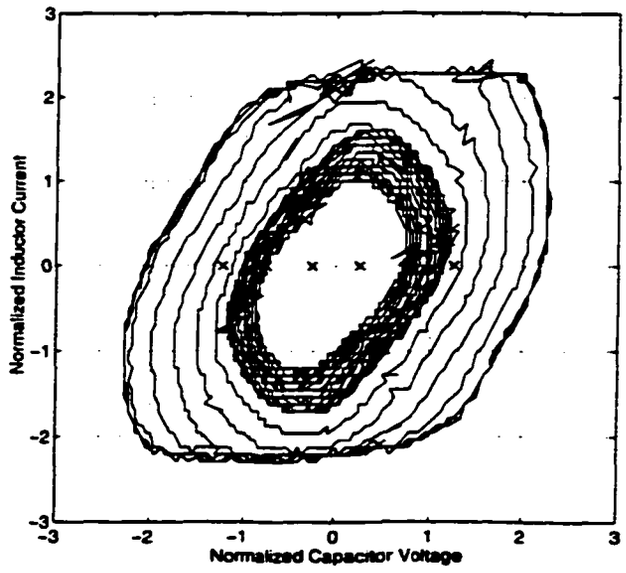

Figure 3.27: Performance of Controller with i_{LN} in Saturation (Decreasing Load)

this Chapter has addressed the task of simplifying the control law into a pseudo-linear form which can be implemented in a simple multirate framework. Results presented show the feasibility and the ease of use of such an approach in controlling the CF-SRC.

Reproduced with permission of the copyright owner. Further reproduction prohibited without permission.

Chapter 4

Conclusion and Future Work

Two Series Resonant Converters (SRC) have been studied in this thesis. In Chapter 2, a half-bridge SRC was studied in variable frequency operating mode (below and above resonant frequency). In Chapter 3, a full-bridge SRC was studied in constant frequency operating mode (non-linear mode). State-plane analysis was used in this thesis to develop the control laws of Optimal Trajectory Control (OTC). The control laws were simulated in a computer and further simplified and successfully implemented in the lab. Both simulation and experimental results demonstrated the excellent performance of the multi-rate controller developed in this thesis.

The main contribution of this thesis is that the control laws are simplified and the inductor current measurement is no longer required. Consequently the implementation complexity is reduced, cost is reduced, the controller robustness is increased, as introduced and analyzed in Chapter 2 and Chapter 3.

The tank circuit of traditional SRC consists of one inductor and one capacitor. Therefore, the system is a second order system. New converters are proposed by adding one more inductor or capacitor in the tank circuit (LLC or LCC tank circuits [17]). It remains an open question as to whatever OTC can be extended to such converters. Compared to the conventional second order SRC, the third order SRC has improved characteristics, isolation and less component stresses. The suggestion for future work is to study and implement the modified type of OTC schemes for such third order resonant converters.

Reproduced with permission of the copyright owner. Further reproduction prohibited without permission.

Appendix A

A.1 Gate Drive Circuit

In this thesis, the MOSFETs are driven by DS0026 MOS drivers (now obsolete, but replacable by pin compatible UC3709). DS0026 may be driven from standard 54/74 series TTL voltage level.

In the circuits of this thesis, two MOSFETs are in series and then paralleled across a power supply (As shown in Figure 2.1 and Figure 3.1 for variable and constant frequency SRC). Three important considerations must be implemented in design of MOSFET drive circuit. The first consideration is that a fast supply of gate current is required as stated above. This consideration is implemented by selecting a suitable MOSFET driver, the DS0026 Chip. Since the point where the two MOSFETs are connected is not grounded, the second consideration is isolation. In this thesis, opto isolator H11L1 and HCPL261A are used to drive the isolated MOSFET switching signals from feedback signals. The H11L1 circuit is a slower version and operates up to 80kHz switching frequencies. The HCPL261A circuit operates up to 500kHz switching frequencies. The third consideration is the need for a lockout circuit to avoid power supply being shorted if the two MOSFETs are switched on accidentally at the same time. To guarantee safe operations of converters considered in this thesis, a reliable lockout circuit which ensures that both MOSFETs will not be on at the same time is very important. In the drive circuits of this thesis, two kinds of lockout circuits are used. The drive circuits used in this thesis are shown in Figures A.1 and A.2.

In Figure A.1, a function generator may be used to start the series resonant converter. IC1a and IC1b are used to produce two opposing signals which turn one MOSFET on and the other off at the series chain. IC2c is an analog switch which enables transfer from function generator operation of the converter to feedback operation. The transistor and IC1c supply the control for this transfering. IC2a, IC2b, IC3a and IC3b are opto isolators which isolate the switching signals and lockout signals. IC4a and IC4b are NAND gates. IC 5a and IC5b are MOSFET drivers DC0026. The lockout strategy is described as follows:

If Q1 is to be turned on, the input signal of IC5a must be "0" (Low). After inversion by IC5a DS0026, two output signals of IC5a become "1" (High). One output is to trigger Q1. The other output signal is used as a feedback signal to IC3a input. Because the feedback signal is high, the opto isolator sends a "0" (Low) output. This Low signal can

Reproduced with permission of the copyright owner. Further reproduction prohibited without permission.

lockout the output of IC4b always as "1" (High) no matter what the other input is. After inversion by IC5b, the switching signal of Q2 is always Low. Therefore, the lockout circuit guarantees two MOSFETs are never turned on at the same time. This gate driving circuit is used in variable frequency SRC in Chapter 2.

Figure A.2 is used for fixed frequency series resonant converter in Chapter 3. In principle, this drive circuit operates the same way as the circuit in Figure A.1 except the lockout circuit is implemented through the enable signal of the HCPL261A opto isolators. As mentioned earlier, this drive circuit is a faster version of Figure A.1 and evolved from the design of Figure A.1. IC1 is a logic gate to invert input signals. IC2, IC3, IC8 and IC9 are opto isolators to filter and lockout firing signals. IC4 and IC5 are DS0026 MOSFET drivers. In this gate drive circuit, a MOSFET firing signal is compared with IRF540 threshold value by the LM361 comparator IC6/IC7 to provide the lockout signal to lockout the other MOSFET firing signal. Therefore, if one MOSFET is turned on, the other MOSFET will be turned off.

A.2 Snubber Circuit

In general, snubbers are composed of diodes, resistors, capacitors. They have following functions:

1). Absorbing stored energy in stray inductances during turn-off. Therefore, the spikes across MOSFETs are reduced.
2). Increasing the rate of change of di/dt during turn-on of MOSFETs.
3). Reducing the rate of growth of dv/dt on MOSFETs during turn-off.
4). Transfering part of switching losses from MOSFETs to resistors in snubbers.

Before implementing the circuits of this thesis, a test circuit was used to check turn-on time, turn-off time and spikes across drain and source of IRF540. In the test circuit, the snubber is a simple R-C circuit. After comparing the effects of various snubber designs with that of the test circuit for the same range of V_S and load to be used in the actual resonant converters, it was found that the snubbers had negligible effects on the MOSFET switching waveforms. Therefore, in the implementations of resonant converters in this thesis, snubbers are not used.

However, a proper heat sink must be used to remove the heat produced due to switching losses. It was assumed that the converters would supply a max of 5A to the load. Therefore, conservatively the steady state power loss on switch was estimated as $5^2 \times 0.077\Omega$ (max on resistance R_{DS} of IRF540) which is about 2W. Since no one MOSFET supplies all of the current all the time, no corrections were applied to correct for additional switching losses. Maximum ambient temperature for this laboratory experimentation without enclosing circuits was assumed to be 50°C (conservatively) and a heat sink calculated on that basis. The heat sink design was adequate for the experimental aspects of this thesis.

Reproduced with permission of the copyright owner. Further reproduction prohibited without permission.

A.3 Control Logic

A.3.1 Below Frequency Operation for VF-SRC

The control block diagram of below frequency operation is shown in Figure A.3.

In the implementation of below frequency operation, the capacitor voltage is processed through peak detector (PKD01) separately to obtain $|V_{C0}|$. In order to implement the control law, two multipliers (AD633JN) are used: one is used to multiply V_S by $\pm v_C - V_0$ to obtain the left hand side of Equation (2.34), the other is used to multiply R$-V_{L0}$ by R$+V_{L0}$ to obtain the right hand side of Equation (2.34). Note that $4V_S(\pm v_C - V_0)$ may be implemented by a programmable gain amplifier if V_S variations are slow. The waveforms of $4V_S(\pm v_C - V_0)$ and $R^2 - V_{L0}{}^2$ are shown in Figure 2.21. $\bar{q}_1$ and $\bar{q}_2$ are the signals out of the comparators shown in Figure 2.21. If $4V_S(\pm v_C - V_0) \leq (R - V_{L0})(R + V_{L0})$, the signals are "0" (Low). Otherwise they are "1" (High). They will be processed by other logic as stated below. The spikes in compared results are not important as they will be eliminated by the additional logic. According to the control law, if $4V_S(\pm v_C - V_0)$ is lower than $R^2 - V_{L0}{}^2$, MOSFETs are to be switched on. The compared results $\bar{q}_1$ and $\bar{q}_2$ are also shown in Figure 2.21. I_L and $\bar{I}_L$ are signals when inductor current is positive and negative respectively. Note that only the sign of I_L is needed. By doing AND and NOT logics for q_2 and I_L, $\overline{q_2 I_L}$ produces switching signal for Q_1. By doing AND and NOT logics for q_1 and $\bar{I}_L$, $\overline{q_1 \bar{I}_L}$ produces switching signal for Q_2, as shown in Figure 2.22. These two switching signals are sent to MOSFET firing and lockout circuit, Figure A.1.

A.3.2 Above Frequency Operation for VF-SRC

The control block diagram of above frequency operation is shown in Figure A.4.

The same peak detectors and multipliers are used to get the left and right hand sides of this simplified control law. The waveforms of $4V_S(\pm v_C + V_0)$, $R^2 - V_{L0}{}^2$ and compared results are shown in Figure 2.23. According to the control law, if $4V_S(\pm v_C + V_0)$ is greater than $R^2 - V_{L0}{}^2$, the MOSFETs are to be switched off. Unlike the below resonant frequency operation, the switching logic is pretty straight forward in above resonant frequency operation. Current direction signals I_L and $\bar{I}_L$ are not used to produce the switching signals here. The negative edges of signals q_1 and q_2 (inverted signals of $\bar{q}_1$ and $\bar{q}_2$) can provide the switching off instants. They are directly used as PRESET and CLEAR signals for a flip-flop (74LS74) to generate switching signals for Q1 and Q2 as shown in Figure 2.24. In the lab, Q1 is the positive output signal of the flip-flop. Q2 is the negative output. Therefore, Q2=$\overline{Q1}$. However, it does not mean that Q1 and Q2 conduct 50% duty. In fact, Q1 does not conduct immediately after the switching signals become "1" until i_L is reversed, because D1 is conducting at that time (V_{DS} is negative). Q2 has the similar conditions. 74LS74 is the main component in switching logic circuit in Figure A.4. Signals for Q1 and Q2 are sent to MOSFET firing and lockout circuits, Figure A.2.

Reproduced with permission of the copyright owner. Further reproduction prohibited without permission.

A.3.3 Nonlinear Operation for CF-SRC

The control block diagram for nonlinear operation mode is shown in Figure A.5. The overall logic is identifical to the logic of variable frequency SRC operation.

A.4 Maple Code

In this Section, the original Maple code used to simplify Equations (3.14) through (3.16) is provided. The results of this simplification are Equations (3.18) through (3.20).

```
# Maple code for simplifying Equation (3.14) to Equation (3.16)
# |((r_2 exp(j pi omega_0/omega)-r_1 exp(j pi))exp(-j theta_1) -1| = 1
# In code below mu = pi omega_0/omega
# a= cos (mu) b= sin (mu);
# In code below theta_1 is written as theta and r_2 as r2 etc.
# Equation (3.14) is
# |(r_2 a + j r_2 b +r_1)exp(-j theta_1) - 1 | = 1
# CODE BELOW lhs is left hand side of above and rhs is 1.

lhs := (r2*a + r1 +I*r2*b)*(cos(theta) -I*sin(theta)) - 1;
magnitude_squared_of_lhs:=simplify(evalc(abs(lhs)*abs(lhs)));
rhs:=1;
#form new_equation which is a rewrite of old equation as |  | -1 = 0
new_equation:= simplify(magnitude_squared_of_lhs-rhs); # = 0
# leave the cos theta terms in new equation on lhs of new equation and
#put all sin theta terms on the right hand side of new equation.
# the only sin theta terms in new equation is -2 r2 b sin(theta)
new_equation_rhs := 2*r2*b*sin(theta);
new_equation_lhs := simplify(new_equation+2*r2*b*sin(theta));
# at this stage use a*a +b*b =1 and simplify lhs of the new equation
new_equation_lhs_no_b := simplify(subs(b=sqrt(1-a*a), new_equation_lhs));
new_equation_lhs_squared := new_equation_lhs * new_equation_lhs;
new_equation_rhs_squared := new_equation_rhs *new_equation_rhs;
# get rid of sin theta terms now Maple will substitute for sin(theta)^2
modified_new_equation := simplify(new_equation_lhs_squared -
new_equation_rhs_squared);
# again use b^2+a^2=1 to get rid of b;
modified_new_equation := simplify(subs(b=sqrt(1-a^2),
modified_new_equation));
# now substitute for cos (theta) = (r1^2+1-R^2)/2*r1
modified_new_equation := simplify(subs(cos(theta) = (r1^2+1-R^2)/(2*r1),
modified_new_equation));
# the equation has r1^2 in denominator. Since right hand side is zero
```


Reproduced with permission of the copyright owner. Further reproduction prohibited without permission.

```
# normalize by multiplying by r1^2
modified_new_equation := simplify(r1^2*modified_new_equation);
# This looks ugly in maple but one can see that there are no coefficients
# beyond R^4 in it and that only R^2 and R^0 are present.
# So collect coefficients a4,a2 and a0
a4 := coeff(modified_new_equation,R,4);
a2 := coeff(modified_new_equation,R,2);
a0 := coeff(modified_new_equation,R,0);
# Maple provides a2, a0  coefficients in an expanded form. To see that
#they are the same as in Dr. Natarajan's derivations, expand and
#compare his coefficients.
simplify(a2 - 2*(r1*r2*a-1)*a4);
simplify(a0 - (r1^2+r2^2)*(1+r1^2*r2^2) +
2*r1*r2*a*(r1^2+r2^2-1-r1^2*r2^2) + 4*r1^2*r2^2);
# Last two come out as zero and Equation (3.16) is verified
# Now substitute for r1,r2 in a4,a2,a0
# alpha is vc0
r1:=1+alpha-v0;
r2:=1+alpha+v0;
a4:=simplify(a4);
a2:=simplify(a2);
a0:=simplify(a0);
# now collect terms in powers of v0
a4:=collect(a4,[alpha,v0]);
a2:=collect(a2,[alpha,v0]);
a0:=collect(a0,[alpha,v0]);
#
```


Reproduced with permission of the copyright owner. Further reproduction prohibited without permission.

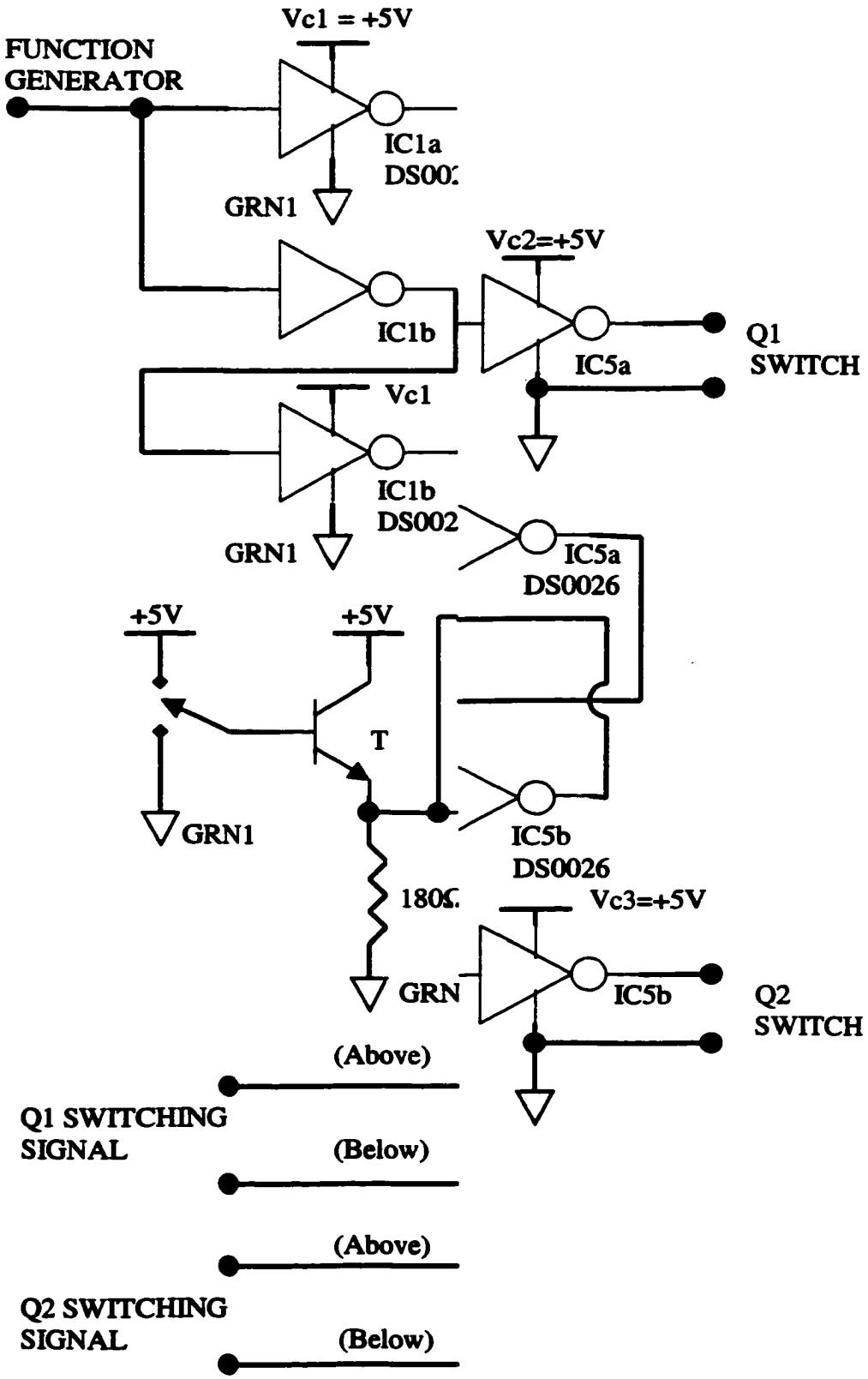

Reproduced with permission of the copyright owner. Further reproduction prohibited without permission.

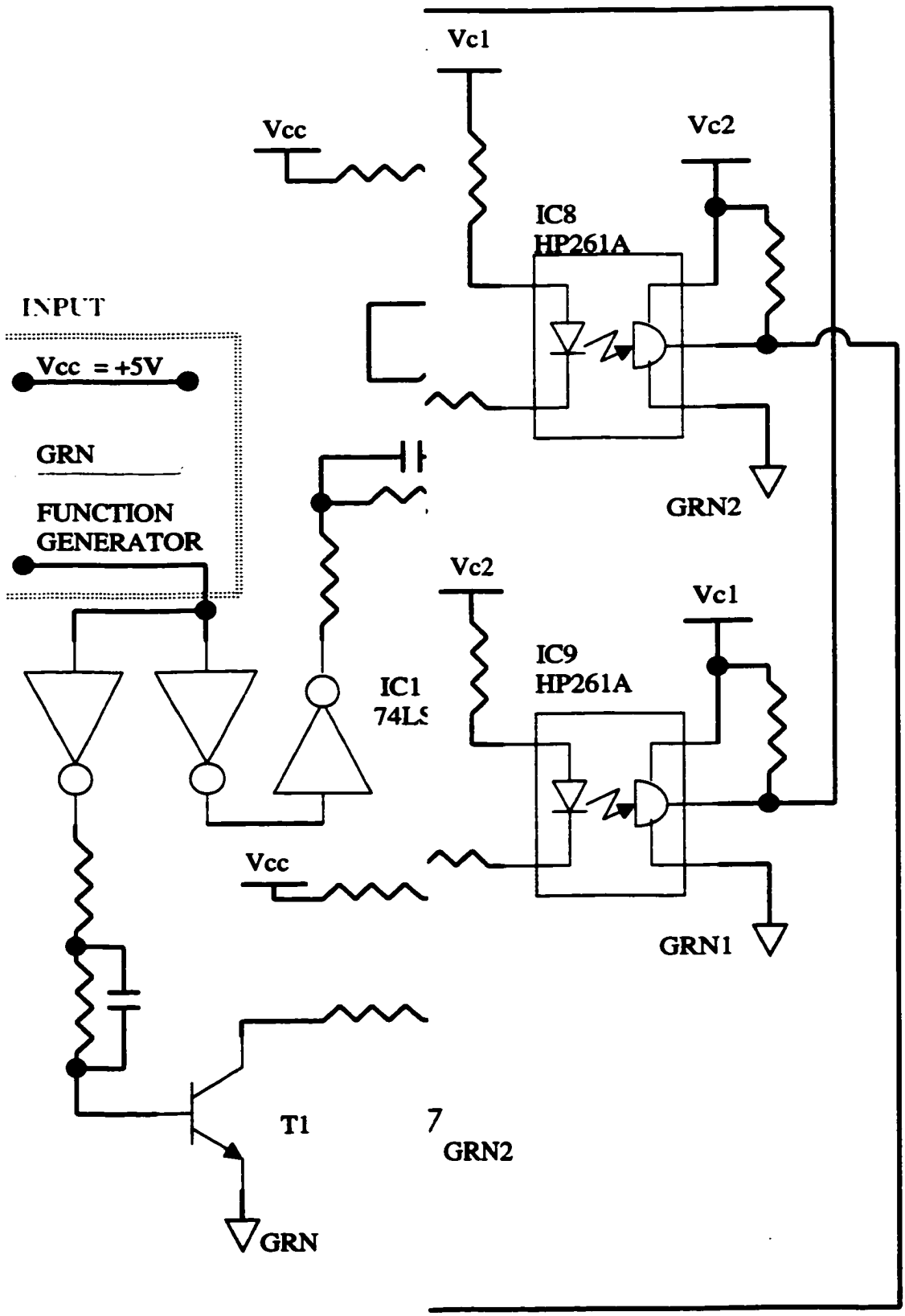

Reproduced with permission of the copyright owner. Further reproduction prohibited without permission.

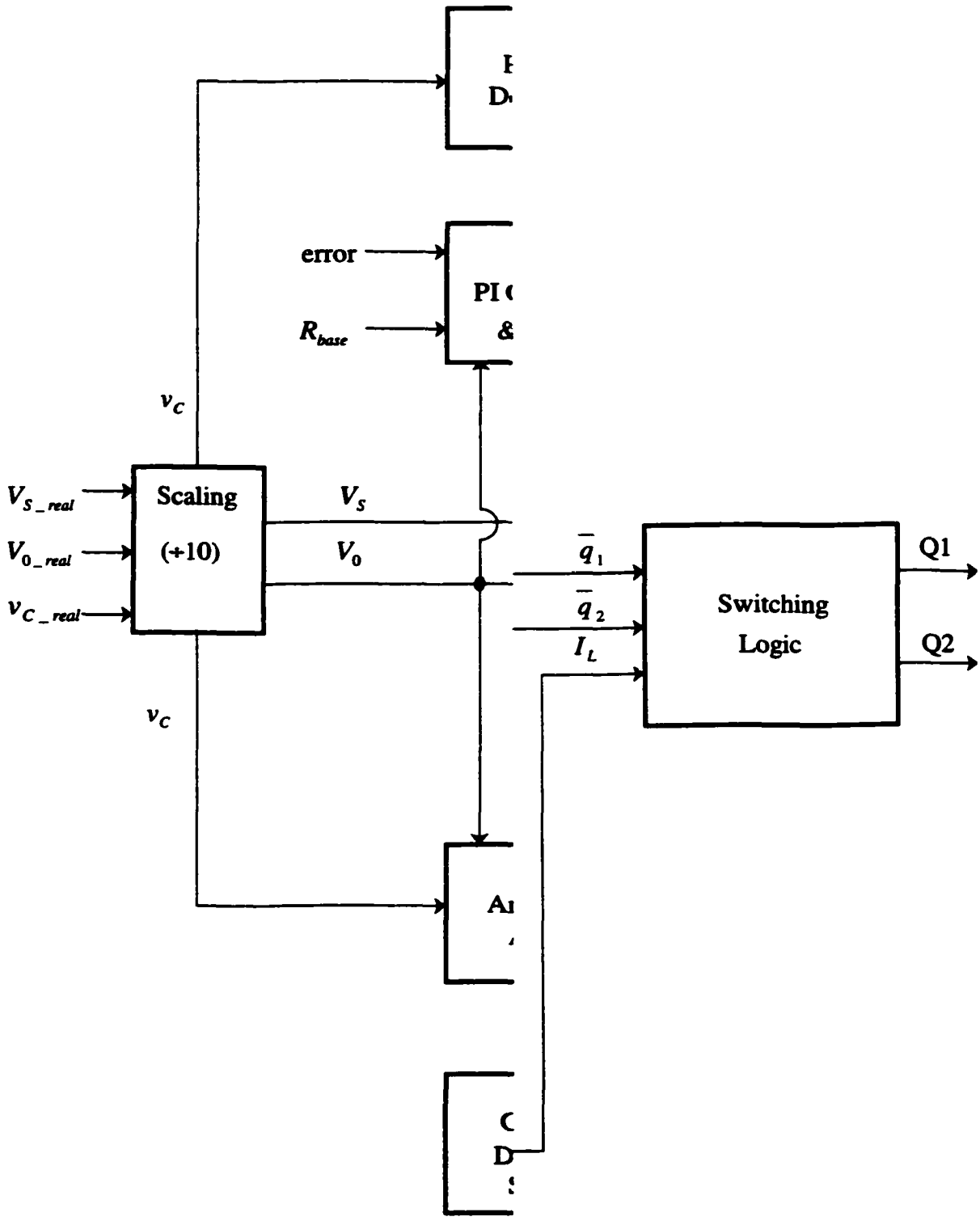

Reproduced with permission of the copyright owner. Further reproduction prohibited without permission.

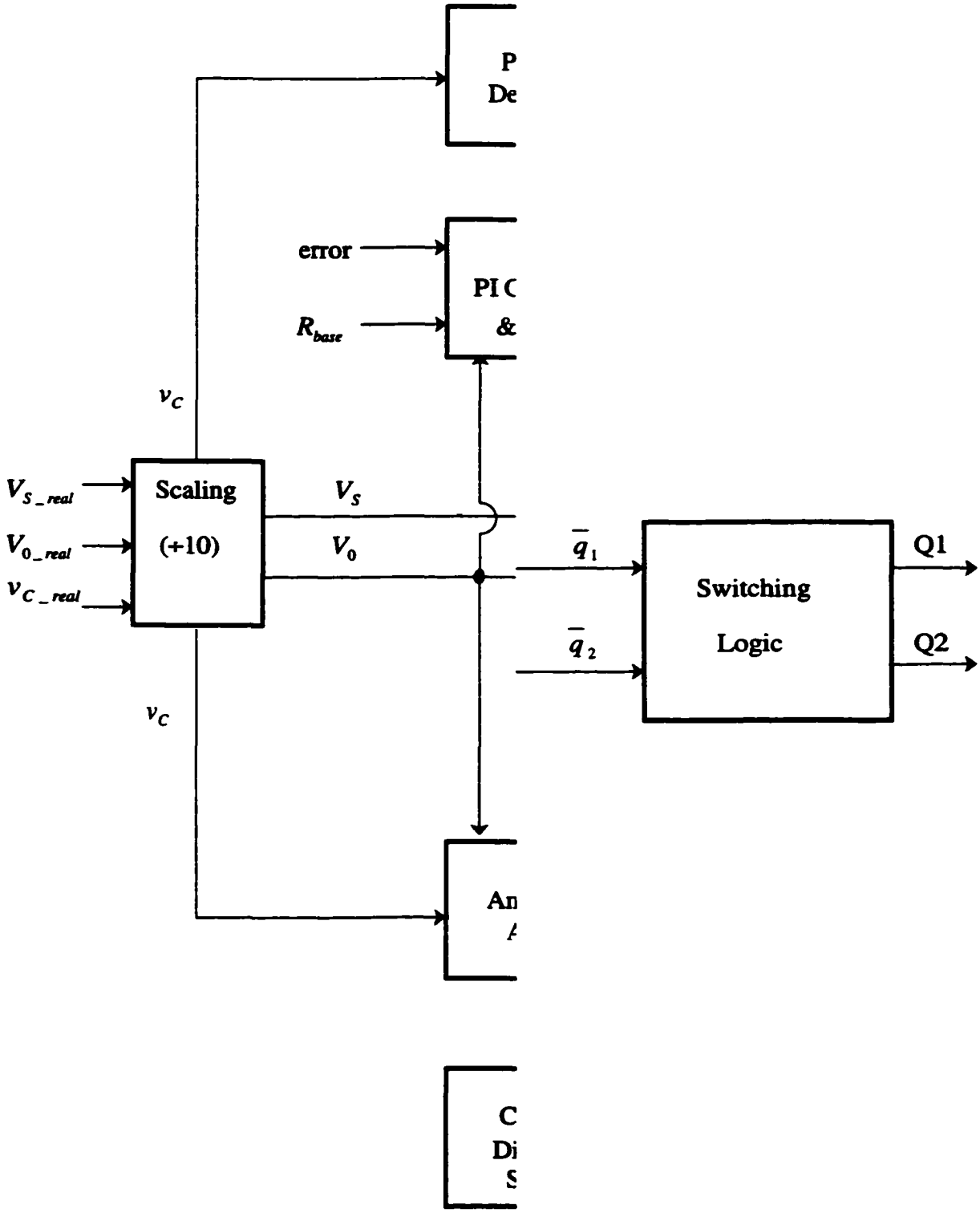

Reproduced with permission of the copyright owner. Further reproduction prohibited without permission.

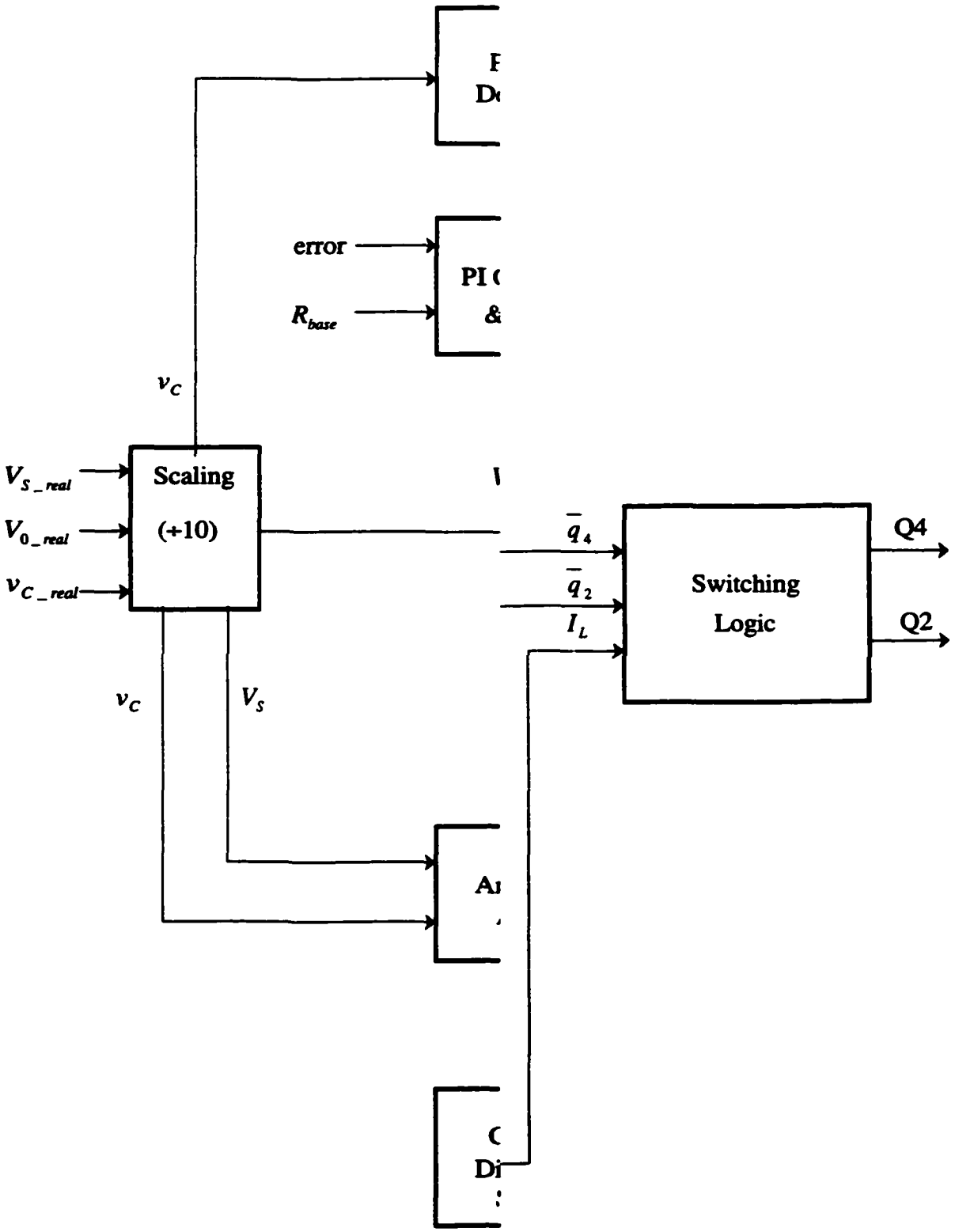

Reproduced with permission of the copyright owner. Further reproduction prohibited without permission.

Bibliography

[1] N. Mohan. T. M. Undeland, W. P. Robbins. *"Power Electronics: Converters, Applications and Design"*, John Wiley and Sons. Inc. 1989.

[2] Peter Wood. *"Switching Power Converter"*. Van Nostrand Reinhold Company. 1981.

[3] Simon S. Ang. *"Power-switching Converter"*. Marcel Dekker. Inc. 1995.

[4] H. W. Whittington, B. W. Flynnand and D. E. Macpherson, *"Switched Mode Power Supplies: Design and Construction"*, John Wiley & Sons, Inc. 1997.

[5] S. Sivakumar, K. Natarajan and A. M. Sharaf, *"Optimal Trajectory Control Series Resonant Converter Using Modified Capacitor Voltage Control Technique"*, pp. 752-759, PESC 1991.

[6] K. Natarajan, S. Sivakumar *"Optimal Trajectory Control of Constant Frequency Series Resonant Converter"*, pp. 215-221, PESC 1993.

[7] R. Oruganti and F. C. Lee, *"Resonant Power Processors, Part I — State Plane Analysis"*, IEEE Transactions On Industry Application, Vol. IA-21, NO.6. pp. 1453-1460, November/December 1985.

[8] R. Oruganti and F. C. Lee, *"Resonant Power Processors, Part II — Methods of Control"*, IEEE Transactions On Industry Applications, Vol. IA-21, NO.6, pp. 1461-1471. November/December 1985.

[9] R. Oruganti. J. J. Yang and F. C. Lee, *"Implementation of Optimal Trajectory Control of a Series Resonant Converter"*, IEEE Transactions On Power Electronics, Vol. 3, No. 3. pp. 318-327, July 1988.

[10] F.S. Tsai, F.C. Lee, *"State Plane Analysis of a Constant Frequency Clamped Mode Parallel Resonant Converter"*, IEEE Transactions On Power Electronics, Vol. 3, No. 3, pp.364-378, July 1988.

[11] N. H. Kutkut, C. Q. Lee and I. Batarseh, *"A Generalized Program for Extracting the Control Characteristics of Rosonant Converters Via the State-Plane Diagram"*, IEEE Transactions On Power Electronics, Vol. 13, No. 1, pp. 58-66, January 1998. Vol. IA-18, No.3, pp.

[12] L. Rossetto, *"A Simple Control Technique for Series Resonant Converters"*, IEEE Transactions On Power Electronics, Vol. 11, No. 4, pp. 554-560, July 1996.

Reproduced with permission of the copyright owner. Further reproduction prohibited without permission.

[13] A.K.S.Bhat, *"A Fixed-Frequency Modified Series-Resonant Converter: Analysis. Design and Experimental Results"*, IEEE Transactions On Power Electronics, Vol. 10, No. 6. pp. 766-776, November 1995.

[14] S.C.Wong and A.D.Brown, *"Analysis, Modeling and Simulation of Series-Parallel Resonant Converter Circuits"*, IEEE Transactions On Power Electroncs, Vol. 10. No. 5, pp. 605-614, September 1995.

[15] M. K. Kazimierczuk and M. K. Jutty, *"Fixed-Frequency Phase-Controlled Full-Bridge Resonant Converter With a Series Load"*, IEEE Transactions On Power Electronics, Vol. 10, No.1, pp. 9-18, January 1995. IEEE Transactions On

[16] R.L. Steigerwald, *"A Comparison of Half-bridge Resonant Converter Topologies"*, IEEE Transactions On Power Electronics, Vol. 3, No. 2, pp. 174-182, April 1988. Transactions On Power Electronics, Vol. 3, No. 1,

[17] Rui Liu and C. Q. Lee, *"Series Resonant Converter with Third-order Commutation Network"*, IEEE Transactions On Power Electronics, Vol. 7, No. 3, pp. 462-468. July 1992.

[18] B.W. Char, K.O. Geddes, G.H. Gonnet, B.L.Leong, M.B. Monagan, & S.M. Watt, *"First Leaves: A Tutorial Introduction to Maple V"*, Springer Verlag. 1992 ISBN 0-387-97621-3.

Reproduced with permission of the copyright owner. Further reproduction prohibited without permission.

Shengli Feng, received the B.S. degree in electrical engineering from Harbin Electrical and Technical Institute, People's Republic of China, in 1992. From 1992 to 1996, he was employed as an electrical engineer in Xi'an Power and Electronic Research Institute, People's Republic of China. He began to pursue his M.Sc.Eng. degree from Lakehead University, Thunder Bay, Ontario, in 1997. Currently he works as a commissioning engineer officer in Ontario Power Generation Inc., Pickering NGS, Ontario.

Reproduced with permission of the copyright owner. Further reproduction prohibited without permission.